

WASHINGTON UNIVERSITY

Department of Physics

Dissertation Committee:

James S. Schilling, Chairperson

Anders E. Carlsson

Mark S. Conradi

Sophia E. Hayes

Anne M. Hofmeister

Kenneth F. Kelton

SUPERCONDUCTIVITY STUDIES  
AT EXTREME PRESSURE

By

James J. H. Hamlin

A DISSERTATION PRESENTED TO THE  
GRADUATE SCHOOL OF ARTS AND SCIENCES  
OF WASHINGTON UNIVERSITY IN  
PARTIAL FULFILLMENT OF THE  
REQUIREMENTS FOR THE DEGREE  
OF DOCTOR OF PHILOSOPHY

December 2007

St. Louis, Missouri

© Copyright 2007

by

James Jeffrey Hengst Hamlin

# Preface

Superconductivity is a phenomena that would likely never have been predicted by theory in the absence of the experimental discovery [1,2] because it depends on the seemingly unlikely scenario of two electrons being attracted to each other. For nearly a century, this exotic low-temperature phase has attracted considerable interest in large part due to the, as yet unrealized, promise of room-temperature superconductivity and its many potential applications. While we now have a basic theoretical understanding of superconductivity [3], from a practical standpoint, theory has yet to prove successful in bringing superconductivity closer to room-temperature. Systematic experimental studies, both through chemical substitution and high pressure, are still the primary means of discovering higher temperature superconductors. In this dissertation I will describe the results of ultra-high pressure experiments (up to 1.7 Mbar) on pure elements, alloys and compounds. A variety of probes including resistivity, ac magnetic susceptibility and optical spectroscopy are used to investigate the optimal conditions for high superconducting transition temperatures.

# Acknowledgements

I offer my most sincere thanks to:

My advisor, Dr. Jim Schilling, whom it has been a privilege to work for. I can not thank you enough for the experience I have gained as your student.

Dr. Anne Hofmeister, for generously donating her time, equipment and expertise to make the infrared absorption measurements possible.

Dr. Vladimir Tissen for many informative discussions and for first suggesting that we examine yttrium.

The members of my dissertation committee, for helpful discussions and enlightening answers.

Julia Hamilton, for reminding me, with good humored insistence, to take the necessary steps to actually graduate.

Dr. A. Gangopadhyay for assistance with the PPMS measurements.

Dr. J. D. Pasteris and Dr. B. Wopenka for help with Raman measurements.

Todd Hardt, Denny Huelsman, and especially Tony Biondo for being excellent machine shop teachers.

T. Matsuoka, for a very exciting three months worth of experiments, and many fine cups of coffee.

Members of the Schilling group past and present whom I've had the opportunity to work with, F. Mascarenhas, E. Kline, B. Beckett, W. Bi, N. Hillier, C. Looney, T. Tomita, M. Debessai for contributing so much to the work described in this dissertation and S. Deemyad for teaching me the DAC.

All the members of the Washington University Physics Department, who have created such a friendly atmosphere.

My parents, Marilyn and Jeffrey, who's continual support and encouragement has made my graduate studies possible.

Most of all, I thank my wife Chi-Shan, to whom this dissertation is dedicated, and who has consistently inspired me not give up at the sight of a freshly powdered diamond.

# Contents

<b>Preface</b>	<b>i</b>
<b>Acknowledgements</b>	<b>ii</b>
<b>Contents</b>	<b>iv</b>
<b>List of Tables</b>	<b>vi</b>
<b>List of Figures</b>	<b>vii</b>
<b>1 Introduction</b>	<b>1</b>
<b>2 Background: Theory and Experiment</b>	<b>4</b>
2.1 Superconductivity . . . . .	4
2.1.1 BCS Theory of Superconductivity . . . . .	5
2.1.2 Penetration Depth and Coherence Length . . . . .	8
2.2 High Pressure . . . . .	9
2.2.1 Equation of State . . . . .	12
2.2.2 Effect of Pressure on Superconductors . . . . .	12
2.3 Superconductivity of the Elements . . . . .	15
2.4 A Useful Ratio: Volume per Atom versus Ionic Volume . . . . .	18
2.4.1 Magnetism . . . . .	19
2.4.2 The Goldhammer-Herzfeld Criterion for Metallization . . . . .	21
2.4.3 Structure Sequence of Rare-Earth Elements . . . . .	24

<b>3</b>	<b>Experimental Apparatus and Methods</b>	<b>28</b>
3.1	Diamond Anvil Cell . . . . .	28
3.2	Cryostat . . . . .	34
3.3	Vickers Hardness . . . . .	40
3.4	Water Cooled Magnet . . . . .	43
3.5	Optical Measurements in the Diamond Anvil Cell . . . . .	46
3.5.1	Ruby Fluorescence Manometer . . . . .	46
3.5.2	Diamond Vibron Manometer . . . . .	53
3.5.3	Optical Absorption Measurements . . . . .	58
3.5.4	Measuring Gasket Thickness . . . . .	60
3.6	Coil System and AC Magnetic Susceptibility . . . . .	64
3.7	Resistivity Measurements in the Diamond Anvil Cell . . . . .	69
3.8	General Considerations for Reaching Higher Pressures . . . . .	71
<b>4</b>	<b>Results and Discussion</b>	<b>73</b>
4.1	Superconductivity in d-Electron Metals . . . . .	73
4.1.1	Experiment . . . . .	74
4.1.2	Analysis . . . . .	91
4.2	Low-Z Materials . . . . .	100
4.2.1	Li and Li(Mg) Alloy . . . . .	101
4.2.2	CaLi <sub>2</sub> Compound . . . . .	105
4.2.3	Complex Hydrides: LiBH <sub>4</sub> and LiAlH <sub>4</sub> . . . . .	111
<b>5</b>	<b>Summary</b>	<b>118</b>
	<b>Bibliography</b>	<b>119</b>
<b>A</b>	<b>R/V for Selected Compounds</b>	<b>120</b>
<b>B</b>	<b>Overview of the Optical System</b>	<b>123</b>
<b>C</b>	<b>Optical Measurement using the Nikon Optiphot Microscope</b>	<b>127</b>
<b>D</b>	<b>A Precise Method for Aligning Optics at Infinite Conjugate</b>	<b>130</b>

# List of Tables

2.1	Crystal structures found in the rare-earths at ambient and high pressure. Elements in parentheses show anomalies. . . . .	25
3.1	Vickers hardness of various materials. . . . .	43
4.1	Parameters obtained by fitting $T_c$ versus relative volume data with the McMillan Equation. . . . .	93
4.2	Ambient pressure values of $R_{WS}$ , $R_c$ and $R_{WS}/R_c$ . . . . .	98
B.1	Components of the optical system. . . . .	126

# List of Figures

1.1	Highest superconducting critical temperatures attained from discovery of superconductivity to present. . . . .	3
2.1	Schematic illustration of the electron-phonon coupling mechanism. . .	7
2.2	Estimated number of papers concerning diamond anvil cells for each year. . . . .	11
2.3	Dependence of relative volume ( $V/V_0$ ) on pressure for several elemental solids. . . . .	13
2.4	Periodic table showing the occurrence of superconductivity in the elements. . . . .	16
2.5	Schematic of solid at low pressure and high pressure. . . . .	19
2.6	The ratio $\alpha = R_{WS}/R_{mo}$ for the elemental solids. . . . .	20
2.7	$R/V$ versus column in the periodic table for the elemental solids. . .	23
2.8	Values of the $R_{WS}/R_{5p}$ for structural transitions for the rare earths. .	27
3.1	Cross-sectional view of the diamond anvil cell designed by J. S. Schilling.	29
3.2	The mechanically loaded DAC designed by R. Boehler. . . . .	30
3.3	Sample pressure versus membrane pressure. . . . .	32
3.4	Magnetization data for various gasket materials. . . . .	33
3.5	The Oxford Instruments continuous flow cryostat. . . . .	35
3.6	Warming rate versus temperature for the Oxford cryostat. . . . .	38
3.7	Cooling rate versus temperature for the Oxford cryostat. . . . .	39
3.8	Empirical relationship between Vickers and Rockwell C hardness. . .	40
3.9	The Vickers hardness test. . . . .	41
3.10	Schematic of a system for measuring Vickers hardness. . . . .	42

3.11	Cross sectional plan of water cooled magnet spool. . . . .	44
3.12	Temperature versus power for the water cooled magnet. . . . .	45
3.13	Energy levels associated with ruby fluorescence. . . . .	47
3.14	Temperature dependence of the $R_1$ ruby fluorescence line at ambient pressure. . . . .	49
3.15	Comparison of different ruby manometer calibrations. . . . .	51
3.16	Ruby measurements taken at various pressures. . . . .	52
3.17	FWHM versus pressure of the ruby $R_1$ line. . . . .	52
3.18	Pressure dependence of the diamond vibron. . . . .	55
3.19	Raman spectra of diamond anvils under pressure. . . . .	57
3.20	Schematic of a Fourier Transform Infrared Spectrometer (FTIR). . . . .	59
3.21	Example of extracting the fraction of light transmitted by a sample as a function of wavelength. . . . .	59
3.22	First and second order reflections giving rise to a Fabry-Pérot interference spectrum. . . . .	61
3.23	Spectral measurements used to determine the separation between the diamond culets. . . . .	63
3.24	Thickness versus pressure as determined by Fabry-Pérot interference. . . . .	64
3.25	Overview of the ac magnetic susceptibility technique and coil system. . . . .	65
3.26	Schematic of the ac magnetic susceptibility circuit. . . . .	66
3.27	Model of the coil system. . . . .	67
3.28	Estimated ac magnetic susceptibility signal for a sample broken into several pieces. . . . .	69
3.29	Arrangement of leads used for measuring resistivity in a DAC. . . . .	70
3.30	Circuit for measuring ac resistance using a lock-in amplifier. . . . .	71
4.1	AC magnetic susceptibility for yttrium at a variety of different pressures. . . . .	76
4.2	Superconducting transition in the ac susceptibility of yttrium metal versus pressure. . . . .	78
4.3	AC magnetic susceptibility in nanovolts versus temperature for Sc at different pressures. . . . .	80
4.4	Superconducting transition temperature $T_c$ versus pressure for Sc. . . . .	82

4.5	Image of the Lu sample at 174 GPa. . . . .	84
4.6	Ac susceptibility versus temperature for Lu at several pressures. . . . .	85
4.7	Dependence of superconducting transition on dc magnetic field for Lu. . . . .	86
4.8	$T_c$ versus pressure for pure Lu metal. . . . .	86
4.9	Resistance versus Temperature for Eu at 80 GPa. . . . .	89
4.10	Field dependence of the possible superconducting transition in Eu. . . . .	90
4.11	$T_c$ versus relative volume for Sc, Y and Lu. . . . .	94
4.12	Calculated d-band occupancy $N_d$ versus $R_{WS}/R_c$ . . . . .	97
4.13	$T_c$ versus $R_{WS}/R_c$ for the non-magnetic, trivalent, rare-earth metals Sc, Y, La and Lu. . . . .	99
4.14	$T_c$ versus pressure for pure Li and $\text{Li}_{0.9}\text{Mg}_{0.1}$ . . . . .	102
4.15	Magnetic field dependence of $T_c$ in pure Li under pressure. . . . .	103
4.16	Ac susceptibility versus temperature for $\text{Li}_{0.9}\text{Mg}_{0.1}$ at several pressures. . . . .	105
4.17	Resistance versus pressure for $\text{CaLi}_2$ . . . . .	107
4.18	Resistance versus pressure normalized to the resistance at 16 K for $\text{CaLi}_2$ . . . . .	108
4.19	$T_c$ versus pressure for $\text{CaLi}_2$ . . . . .	110
4.20	Transmitted light photographs for two of the high pressure experiments on complex hydrides. . . . .	114
4.21	Transmission versus photon energy for $\text{LiAlH}_4$ . . . . .	117
B.1	Schematic of the optical system. . . . .	125
C.1	Schematic of Nikon Optiphot microscope configured for optical mea- surements in a DAC. . . . .	129
D.1	Proper configuration for achromatic lenses. . . . .	131
D.2	A common optical system consisting of two achromatic lenses. . . . .	132
D.3	Method for aligning lenses at infinite conjugate. . . . .	132
D.4	Appearance of crosshair when system is aligned for infinite conjugate. . . . .	132

# Chapter 1

## Introduction

In 1908, Heike Kamerlingh-Onnes succeeded in liquefying  $^4\text{He}$ , the last of the so-called “permanant gases”. This extended the lowest temperature achievable in a laboratory from 12 K (by pumping the vapor above solid hydrogen) [4] to slightly below 1 K. Most experimenters in the field simply condensed small amounts of cryogenic fluids in order to demonstrate that liquification was possible. Onnes focused on using liquid helium as a tool to investigate the vast world of unexplored physics at very low temperatures. Thus, by 1911, Onnes had refined his liquification techniques to yield useful (though still minute by today’s standards) quantities of liquid helium and had built the world’s first helium cryostat, allowing his group to begin to study the properties of matter at the lowest possible temperatures. Among the first properties studied was the resistivity of pure metals. This subject was of interest for fundamental reasons and for the practical use of metallic resistivity as a secondary thermometer. It was known that the resistivity dropped with temperature but there was a great deal of speculation as to how the resistivity of a pure metal would change as the temperature approached absolute zero. Some thought the resistance would smoothly approach zero at zero temperature while others surmised it would smoothly approach a constant value. Still others, including Lord Kelvin, proposed that the resistivity would become infinite at zero temperature as the electrons became “frozen” in place [4, 5]. A few, including Onnes himself at times, speculated that the resistivity would smoothly approach zero at finite temperature. It was thus a complete suprise when Onnes and graduate

student Gilles Holst found [1,2] that the resistivity of mercury<sup>1</sup> dropped *abruptly to zero* near 4.2 K. The phenomenon, originally named *superconductivity*, is now referred to as *superconductivity*. Subsequent experiments showed that the resistivity in the superconducting state is indeed zero to arbitrary measurement sensitivity.

In the years following the discovery of superconductivity in mercury, the phenomena was discovered in a number of other materials, first in pure elements and later in alloys and compounds. It was clear from the beginning that practical applications would require the discovery of materials that became superconducting at significantly higher temperatures. Figure 1.1 shows the progression of the highest superconducting critical temperature ( $T_c$ ) achieved over the years. After the initial discovery, progress increasing  $T_c$  was slow for over 70 years. A breakthrough came in 1986 when Bednorz and Müller discovered superconductivity, at 30 K, in a ceramic material containing La, Ba, Cu, and O (LBCO) [6], the first of the so-called *high- $T_c$*  or *cuprate* superconductors. Subsequently, Chu *et al.* studied the superconductivity of LBCO under pressure and found that  $T_c$  increased rapidly with applied pressure [7]. Given that pressure results in a reduction of lattice parameter, it was logical to ask whether it would be possible to reduce the lattice parameter of the LBCO compound through chemical means. Chu *et al.* achieved this reduction of lattice parameter by replacing La with isoelectronic and smaller Y, leading to a compound (YBCO) with  $T_c$  near 90 K [8]. This was the first superconducting material with  $T_c$  above the boiling point of liquid nitrogen. Thus, pressure played a critical role in one of the most highly celebrated breakthroughs in superconductivity research. Today, the record for the highest superconducting critical temperature is  $T_c = 164$  K in a mercury based cuprate under a pressure of 31 GPa [9].

Despite nearly a century of research since G. Holst and Kamerlingh Onnes' discovery of superconductivity and half a century since the development of a complete microscopic theory of superconductivity (BCS theory) [3], there is still no general theory able to reliably predict the superconducting critical temperature of a given material or even if a material will become superconducting. For this reason, systematic studies continue to be the primary method for the discovery of new superconductors. High

---

<sup>1</sup>Mercury was one of the first metals studied because it is rather easy to purify.

pressure experiments are an invaluable aid to such systematic studies because they provide the only available means to significantly reduce the lattice parameter without changing chemical composition. Chemical substitution studies typically change the average interatomic spacing by  $\lesssim 1\%$  while modern high pressure techniques are capable of changes as great as 40%.

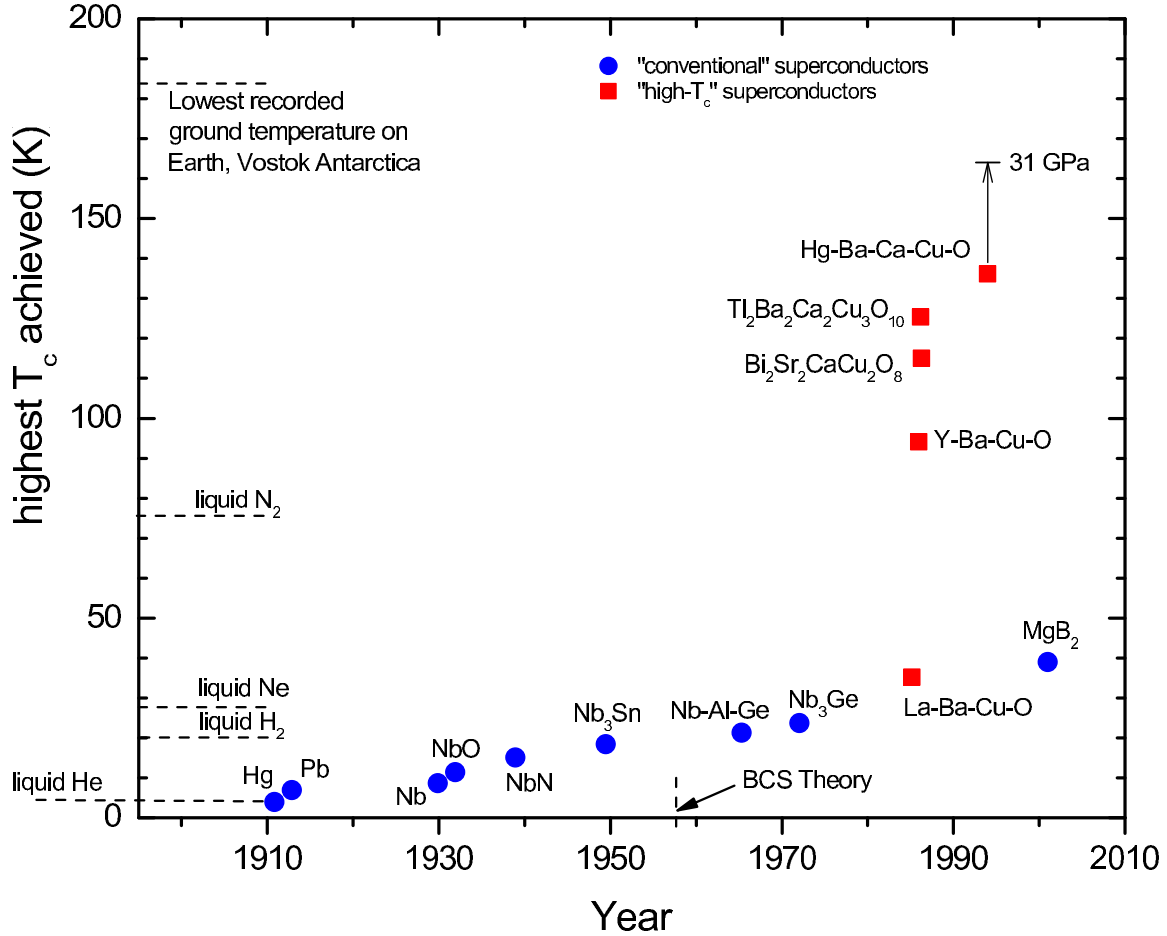


Figure 1.1: Highest superconducting critical temperatures attained from discovery of superconductivity to present. Figure adapted from Reference [10].

## Chapter 2

# Background: Theory and Experiment

### 2.1 Superconductivity

After nearly a century of development, the field of superconductivity is by now highly developed with many excellent texts describing the properties of superconductors in great detail [11–14]. Therefore, this chapter will simply provide a brief introduction to the main concepts and introduce ideas that will be useful in the later chapters.

The primary phenomena associated with superconductivity are: i) zero dc electrical resistivity when the current is below a certain critical value and ii) expulsion of magnetic field from the interior of the superconductor (Meissner-Ochsenfeld effect) when the applied field is below a critical value. Both phenomena only occur when the temperature is below a critical temperature referred to as  $T_c$ . Thus, when the temperature of a superconductor is cooled below  $T_c$ , the resistivity drops, more or less, abruptly to zero. That the resistivity is actually zero rather than being very small can be demonstrated straightforwardly by measuring the decay of a magnetic field induced by a supercurrent running in a loop. If the resistance were finite then the field would gradually decay over time. In fact, it is found that at low enough temperature, the supercurrents persist for as long as one measures [15]. The Meissner-Ochsenfeld effect was first observed in 1933 [16]. The effect demonstrates that superconductors are not only perfect conductors but also perfect *diamagnets* (with susceptibility,

$\chi = -1$ , in MKS units). This means that the magnetic field within a superconductor is zero regardless of whether the field is applied before or after the superconductor is cooled below  $T_c$ . This is in contrast to the expectation if a superconductor were merely a perfect conductor and is the piece of evidence that proves superconductivity is a phase of matter in the thermodynamic sense.

### 2.1.1 BCS Theory of Superconductivity

After the discovery of superconductivity in 1911 [1, 2], it took nearly half a century for a complete microscopic description of the phenomena to be developed. In 1938, F. London [17] showed that infinite conductivity (and the suppression of thermal conductivity in the superconducting state) could be explained by the Bose-Einstein condensation of Bosonic charge carriers. However, it was not clear at that time how such a situation could arise given that the charge carriers in metals are electrons (fermions). In 1946, R. A. Ogg, Jr. suggested that superconductivity could be explained by the Bose-Einstein condensation of trapped electron pairs [18, 19]. Electron pairs would have integer spin and thus be able to undergo Bose-Einstein condensation. In the same paper, Ogg reported superconductivity at 180 K in quenched metal-ammonia solutions. Unfortunately, no other researchers were able to reproduce this spectacular result. Consequently, this early suggestion by Ogg that superconductivity could be explained by Bose-Einstein condensation of bound electron pairs is largely ignored (for a discussion of this episode see Reference [20]). In 1950, H. Fröhlich showed that a coupling between the lattice (phonons) and electrons would lead to an effective electron-electron interaction. At nearly the same time, the importance of this phenomena for superconductivity was confirmed by the observation of the *isotope effect* concurrently by Reynolds *et al.* [21] and Maxwell *et al.* [22]. They found that different isotopes of mercury displayed different superconducting transition temperatures, with the  $T_c$  of the lighter isotopes being slightly higher than that of the heavier isotopes. This key experimental observation indicated that the electron pairing must be occurring through some interaction with the lattice vibrations (phonons). Using the idea of an *electron-phonon coupling*, the seminal paper of Bardeen, Cooper and Schrieffer [3] finally described a complete microscopic theory of superconductivity (BCS

theory). There are superconductors that do not fit into the framework of the BCS theory, namely the high- $T_c$  cuprate superconductors. However, we restrict our discussion here to electron-phonon coupled, BCS or *conventional* superconductors since the experiments presented in this dissertation all concern apparently conventional superconductors.

Figure 2.1 shows a schematic illustration of the electron-phonon coupling mechanism. As an electron passes through the lattice it attracts the positive cations to it causing a vibration of the lattice (phonon). Thus a localized region of excess positive charge builds up. Because the much more massive cation moves more slowly than the electron, this region of excess positive charge remains for some time after the electron has moved on. Some time later, a second electron can be attracted to this same region of excess positive charge. This leads to an effective attractive interaction between the two electrons causing them to “pair up” into a so-called *Cooper pair*. Note that the spacing between the two electrons in the pair is typically several hundred or a thousand times the interatomic spacing. The interaction is retarded since the attractive interaction occurs via phonons which travel with finite speed (while the Coulomb repulsion between the electrons is nearly instantaneous). The interaction need only be attractive in some (possibly very small) region of space-time, in order for the electrons to pair up. In the limit of weak electron-phonon coupling, the BCS theory predicts the following relationships. The critical temperature for the transition to superconductivity is given by

$$T_c = 1.14 \left( \frac{\hbar\omega_D}{k_B} \right) \exp \left[ \frac{-1}{N(E_F)V_{eff}} \right], \quad (2.1)$$

where  $k_B$  is the Boltzmann constant,  $N(E_F)$  is the density of states at the Fermi level,  $V_{eff}$  is the net attractive potential between electrons, and  $\omega_D$  is the Debye frequency. The density of states at the Fermi level appears because only electrons within  $\sim \hbar\omega_D$  of the Fermi level can form pairs. Electron deep within the Fermi sea cannot pair because there are no nearby unoccupied states for them to scatter into (Pauli blocking). Because it takes a finite energy to break apart a Cooper pair, a energy gap appears in the electronic excitation spectrum. The energy gap as a

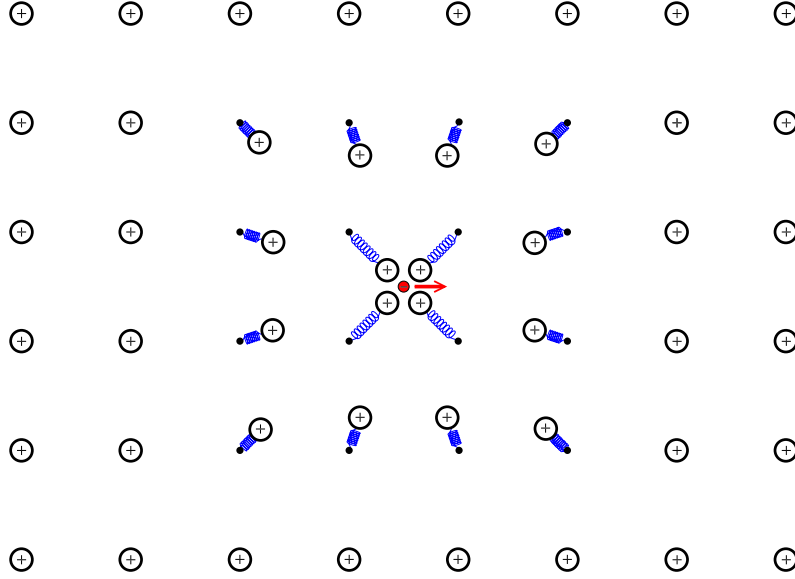


Figure 2.1: Schematic illustration of the electron-phonon coupling mechanism. The small central dot with minus sign shows an electron and the arrow shows the path of the electron. Springs indicate restoring force bringing the cations back to their equilibrium positions.

function of temperature at temperatures close to  $T_c$  is given by

$$\frac{\Delta(T)}{\Delta(0)} = 1.74 \left(1 - \frac{T}{T_c}\right)^{\frac{1}{2}}, \quad T \approx T_c, \quad (2.2)$$

showing that the gap closes when  $T = T_c$ . The gap at  $T = 0$  K and critical temperature are related by [14]

$$\frac{\Delta(0)}{k_B T_c} = 1.76. \quad (2.3)$$

The critical field above which superconductivity is destroyed is given approximately by

$$H_c \simeq H_0 \left[1 - \left(\frac{T}{T_c}\right)^2\right], \quad (2.4)$$

where  $H_c$  is the critical field at temperature  $T$  and  $H_0$  is the critical temperature at  $T = 0$  K. A useful relationship between the temperature dependence of the critical field and the density of states at the Fermi level is given by Equations 2.5 and 2.6 [3]. These two equations allow one to estimate  $N(E_F)$  simply by measuring the field

dependence of the critical temperature at low fields.

$$\frac{1}{\gamma} \left( \frac{dH_c}{dT} \right)^2 \Big|_{T \approx T_c} = 19.4 \quad (2.5)$$

$$\gamma = \frac{2}{3} \pi^2 N(E_F) k_B^2 \quad (2.6)$$

Generalizations of the BCS theory to stronger coupling have been nicely summarized by Diederichs [23].

### 2.1.2 Penetration Depth and Coherence Length

There are two important length scales associated with superconductivity, the London penetration depth,  $\delta$  and the coherence length,  $\xi$ . The penetration depth is associated with the fact that a magnetic field will penetrate the surface of a superconductor, falling off exponentially with increasing depth from the surface [24]. Specifically,  $\delta$  gives the distance at which the magnetic field inside the superconductor falls to  $1/e$  of the applied field. In a real sense,  $\delta$  is the thickness of the layer of shielding current which prevents the applied field from penetrating the superconductor. The temperature dependence of the penetration depth is given by

$$\delta = \frac{\delta_0}{\sqrt{1 - (T/T_c)^4}}, \quad (2.7)$$

Showing that the penetration depth diverges to infinity as the sample is warmed to  $T_c$ . However,  $\delta \sim \delta_0$  except at temperatures close to  $T_c$ .

The coherence length,  $\xi$  has two interpretations. According to the BCS interpretation,  $\xi_{BCS}$  is the size of the Cooper pair. According to the Ginzburg-Landau interpretation,  $\xi_{GL}$  is a measure of the length over which the superconducting order parameter (supercurrent carrier density) cannot vary appreciably. According to the latter interpretation, it becomes clear that a supercurrent can tunnel from one superconductor through a non-superconducting region to another superconductor as long as the distance traveled through the non-superconducting region is less than  $\xi_{GL}$ . Values of  $\delta$  and  $\xi$  for several superconductors are tabulated in Reference [25].

Materials with  $\delta < \xi/\sqrt{2}$  are called type I superconductors while materials with  $\delta > \xi/\sqrt{2}$  are called type II superconductors. Type I superconductors exhibit the Meissner state (complete exclusion of the applied field) at temperatures below  $T_c$  and fields below  $H_c$ . Type II superconductors exhibit an additional state known as the *mixed state*. In the mixed state, it becomes energetically favorable for fluxoids (single quanta of magnetic flux) to penetrate the sample. Thus in the mixed state, the field is not entirely excluded from the superconductor. In a type II superconductor, one finds the Meissner state at fields less than  $H_{c1}$ . As the field is increased above  $H_{c1}$ , more and more fluxoids penetrate the sample until, eventually, bulk superconductivity is destroyed above  $H_{c2}$ . Note that the resistivity is zero ( $\rho = 0$ ) all the way up to  $H_{c2}$ . Type I superconductors generally have  $H_c$  values of much less than a Tesla whereas type II superconductors can have  $H_{c2}$  values of several hundred Tesla [25]. Therefore, in applications requiring high magnetic fields, type II superconductors are employed.

## 2.2 High Pressure

Pressures found in the universe vary over a tremendous range from  $10^{-32}$  bars in the vacuum of intergalactic space, to  $10^{67}$  bars inside of a black hole. In between these extremes, we have all life as we know it from  $\sim 1$  bar at sea level to  $\sim 1$  kbar at the bottom of the ocean. The pressure at the core of the earth is  $\sim 3.5$  Mbar. One might consider the maximum experimentally accessible pressure to be several hundred Mbar, the pressure at the center of a nuclear explosion.

The importance of high pressure studies to our understanding of condensed matter has perhaps been best summarized by Percy Williams Bridgman:

The condensed state, *par excellence*, is obviously presented by matter under high pressure, so that, to say the least, our understanding of the condensed state cannot be regarded as satisfactory until we can give an account of the effect of pressure on every variety of physical phenomena.

- *P. W. Bridgman* (1935) [26]

Many of the earliest efforts in high pressure were directed towards measuring the compressibility of fluids, in particular water which, for a long time, was believed

to be incompressible. The compressibility of water was finally determined in 1762 [27]. The pressure dependence of resistivity, dielectric properties and melting curves were also studied, and continue to be focal points for high pressure research. The continual drive to reach ever higher pressures was likely significantly motivated by the possibility of synthesizing diamond at high pressure. The early history of high pressure research is outlined in Reference [28]. Until about a century ago, there were very few researchers investigating the properties of matter at high pressure. By the opening of the 20th century, experimentally accessible pressures were limited to a maximum of several thousand bars. Beginning his work in 1905 at Harvard University, Percy Williams Bridgman vastly extended the upper limit of experimentally accessible pressure through a series of brilliant technological innovations. In 1946, Bridgman won the Nobel Prize in Physics for his efforts in high pressure. By the end of his career, Bridgman was able to reach pressures above 100 kbar by compressing the sample between metallic anvils. Today, it is possible to reach static pressure in excess of 3 Mbar, nearly the pressure at the core of the earth! The device that makes this possible is the *diamond anvil cell* (DAC), a direct descendent of the Bridgman cell.

The DAC was invented in the late 1950's at the National Bureau of Standards (NBS) by C. E. Weir, A. V. Valkenburg, E. R. Lippencott and E. N. Bunting [29]. The exceptional strength of diamond is what allows the DAC to reach the extreme pressures mentioned above. Since diamond is transparent in a wide range of the electromagnetic spectrum, the DAC is particularly suited for optical studies. The development of the optical ruby fluorescence manometer [30] made it possible to accurately determine pressure inside the DAC and lead to widespread adoption of the DAC as an experimental tool. The DAC provides the highest possible *static* pressures and has, therefore, gained increasing popularity over the years. Figure 2.2 shows the estimated number of papers concerning the phrase “diamond anvil cell” versus year. While dynamic shock techniques can produce pressures higher than the DAC, these pressures exist for fractions of a second and are accompanied by high temperatures. The DAC allows high pressure at the low temperatures required for the study of superconductivity. The combination of extremely high pressure and extremely low temperature is particularly exotic in that it must be quite rare in nature.

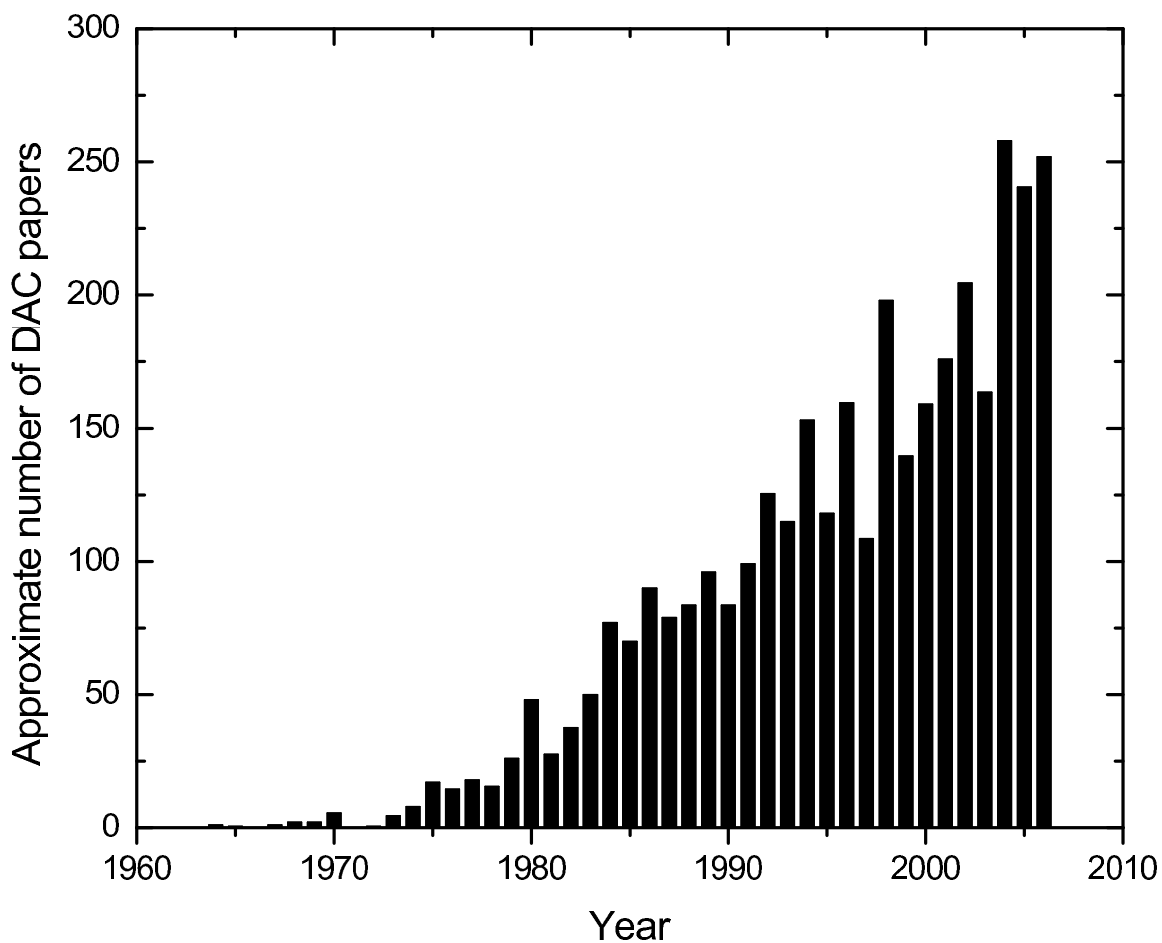


Figure 2.2: Estimated number of papers concerning diamond anvil cells for each year. The number of papers are estimated by searching for the phrase “diamond anvil cell” using the program *SciFinder Scholar* which searches the *CAplus* [31] literature database.

### 2.2.1 Equation of State

The fundamental quantity that is varied in a high pressure experiment is the relative volume of the material. The thermodynamic definition of pressure is  $P = -(\partial E/\partial V)_T$  where  $E$  is the average energy,  $V$  is the volume, and the subscript  $T$  represents constant temperature. Thus, a measurement of volume versus pressure (the equation of state) provides a knowledge of how the bulk energetics of the system depend on volume. Furthermore, we'll see in Section 2.4 that many condensed matter properties can be understood on the basis of the average distance between the atoms, which derives directly from the equation of state. The change in volume with pressure is most commonly determined through x-ray diffraction experiments. Frequently, equations of state are listed in either the Birch-Murnaghan [32,33] or Vinet [34] forms, although other equations are sometimes used. The dependence of volume on pressure can also provide some information about crystal structures since in many cases there is either a sudden drop in volume or a somewhat more subtle change in the equation of state at the onset of a pressure induced structural phase transition.

Figure 2.3 shows the experimentally determined equations of state for several elemental solids, including the highly compressible alkali elements as well as less compressible Au and diamond. Compressibility generally decreases under pressure and is given by  $1/B$  where the bulk modulus is given by  $B = -V(\partial P/\partial V)$  and  $V$  is the volume. The most compressible of the elements is  ${}^3\text{He}$ . It was recently found that osmium, being very slightly less compressible than diamond, is the least compressible of the elements [44]. Note that as one travels down the column of the alkali elements, the compressibility progressively increases. This is because the heavier alkali elements, having larger  $Z$ , do a better job of screening the Coulomb interaction between the outer valence electron and the nucleus, leading to a comparatively larger atomic radius and lower density.

### 2.2.2 Effect of Pressure on Superconductors

Drickamer has emphasized [45] that the primary effect of a change in temperature is to modify the occupation of the energy levels in a system while the primary effect of pressure application is to modify the energies of the levels. Thus temperature and

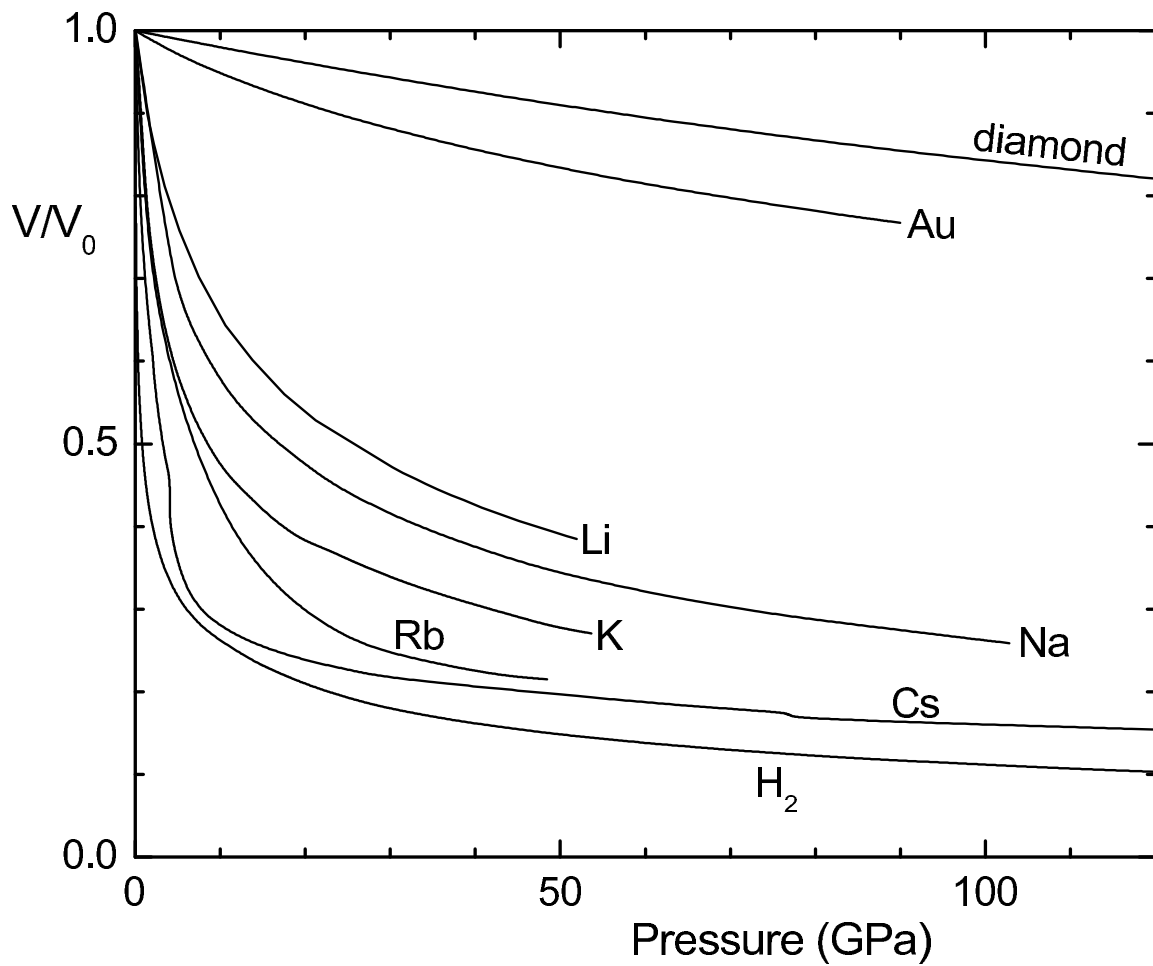


Figure 2.3: Dependence of relative volume ( $V/V_0$ ) on pressure for several elemental solids. Steeper slope indicates higher compressibility. Note the sudden volume collapses visible near 5 and 75 GPa for Cs; these occur transitions between different crystal structures. Data from References [35] diamond, [36] Au, [37, 38] Li, [39] Na, [40] K, [40] Rb, [41] Cs, and [42, 43] H.

pressure studies provide complementary information. Since the critical temperature of a superconductor depends on both lattice and electronic properties, one in general expects pressure to have a profound and possibly complicated effect on  $T_c$ . High pressure studies can advance the field of superconductivity in at least three important ways: (1) test theoretical models and reveal systematic trends, (2) improve the properties of known superconductors and (3) create new superconductors.

To explore the effect of pressure on superconductivity, we return to Equation 2.1 and make a harmonic approximation  $\omega_D \approx \langle \omega \rangle \approx \sqrt{k/M}$ , where  $k$  is the lattice spring constant and  $M$  is the cation mass. We use the McMillan expression [46] for the electron-phonon coupling parameter

$$\lambda = \frac{N(E_F) \langle I^2 \rangle}{M \langle \omega^2 \rangle}, \quad (2.8)$$

where  $\langle I^2 \rangle$  and  $\langle \omega^2 \rangle$  are the average square electronic matrix element and average square phonon frequency respectively. We define the Hopfield parameter  $\eta \equiv N(E_F) \langle I^2 \rangle$  [47]. For simplicity we set  $k_B = \hbar = 1$  and assume  $M \langle \omega^2 \rangle \approx M \langle \omega \rangle^2 \approx M(k/M) = k$ . Neglecting the Coulomb repulsion (set  $\mu^* = 0$ ), one finds for weak coupling  $\lambda \simeq N(E_F)V_{eff}$ . Rewriting Equation 2.1 we obtain

$$T_c \approx \sqrt{k/M} \cdot \exp[-k/\eta]. \quad (2.9)$$

Immediately apparent in this expression is the standard isotope effect  $T_c \propto \sqrt{1/M}$ . Within the exponent we have  $\eta$ , a purely electronic term and  $k$ , a lattice term. The spring constant  $k$  increases under pressure due to lattice stiffening (leading to the positive curvature of the equation of state), and  $\eta$  also normally increases under pressure. The  $k$  inside of the exponent in Equation 2.9 outweighs the  $k$  in the prefactor so that an increase in  $k$  leads to a decrease in  $T_c$ . It is possible for  $T_c$  to increase if  $\eta$  increases more rapidly than  $k$  under pressure. Therefore,  $dT_c/dP$  depends on the relative magnitude of pressure induced changes in lattice versus electronic properties. In the simple metal superconductors like Al, Zn, In, Sn, and Pb, pressure-induced lattice stiffening dominates over the relatively modest changes in electronic properties so that  $T_c$  decreases rapidly under pressure in these materials. In the transition

metals,  $T_c$  may either increase or decrease under pressure. Reference [48] contains an extensive review of the effect of pressure on superconducting materials. We will return to the simple picture presented by Equation 2.9 as we discuss superconductivity in the elements in the next section.

## 2.3 Superconductivity of the Elements

At ambient pressure 30 of the elemental solids are known to become superconducting at low enough temperature. Under sufficient pressure, an additional 22 elements become superconducting. Nearly half of the pressure induced superconductors were discovered prior to the 1980's by Jörg Wittig. Figure 2.4 summarizes the data on high pressure superconductivity for all of the elemental solids. Note the exceptionally high values of  $T_c$  observed for Y (19.5 K) [49], Sc (19.6 K), and Ca (25 K) [50]. For calcium the  $T_c$  value is higher than the highest  $T_c$  discovered for any *compound* during more than 70 years of superconductivity research prior to the discovery of the high- $T_c$  materials (see Figure 1.1). Several of the elements have  $T_c$  values that are still increasing with pressure at the highest pressure to which they have been studied [51] making it seem likely that higher  $T_c$  values will be discovered in the future. Thus, the pure elemental solids under extreme pressure can give us some insight into the question of the maximum possible  $T_c$  possible in a phonon-mediated superconductor. Is there any reason to think that the maximum achievable  $T_c$  in elemental solids should be lower than that in compounds? As Ginzburg and Kirzhnits [52] have explained, high  $T_c$  values should be sought in layered materials with a high degree of structural anisotropy (the high- $T_c$  cuprate superconductors fit this description). Among the elemental solids, such structures are rare, with graphite being one of the few examples.

Pickett has remarked [53] that a major deficiency in our understanding of conventional superconductivity concerns the inability to differentiate between elements like Y, Ca, or Nb, which display large  $T_c$  values in some pressure range, and other elements which display  $T_c$  values that are low or vanishingly small. For several of the elemental solids, the reasons for the lack of superconductivity are well known; while for others, the reasons are less clear.



Elemental solids that exhibit magnetic order, are not expected to become superconducting. These magnetic solids include Cr, Mn, Fe, Co, Ni, Ce through Tm, Cm, Bk, and Cf. Both Pd and Pt are nearly magnetic and superconductivity is suppressed by magnetic fluctuations in these elements. Fe and Ce, both magnetic at ambient pressure, become superconducting at high pressure following pressure-induced destruction of magnetism. Section 2.4.1 discusses the effect of pressure on magnetism.

Insulating solids will not superconduct; however, under pressure, O, P, S, Se, Br and I undergo an insulator to metal transition and become superconducting. The elements, B, Si, Ge, As, Sb, Te, and Bi have either either low or zero  $N(E_F)$  disfavoring superconductivity; under pressure they all become superconducting as they are driven from a metalloid/semiconducting state to a fully metallic state. Several of the non-metallic elemental solids have yet to be subjected to high enough pressure to drive them metallic. Among these, hydrogen has attracted the most attention. Following Wigner’s 1935 prediction of a metal insulator transition in hydrogen in 1935 [54], Ashcroft predicted in 1968 that solid metallic hydrogen ought be a superconductor with a  $T_c$  near room temperature [55]. This very high  $T_c$  is, in part, expected because of the low mass of H which leads to an enhancement of  $T_c$  according to Equation 2.9.

The alkali metals have exceptionally low ( $T_c \sim 0.4$  mK for Li) or vanishing  $T_c$  at ambient pressure. Here the reason for the suppression of superconductivity is somewhat less obvious, but it appears that the low Debye frequency  $\omega_D$  combined with near zero Hopfield parameter  $\eta$  serves to keep  $T_c$  of the alkali metals near 0 K [55]. Given that the alkali metals are simple metals, one would not expect  $T_c$  to increase under pressure. However, under pressure, Li and Cs are both superconducting and the  $T_c$  value for Li near 30 GPa is among the highest observed in the elements. Superconducting Li is discussed in more detail in Section 4.2. Under pressure, Cs ceases to be a simple metal and becomes a transition metal due to pressure induced s-d transfer; thus, the appearance of superconductivity is not completely unexpected.

Upon examining Figure 2.4 one may immediately note that nearly all of the d-electron metals (metals with a partially filled d-band) are ambient pressure superconductors. It is well known that conduction d-electrons aid superconductivity. In the transition metals, the s-,p-electrons are free-electron-like, while the d-electrons are

well modeled by tight binding bands [56]. The narrow d-bands have a comparatively high density of states. Examination of Equation 2.1 makes it clear that a high density of states at the Fermi level is favorable for superconductivity. The only non-magnetic d-electron metals that do not superconduct at ambient pressure are the Sc, Y and Lu, Ac, and the noble metals Cu, Ag, and Au. The reasons for the failure of these elements to superconduct at ambient pressure is discussed in detail in Section 4.1.2.

## 2.4 A Useful Ratio: Volume per Atom versus Ionic Volume

The basic effect of increasing pressure on a solid is to bring the atoms closer together. It is natural to compare the length scale of the atomic separations to another length scale, namely the size of the ions within the solid. The size of an ion can be quantified in a number of different ways. One can measure size by the radius where the electronic charge density of the localized electrons reaches a maximum (or where the charge density drops off to say 90% of the maximum value). Such radii are generally determined through calculations of electronic wavefunctions in isolated ions which have been extensively tabulated [57,58]. Alternatively, one could use ionic radii determined empirically through studying a variety of ionic crystals and assuming close-packing of hard spheres (for a further discussion of how this is accomplished, see Reference [14]). There are other methods for estimating radii (one is discussed in Section 2.4.2), but the results are similar: ionic radii are typically on the order of 1 Å. Usually, one assumes that these radii do not change significantly under pressure. However, at high enough pressure this assumption will break down. Note that the energy scale (ionization energy) of valence electrons in an atom is typically a few eV while the volume of the valence electron orbitals are a few cubic Angstroms; one could then define a pressure scale for the valence electrons in an atom as  $1 \text{ eV}/\text{Å}^3 \sim 1.6 \text{ Mbar}$ .

In Figure 2.5 (left) we show schematically a solid at low pressure where the volume per atom (dashed circle) is large compared to the ionic volume (solid, filled circle) and in Figure 2.5 (right) we show the same solid at high pressure where the volume per atom is nearly equal to the ionic volume. Volume per atom can be expressed by

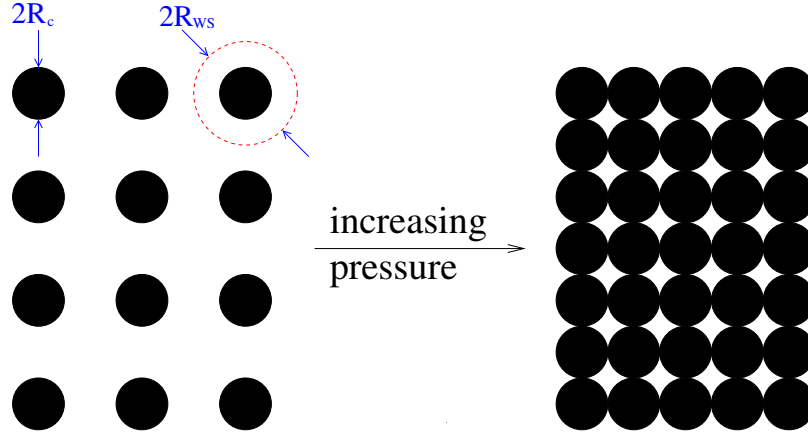


Figure 2.5: Schematic of solid at low pressure (left) and high pressure (right).  $R_c$  is the radius of the ion core and  $R_{WS}$  is the radius determined by the average volume available per atom in the solid. When  $R_{WS} \sim R_c$ , the localized electronic orbitals of the ions begin to overlap.

the Wigner-Seitz radius

$$R_{WS} \simeq \left[ \frac{3V_a}{4\pi} \right]^{\frac{1}{3}}, \quad (2.10)$$

where  $V_a = V/N_A$  is the average volume per atom given by the molar volume,  $V$ , divided by Avogadro's number,  $N_A$ . One ought to expect various material properties to change significantly when the lattice is compressed to the point where ionic cores begin to overlap ( $R_{WS} \sim R_c$ ) [59]. The ratio of these two length scales can be used to describe a wide variety of condensed matter properties. Below we consider three such properties that are all intimately linked to superconductivity: magnetic ordering, which generally destroys superconductivity, metallic versus insulating character (superconductivity occurs only in metals) and crystal structure, which is a key consideration in both the theoretical and empirical approaches to the search for new superconductors.

### 2.4.1 Magnetism

In the isolated neutral atomic state, most of the elements (nearly 75%) have a well-defined magnetic moment. Upon condensation into the solid state most of the elements lose their magnetism so that only 25% of the pure elemental solids are magnetic. This destruction of magnetism occurs because of interactions between the orbitals of

neighboring atoms (for a more complete discussion see, for example, Reference [14]). One expects that when the magnetic orbitals of neighboring atoms overlap magnetism is suppressed. The degree of orbital overlap can be quantified by the ratio  $\alpha \equiv R_{WS}/R_{mo}$  where  $R_{WS}$  was defined above (Equation 2.10) and  $R_{mo}$  is the radius of maximum charge density for the magnetic orbital. For example, scandium has the electronic configuration  $[Ar]3d^12s^2$ ; the magnetism of the isolated atom arises from the partially filled d shell. Thus, for scandium,  $R_{mo}$  is given by the charge density maximum of the  $3d-\frac{3}{2}$  orbital. Orbital radii for atoms and ions have been calculated and tabulated by Waber *et al.* [57]. Figure 2.6 shows  $\alpha$  plotted for all the elements with  $Z \leq 98$ . Remarkably, one can choose a critical value  $\alpha_c$  such that elements above

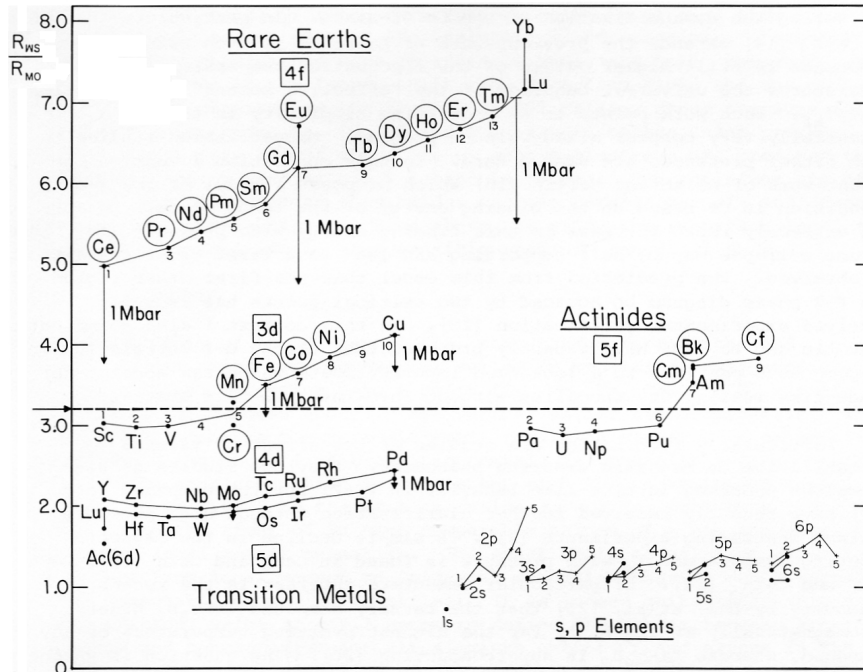


Figure 2.6: The ratio  $\alpha = R_{WS}/R_{mo}$  for the elemental solids with  $Z \leq 98$ . The horizontal dashed line shows  $\alpha_c \simeq 3.2$  and separates elements which are magnetic in the condensed state from those that are nonmagnetic. Circled elements are magnetic in the condensed state. The small numbers next to the points indicate the number of p, d or f electrons. Figure adapted from Reference [60].

this critical value are magnetic and those below are nonmagnetic. Only Cr and O have  $\alpha < \alpha_c$  and retain their magnetism. A particularly useful feature of this picture is that if one knows the equation of state (volume versus pressure) it is straightforward

to estimate the pressure required to destroy the magnetism. For example, note that iron (Fe) is quite close to the critical value implying that a relatively small pressure should be necessary to destroy its magnetism. Indeed a pressure of  $\sim 15$  GPa has been found to destroy magnetism (and induce superconductivity) in iron [61].

#### 2.4.2 The Goldhammer-Herzfeld Criterion for Metallization

A very old and often considered question in condensed matter physics is that of which properties give rise to metallic versus insulating character [62]. Today, the most common description is that metals contain a partially filled conduction band while insulators have a completely filled valence band separated by a large gap from an empty conduction band. The modern theory of band structure provides a comprehensive picture of the behavior of electrons in a solid however, accurately predicting such band structures generally requires powerful computers and sophisticated computational techniques. Long before the theory of band structure in solids was developed, Goldhammer [63] and later Herzfeld [64] developed a simple and remarkably accurate theory able to account for the onset of metallic character.

The Goldhammer-Herzfeld (GH) criterion is based upon the Lorenz-Lorentz or Clausius-Mossotti relation

$$\frac{n^2 - 1}{n^2 + 2} = \frac{\varepsilon - 1}{\varepsilon + 2} = \frac{4\pi\alpha}{3V}N_A = \frac{R}{V}, \quad (2.11)$$

where  $n$  is the index of refraction,  $\varepsilon$  is the relative permittivity,  $\alpha$  is the molecular polarizability,  $V$  is the molar volume,  $N_A$  is Avogadro's number and  $R \equiv (\frac{4}{3}\pi\alpha) N_A$  is called the molar refractivity. Clearly, as  $R/V \rightarrow 1$ ,  $n \rightarrow \infty$  and  $\varepsilon \rightarrow \infty$ ; this can only happen if electrons are no longer bound, as in a metal. Thus, the GH criterion is

$$\begin{aligned} R/V < 1 &\implies \textit{insulating} \\ R/V \geq 1 &\implies \textit{metallic}. \end{aligned} \quad (2.12)$$

A simple physical interpretation of the GH criterion becomes apparent when one notes that the polarizability of a conducting sphere of radius  $r$  is equal to  $r^3$  [65]. That approximating the atom as a conducting sphere can produce reasonable radii is clear if one considers for example the polarizability of Ar,  $\alpha \sim 0.988 \text{ \AA}^3$  [66]

so that  $r = \alpha^{1/3} \sim 1 \text{ \AA}$ . Now, the meaning of  $R$ , the molar refractivity, becomes clear:  $R = (\frac{4}{3}\pi\alpha) N_A$  is nothing more than a measure of the volume occupied by one mole of conducting spheres. Usually  $R$  can be taken to be independent of density<sup>1</sup> allowing straightforward estimates of metallization density given a knowledge of the atomic/molecular polarizability. Imagine compressing a material where initially  $R/V < 1$  which means that  $r < R_{WS}$  (in analogy to the situation shown at the left of Figure 2.5). The material is insulating because the “conducting spheres” do not overlap. Upon increasing the pressure  $R/V$  increases to 1 and the spheres touch. At this and higher pressures, when  $R/V \geq 1$  the material is metallic because the conducting spheres overlap, allowing the electrons to freely wander throughout the material.

The accuracy of the simple GH criterion with respect to the metallic character of elemental solids is strikingly illustrated in Figure 2.7; note that as one scans from left to right across the figure, the elements of the periodic table turn from metal to non-metal around columns 13-16 just as the  $R/V$  values curve below the dashed line at  $R/V = 1$ . If we define  $V_0$  as the ambient pressure volume and  $V_c$  as the critical pressure for transition to the metallic state, it is clear that metallization occurs when the relative volume  $V_c/V_0 = R/V_0$ . As an example, consider Xe. From Figure 2.7  $R/V_0 \sim 0.29$  for Xe leading one to expect Xe to become metallic when compressed to the point where  $V/V_0 \sim 0.29$ . According to the measured equation of state of Xe [69], one would expect to reach this relative volume at a pressure of  $\sim 150$  GPa. Indeed this is approximately the pressure where Xe is found to enter the metallic state [70–72]. In many cases the prediction of the GH criterion is as accurate as significantly more complicated theoretical treatments such as the augmented plane wave (APW) method [73]. In Appendix A we list calculated  $R/V$  values for several compounds and in Section 4.2.3 we’ll return to the GH criterion in the context of the search for superconducting low- $Z$  materials.

---

<sup>1</sup>There are cases where  $R$  changes significantly with density, causing the GH criterion to fail. Some of these cases are discussed in Reference [67].

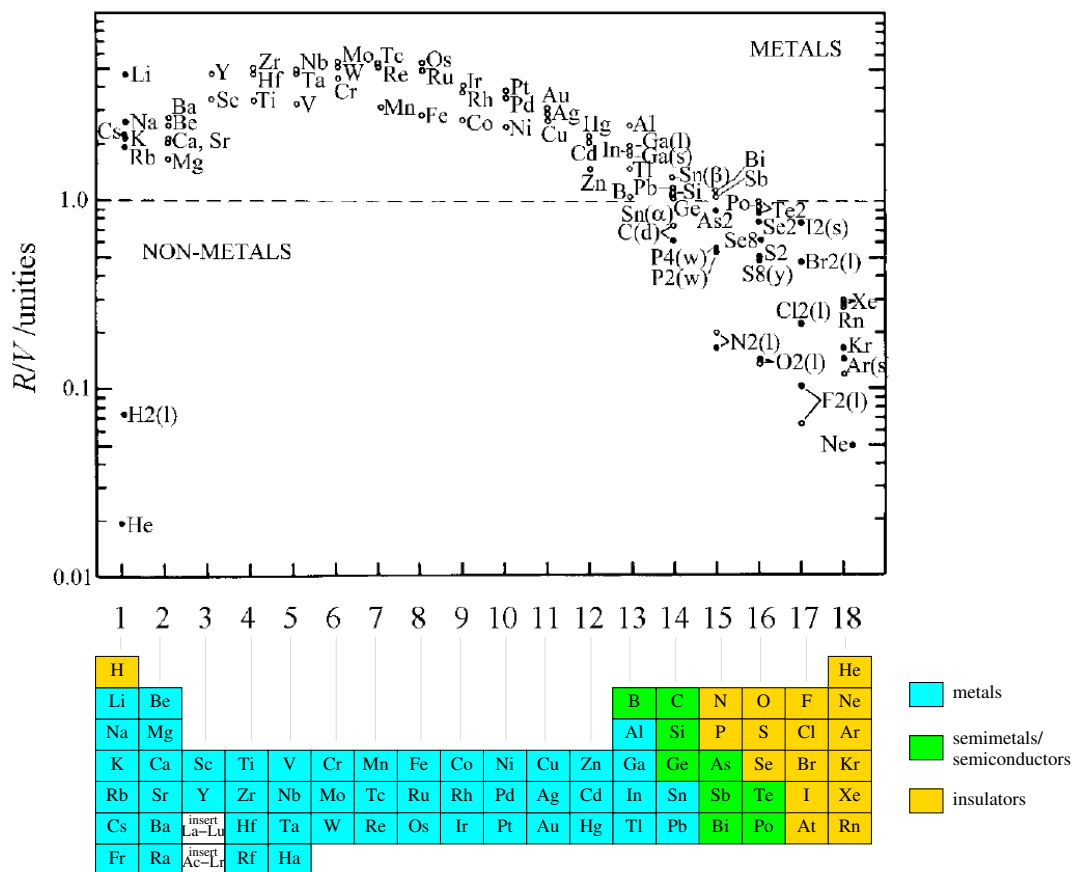


Figure 2.7: Top of figure (reproduced from Reference [68]) shows  $R/V$  versus column in the periodic table for the elemental solids. The periodic table at the bottom of the figure shows the empirically known character of the elemental solids. The dashed line at  $R/V = 1$  separates the metals from the non-metals according to the GH criterion. The lanthanide and actinide elements have been omitted for clarity.

### 2.4.3 Structure Sequence of Rare-Earth Elements

The lanthanides consist of elements La (57) through Lu (71) and are characterized by a gradual filling of the f-shell. Despite the large range in the number of f-electrons across the lanthanide series, at ambient pressure these elements share many characteristics because the highly localized f-orbitals play no role in bonding and electronic structure which are determined by s-, p- and d-electron contributions. Often, Y and Sc are included in discussions of the lanthanides because of their similar conduction electron structure. We will adopt the convention of referring to the lanthanides plus Y and Sc as the *rare-earth* elements.

A notable property of the elemental solids is that as a function of atomic number or hydrostatic pressure their crystal structures appear in certain regular sequences [74]. This is particularly true in the lanthanide elements. Systematic studies of pressure induced phase transitions in the lanthanides were among the earliest experiments to exploit the expanded pressure range made possible by the diamond anvil cell [75]. Table 2.4.3 shows the structures adopted by the rare-earth elements at ambient and high pressure. The vertical arrows indicate increasing pressure. Most of the structures displayed by the rare earths are closely related and are just different stacking sequences of hexagonally close-packed layers [25]. That the f-electrons do not determine the structures of these elements is confirmed by the fact that yttrium, with no f-electrons, displays the same structures as the lanthanides. The elements surrounded by parenthesis, Eu and Yb display anomalous structures; they are anomalous because they are divalent, unlike the rest of the members of the rare-earth series which are trivalent. Both Eu and Yb appear to undergo a divalent to trivalent crossover at high pressure [76–78]. Ce is particularly interesting because only 0.7 GPa is required to drive Ce from a magnetic to a non-magnetic state, both in the fcc structure. This was perhaps the earliest confirmed example of a pressure induced isostructural electronic transition [75, 79].

Excluding the anomalous elements Eu and Yb, one notes that the “regular” members of the lanthanide series exhibit the same sequence of structures from heavier to lighter elements across the series as they exhibit under increasing pressure. Experiments have also shown that this structure sequence appears upon alloying lighter



lanthanides into the heavier ones. This result may at first seem puzzling given that the volume available per atom *decreases* across the series ( $R_{WS}$  varies nearly linearly from 2.08 Å for La to 1.92 Å for Lu [80]). Since the effect of pressure is to decrease  $R_{WS}$ , one might expect that pressure should produce structure sequence exhibited by moving across the series from lighter to heavier elements, the opposite of the observed behavior.

An elegant understanding of these trends was developed by Johansson and Rosengren [81]; noting that the *ratio*  $R_{WS}/R_I$  of the Wigner-Sietz radius to the ion core radius increases nearly linearly across the series, they were able to construct a single generalized phase diagram for the rare-earth elements. Assuming that crystal structure is correlated with the ratio  $R_{WS}/R_I$  leads one to the correct prediction that pressure should produce the same structure sequence as moving from right to left across the series, since both have the effect of decreasing this ratio.

Approximating the core radius as the radius of maximum charge density of the 5p orbital, Krüger *et al.* [82] found that the structural transitions occurred at specific values of the ratio  $R_{WS}/R_{5p}$  and beautifully illustrated the accuracy of the correlation in a plot reproduced in Figure 2.8. First, notice the solid black points in this figure; they indicate the ambient pressure values of the ratio  $R_{WS}/R_{5p}$  which increase linearly across the series as pointed out by Johansson and Rosengren [81]. Next, note the open square data points, representing the pressure induced transition from the hcp to Sm-type structure. To a very good approximation, the hcp to Sm-type transition occurs at a single critical value of  $R_{WS}/R_{5p}$  for all of the rare earth elements that exhibit this transition. Critical values are likewise found for the Sm-type to dhcp and dhcp to fcc transitions. The ratio  $R_{WS}/R_{5p}$  does a remarkable job of describing the structures of the rare earths over a tremendous range of pressure. For example the hcp to Sm-type transition occurs at only  $\sim 3$  GPa in Tb while for Lu it occurs at  $\sim 18$  GPa.

In detailed calculations, Duthie and Pettifor [83] have shown that these structures are determined by the occupancy of the d-band, and that the relative volume of the ion core is directly related to the d-band occupancy. In Section 4.1.2 we'll explore a correlation between superconductivity, the relative volume of the ion core and d-band occupancy in the non-magnetic rare-earth elements.

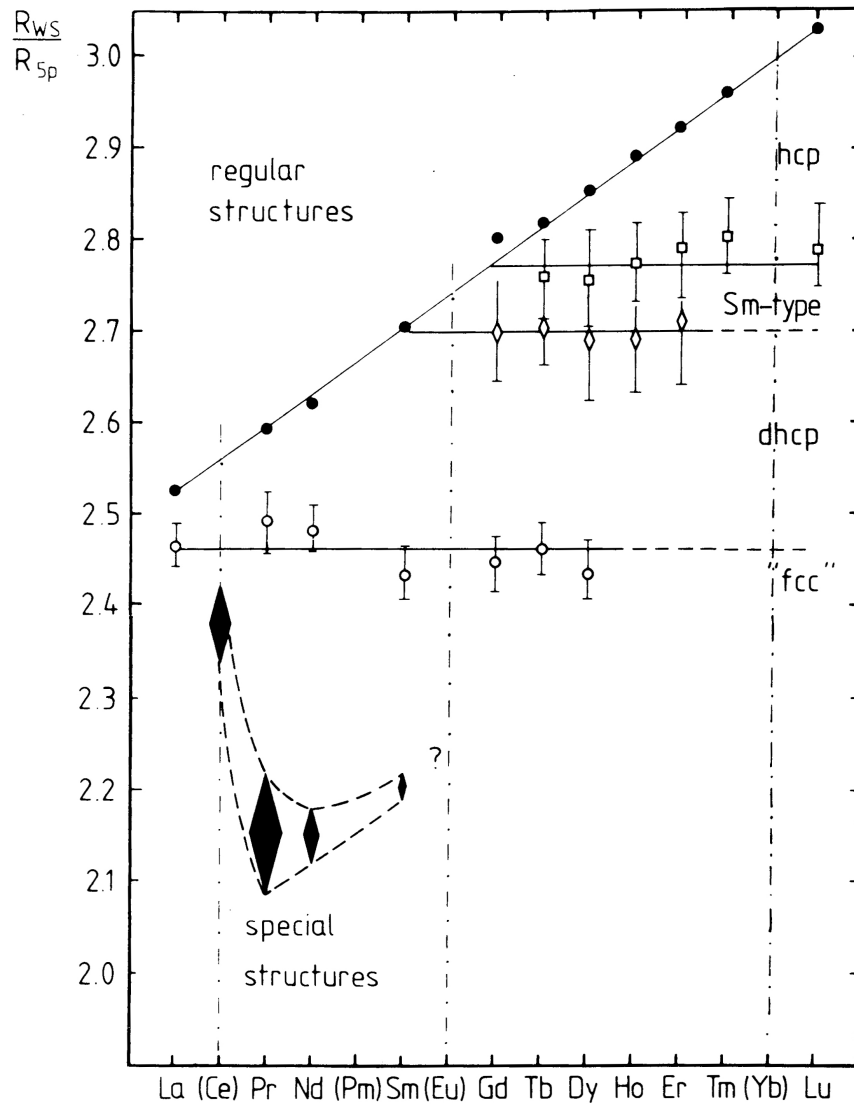


Figure 2.8: Filled circles show ambient pressure values of the ratio  $R_{WS}/R_{5p}$ . Open data points show critical values of the ratio for structural phase transitions. Horizontal lines give critical values of the  $R_{WS}/R_{5p}$  for structural transitions for the rare earths. The large filled diamonds indicate volume collapse phase transitions possibly associated with f-electron delocalization. Figure reproduced from Krüger *et al.* [82].

## Chapter 3

# Experimental Apparatus and Methods

### 3.1 Diamond Anvil Cell

The majority of the experiments described in this dissertation were carried out using a piston-cylinder diamond anvil cell designed by J. S. Schilling [60]. A cut-away view of the cell is shown in Figure 3.1. The cell is constructed of Cu-Be alloy, except for parts near the sample and pickup coils which are made from non-magnetic Cu-Be alloy. To insure stable alignment of the diamond culets, the difference in diameter between piston and the cell bore should be less than  $\sim 10 \mu\text{m}$ . Over time the piston and cylinder are gradually worn away resulting in a poor fit between the piston and cylinder. In order to remedy this problem, the piston is periodically electroplated with copper and then polished to a close fit with the bore using 0.25-1  $\mu\text{m}$  diamond lapping compound. For details on the electroplating process see the DAC manual. Force is applied in this cell using a stainless steel membrane (double-diaphragm press) designed by B. Daniels [84]. By applying moderate gas pressure to the membrane, large forces can be applied to the diamonds. He gas is used to pressurize the membrane because pressurized helium has a lower melting point than any other gas. At 140 bars the melting point of helium reaches approximately 4.2 K and the melting point does not exceed 1.55 K (the lowest temperature accessible using the Oxford cryostat) until the pressure reaches  $\sim 26$  bars [85]. The membranes used in this dissertation research

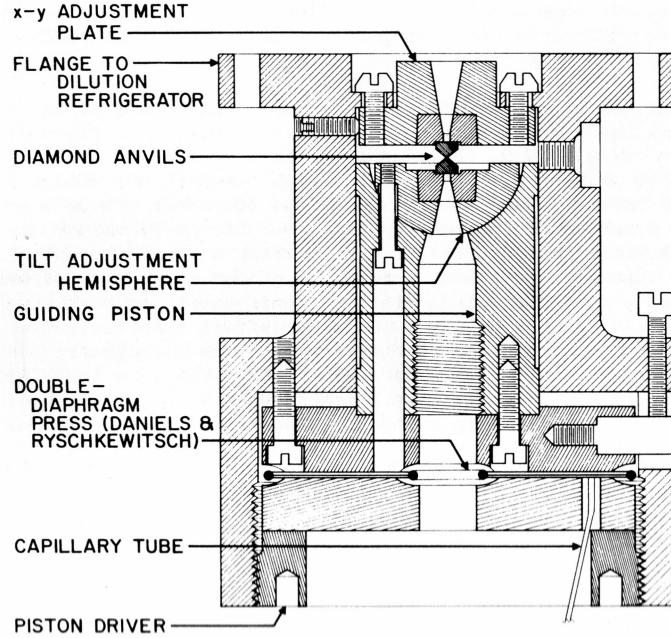


Figure 3.1: Cross-sectional view of the diamond anvil cell designed by J. S. Schilling [60].

produce  $\sim 130$  N (13.3 kg force) per bar of gas pressure. Membrane loading has the advantage that pressure may be changed at any temperature above the melting point of the loading gas (helium). Mechanical loading methods often require that the clamp be removed from the cryostat in order to change the pressure. The applied force is determined very accurately by the gas pressure applied to the membrane. A needle valve allows fine control of the pressure applied to the membrane. A reservoir volume at room temperature insures that the pressure applied to the membrane changes by less than 1% between room temperature and 1.55 K.

The diamond anvils sit atop a small cylinder of *backing material*. The backing materials used with the Schilling clamp have a 1 mm cylindrical hole allowing optical access to the sample with semi-angle<sup>1</sup>  $7^\circ$ . A finite element method (FEM) analysis of the strains present in anvil and backing material suggest that lower strains are produced when the hole in the backing material is a cone, strains reaching a minimum when the cone semi-angle is  $25 - 30^\circ$  [86]. A conical hole in the backing material also allows better imaging and light collecting. The backing material must be very

<sup>1</sup>Here, the semi-angle is the angle between the optical axis and the steepest exiting ray.

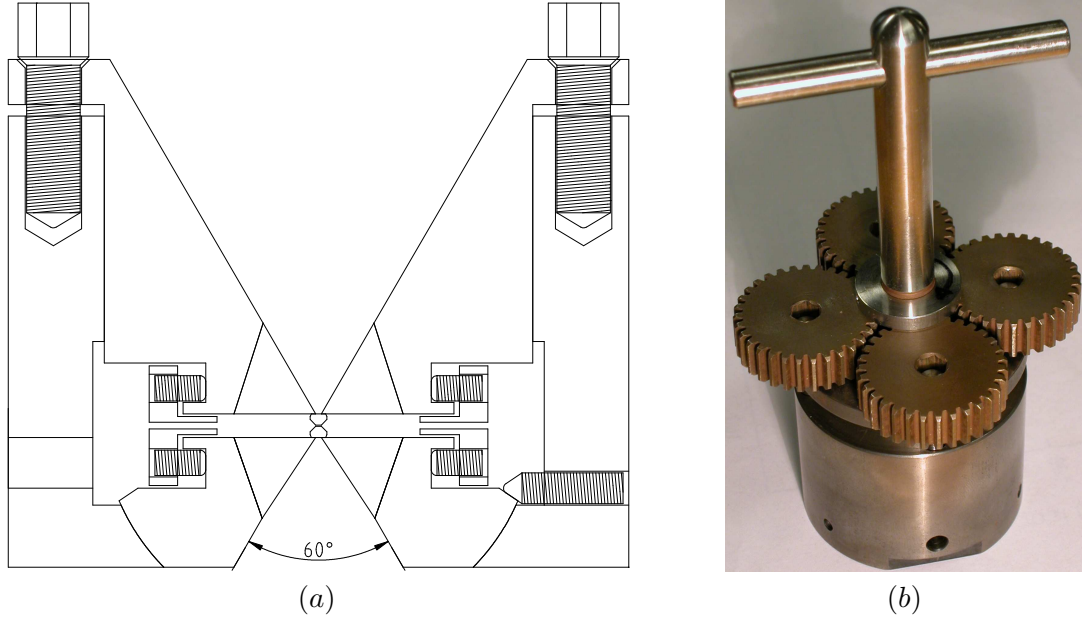


Figure 3.2: The mechanically loaded DAC designed by R. Boehler. (a) Cross-sectional plan of the Boehler cell showing the  $60^\circ$  aperture for optical measurements. (b) Photograph of the DAC and loading mechanism.

tough as pressures at the diamond table can be large. For most experiments in this dissertation, 1/6-carat diamonds are used which have a table diameter of approximately 2.5 mm. The membranes are usually loaded to a maximum pressure of  $\sim 140$  bars, corresponding to an applied force of  $\sim 18340$  N (1870 kg force). This creates a pressure at the table of about 4.5 GPa. Thus, the backing material must have a hardness of greater than  $\sim 450$  HV0.5 in order to withstand plastic deformation at the highest loading forces (this measure of hardness is described in Section 3.3). Plastic deformation of the backing material during an experiment could lead to misalignment and catastrophic failure of the anvils. Two types of backing material were used in this research, tungsten-carbide (WC) and a Ni-Cr-Al precipitation alloy (discussed below). Both materials meet the requirement for hardness (see Table 3.1). The WC material is hard enough that small imperfections in the surface of the backing material could lead to excessive strain in the diamonds. Therefore, when using WC backers, a  $25 \mu\text{m}$  thick Zr foil is placed between the diamond and backing material in order to reduce strain. The Zr foil is unnecessary in the case of softer backing materials.

For studies at room temperature we have used a mechanically loaded diamond anvil cell designed by R. Boehler. Force is applied using a system of gears (see Figure 3.2) which allow at least 6380 ( $\sim 650$  kg force) to be applied by hand turning the loading handle with minimal effort; higher forces are likely possible but have not yet been attempted. The gears guarantee that all four screws are tightened concurrently, insuring that pressure is applied uniformly to the diamond culets. The cell is made of magnetic stainless steel and is therefore not suitable for ac magnetic susceptibility studies; however, the large angle (semi-angle  $30^\circ$ ) of the light ports makes this cell ideally suited to optical studies. The backing material of this cell is WC.

### **Gasket**

A key component of the diamond anvil cell is the gasket. The gasket reduces the strain at the diamond culets and makes it possible to surround the sample with a pressure medium. Metal foils with thickness  $\sim 250 \mu\text{m}$  were used for all the experiments in this dissertation. The foils are first preindented to a thickness dependent on the diameter of the diamond culet. The term “culet” refers to the flattened tip of the diamond anvil; it is the part of the diamond that experiences the greatest pressure. The preindented thickness should be approximately  $1/9$  of the culet diameter and  $1/3$  of the hole diameter [87]. The hole is drilled through through the center of the pre-indented area by electro-discharge machining (EDM). Depending on the sample and pressure medium, the initial diameter of the hole should be adjusted so that it reaches  $1/3$  of the culet diameter at high pressure. When using highly compressible He pressure medium the initial hole diameter should be  $1/2$  the culet diameter [88]; at high pressure the hole diameter then shrinks to  $\sim 1/3$  of the culet diameter. This is also the case when one uses no pressure medium, where usually, as much as 70% of the cell volume is initially empty. Smaller diamond culets allow higher pressures with lower applied force. Figure 3.3 shows the sample pressure versus membrane pressure for experiments with a variety of different culet diameters.

Successful experiments to high pressure place strict requirements on the gasket material. The gasket material must be both hard and ductile. Generally ductil-

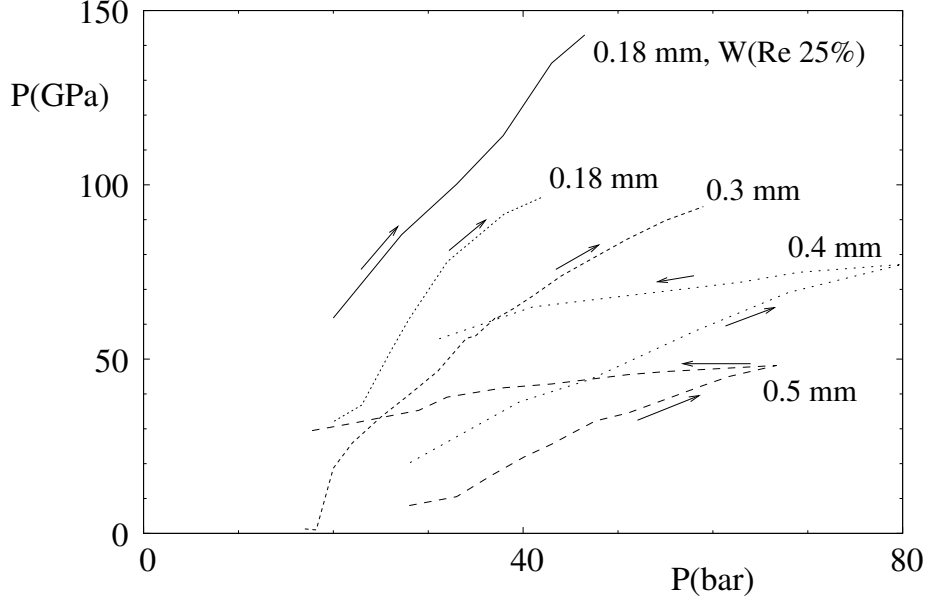


Figure 3.3: Sample pressure versus membrane pressure for experiments using a variety of culet diameters. All data except that marked “W(Re 25%)” was taken with Re gaskets. The curves marked “0.18 mm” were for diamonds beveled from 0.35 mm to 0.18 mm.

ity decreases with increasing hardness. If the gasket’s ductility is too low, it can suffer brittle failure under pressure, resulting in destruction of the diamonds. Several gasket materials were used during this dissertation work, including Re, W(Re 25%), Ni(Cr 39-41%)(Al 3-4%) [89] and Ni(Mo 15.3%). The percentages are given as atomic percent. The Ni(Mo 15.3%) gaskets were made by V. Tissen. The alloy Ni(Cr 39-41%)(Al 3-4%) is frequently referred to as “Russian Steel” or “Russian Alloy” and can be heat treated to adjust the hardness as described in Reference [89]. In this dissertation, we have frequently referred to this alloy simply as “NiCrAl”. The suitability of these materials as diamond anvil cell gaskets depends strongly on the method used to create the foils. Many of the rhenium foils we purchased worked very well as gaskets, but some of the foils were highly granular and displayed significant cracking on preindentation, making them unsuitable as gaskets. Under magnification, small microcracks on the order of 100  $\mu\text{m}$  long are visible in the rhenium foils that develop cracks during preindentation. The hardness values for rhenium foils having microcracks is significantly lower than that of foils without microcracks (see Table 3.1). Preindented gaskets should always be examined carefully for cracks before use.

Ac magnetic susceptibility measurements place a further restriction that the gasket material must remain non-magnetic and non-superconducting to low temperature. If the gasket is magnetic or superconducting, the signal from the gasket will obscure any signal from the sample (see Section 3.6). Pure Re metal superconducts at 1.4 K under ambient pressure, but under strain  $T_c$  increases to 4 K. The W(Re 25%) alloy superconducts at  $\sim 5$  K. Several of the gasket materials were tested in a Quantum Design PPMS system to determine their magnetic properties. The samples were punched out to 3 mm diameter disks (same dimensions as the gaskets). The results of those measurements are shown in Figure 3.4. Note the nearly linear magnetization curve for Ni(Mo 15.3%) in Figure 3.4 (b), which indicates that this material is free from ferromagnetic impurities.

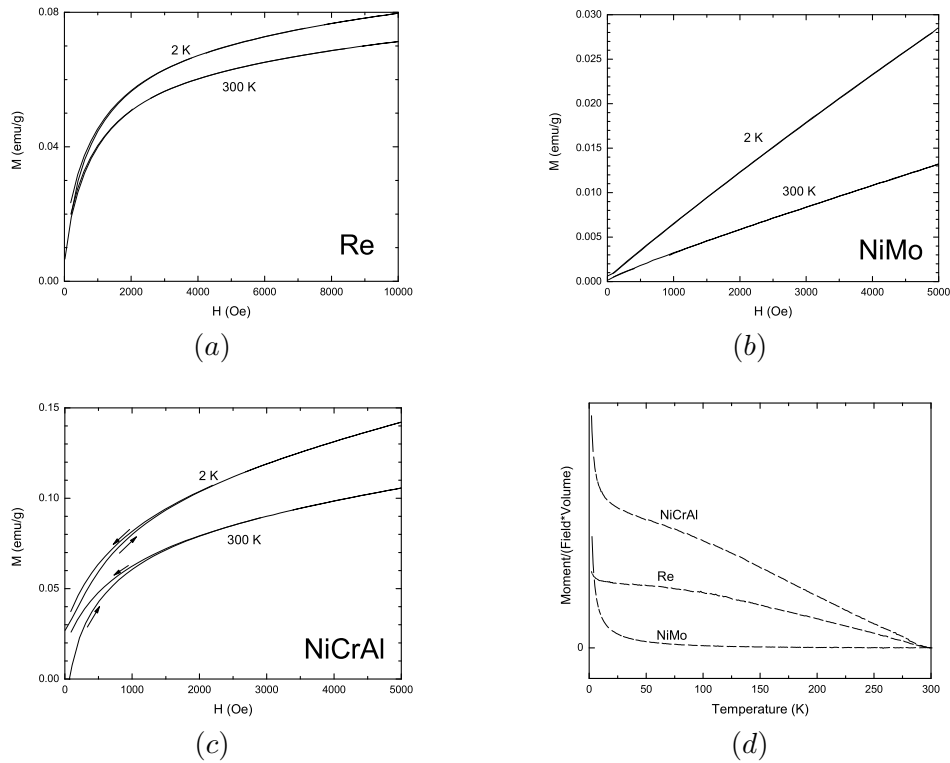


Figure 3.4: Magnetization data for various gasket materials. (a), (b) and (c) show magnetization versus field for Re, Ni:Mo and Ni:Cr:Al. Composition of the alloys is described in the text. (d) Magnetization versus temperature for each of the gasket materials tested. Curves were measured while cooling. Ni(Mo 15.3%) and Ni(Cr 39-41%)(Al 3-4%) were measured in a 5,000 Oe field and Re was measured in a 10,000 Oe field.

## 3.2 Cryostat

All of the low temperature measurements reported in this dissertation were performed using a custom, continuous-flow cryostat built by Oxford Instruments. The basic design of the cryostat is shown in Figure 3.5 (a). The cryostat is capable of operating between room temperature and 1.5 K using a 16 m<sup>3</sup>/h forepump on the helium bath. Optical access to the diamond anvil cell is provided through windows at the bottom of the cryostat and by an optical fiber entering through a feedthrough at the top of the cryostat. For more information on the windows see Appendix B. Electrical feedthroughs at the top of the cryostat provide connections for thermometry, ac susceptibility/resistivity, heating and a liquid helium level meter. An insulating vacuum isolates the low temperature sample space from the surroundings and a highly polished heat shield provides additional thermal isolation by reducing radiative heat transfer. During the course of this research, we took apart the cryostat to remove oil that had accumulated on the inner surface of the optical windows due to a malfunctioning diffusion pump. Photographs of the disassembled cryostat are shown in Figure 3.5 (b).

Temperature measurement is provided by calibrated thermometers fixed to the diamond anvil cell with thermal grease (Apiezon N) approximately one inch above the sample. Temperature gradients between the sample and thermometer, while slowly warming the sample, appear to be less than approximately 80 mK at 7 K; this was determined by measuring the superconducting transition of Pb, which has a precisely known  $T_c$  value. Two types of thermometers were used: a metallic platinum thermometer and a semiconducting germanium thermometer. At low temperature the resistivity of the platinum thermometer has very little temperature dependence, reducing the sensitivity of the temperature determination. Therefore, below 30 K, we measure temperature using the germanium thermometer. As temperature is decreased the resistance of the germanium thermometer goes up and so the sensitivity is greater at low temperature. At all temperatures the power delivered to the thermometers is kept less than  $\sim 1 \mu\text{W}$ , guaranteeing that no significant temperature gradients develop between sample and thermometer due to excess heating of the thermometer.

There are two separate modes of operation for the cryostat. Between room temper-

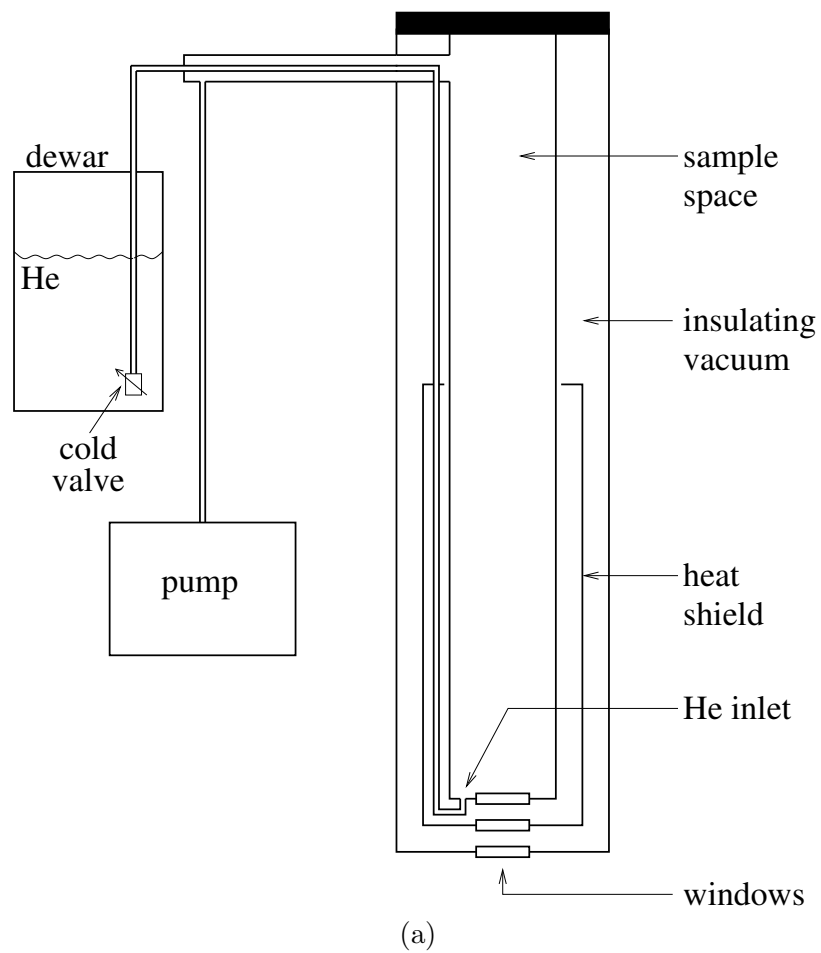


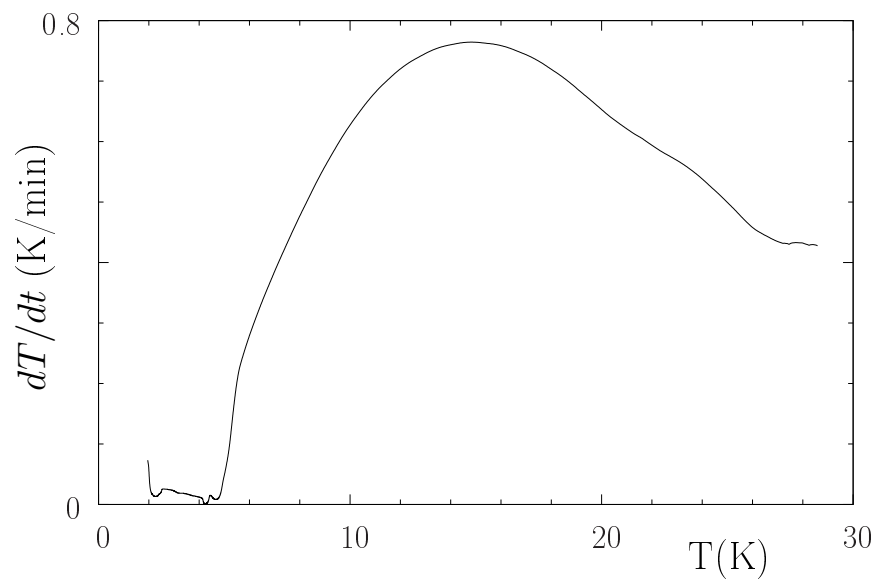
Figure 3.5: The Oxford Instruments continuous flow cryostat. (a) Schematic of the cryostat; not to scale. (b) Photograph showing the disassembled Oxford Instruments cryostat. At left is the outer cylinder, middle is the heat shield and right is the inner sample tube.

ature and 4.2 K (boiling point of liquid helium) a membrane pump creates a vacuum in the sample space which pulls liquid helium from the storage dewar, through the transfer tube, and into the cryostat through a permeable helium diffuser at the bottom of the cryostat. For cooling below 4.2 K, enough liquid helium is filled into the cryostat to completely submerge the DAC and thermometers (2-3 liters), the transfer tube is removed and the helium is evaporatively cooled by pumping with the 16 m<sup>3</sup>/h forepump. Using this method it is possible to cool the DAC to 1.55 K. Lower temperatures should be possible by employing a more powerful pump.

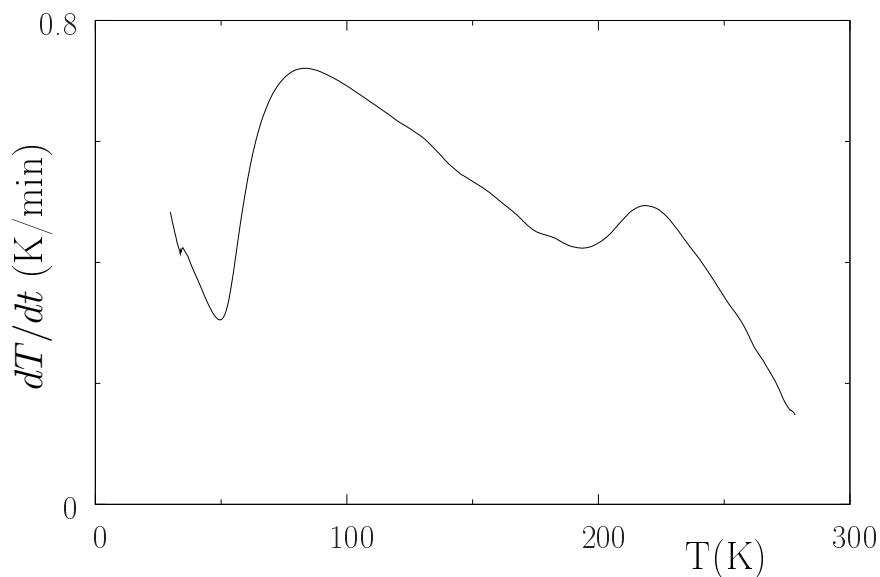
The ac magnetic susceptibility measurements described in Section 3.6 require stable, smooth temperature control in order to minimize induced noise in the ac-susceptibility signal. In addition, in order to perform the subtraction of background data, the temperature versus time profiles must be extremely repeatable from one measurement to another. The majority of superconducting transitions measured during the course of this dissertation work were at or below 20 K. This temperature range has a number of problematic areas, one being the region close to the 4.2 K boiling point liquid helium. The sudden accumulation or dissipation of liquid helium at 4.2 K can produce temperature gradients and rapid changes in the cooling and warming rate that are manifested as increased noise and large discontinuities in the ac-susceptibility or resistivity signal. The temperature range close the superfluid transition temperature of He ( $T_\lambda=2.17$  K) presents similar problems. As helium is cooled through the superfluid transition, heat is released, resulting in a change in the cooling rate at this temperature. In addition, above  $T_\lambda$  helium has a finite thermal conductivity while below  $T_\lambda$  the thermal conductivity of helium becomes infinite. These two factors can lead to spurious features in the data near  $T_\lambda$ . The impact of the effects described above was minimized by the development of three temperature control techniques.

Above 5 K, simply allowing the system to warm up naturally, without any active heating or cooling is sufficient; this method is referred to as *drift warming*. From 3.5 - 10 K a method employing simultaneous active cooling and heating is optimal. First, a constant power of 0.2 W is delivered to a heater near the bottom of the cryostat, and the cold valve (see Figure 3.5) is adjusted until the temperature becomes stable

at 10 K. Then, the current delivered to the heater is ramped down linearly causing the system to cool; this technique is referred to as *slow cooling*. This method allows the temperature to be lowered very slowly down to 3.5 K and no effect is observed at the helium boiling point, allowing accurate data collection near 4.2 K. Slower temperature sweep rates allow for longer integration times to be used on the ac-susceptibility measurement, thus reducing noise levels. At first, an PID (proportional-integral-derivative) temperature controller was used to adjust the heating current, but this resulted in temperature oscillations because the appropriate feedback parameters change significantly between 3.5 K and 10 K resulting in temperature oscillations; simply ramping the current down linearly results in much smoother temperature versus time profiles. Between 1.5 K and 4.2 K the best results were achieved by cooling as opposed to warming. The cooling rate was kept low by very slowly opening the valve between the pump and the sample space (in practice the valve was opened by a given angle every 30 s); this method is referred to as *liquid slow cooling*. The cooling/warming rate versus temperature profiles for the various temperature control methods described above are shown in Figures 3.6 and 3.7.

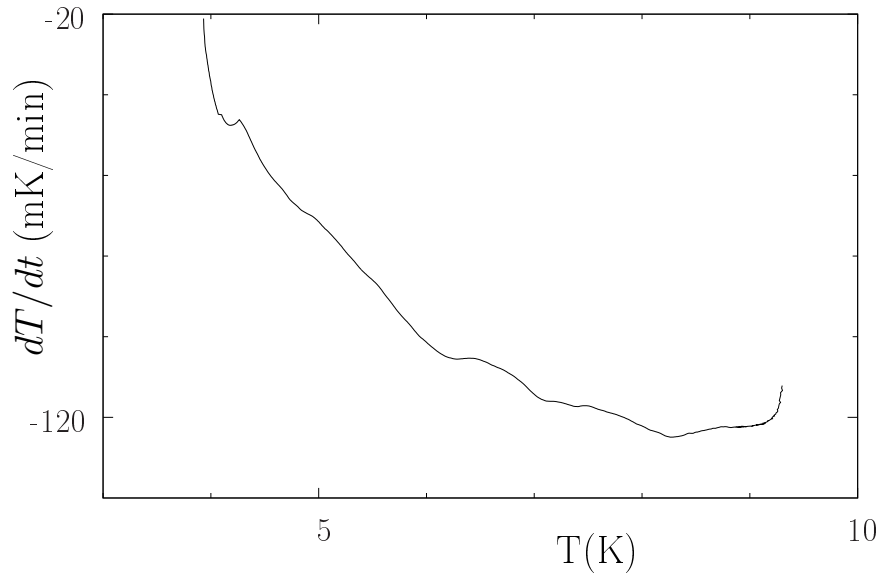


(a)

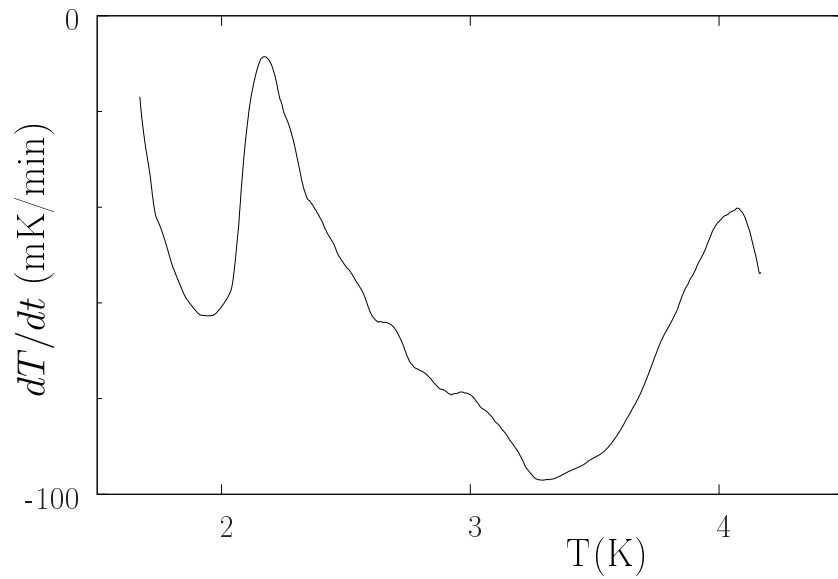


(b)

Figure 3.6: Warming rate versus temperature for the Oxford cryostat. (a) Rate when the system is allowed to warm without heating after being cooled to 1.6 K (*drift warming*). Note the minima in the warming rate at the liquid helium  $T_\lambda$  and  $T_{boil}$ . (b) Rate for *drift warming* to room temperature. For this measurement, the valve connecting the diffusion pump to the insulating vacuum is closed resulting in about twice the warming rate observed when the valve is kept open.



(a)



(b)

Figure 3.7: Cooling rate versus temperature for the Oxford cryostat. (a) Rate when system is cooled by applying a constant cooling power and slowly ramping down the heating current (*slow cooling*). (b) Rate when system is cooled below the helium  $T_{boil}$  by slowly increasing the pumping rate. Note that the cooling rate becomes very small as the system is cooled to  $T_\lambda$ .

### 3.3 Vickers Hardness

Hardness refers to the ability of a material to withstand plastic deformation and is, therefore, a very important parameter in many aspects of high pressure physics. Hardness is usually measured by pressing hardened indenter into the material to be tested with a specified amount of force and then measuring the penetration of the indenter into the test material. There are many different hardness scales based on differing indenter shapes and loads. In general, hardness values measured using different scales can only be converted using empirically determined relations. For comparison with hardness values reported elsewhere, the HV0.5 values can be converted to the Rockwell C (HRC) scale using the empirical relationship described in Reference [90] and shown in Figure 3.8.

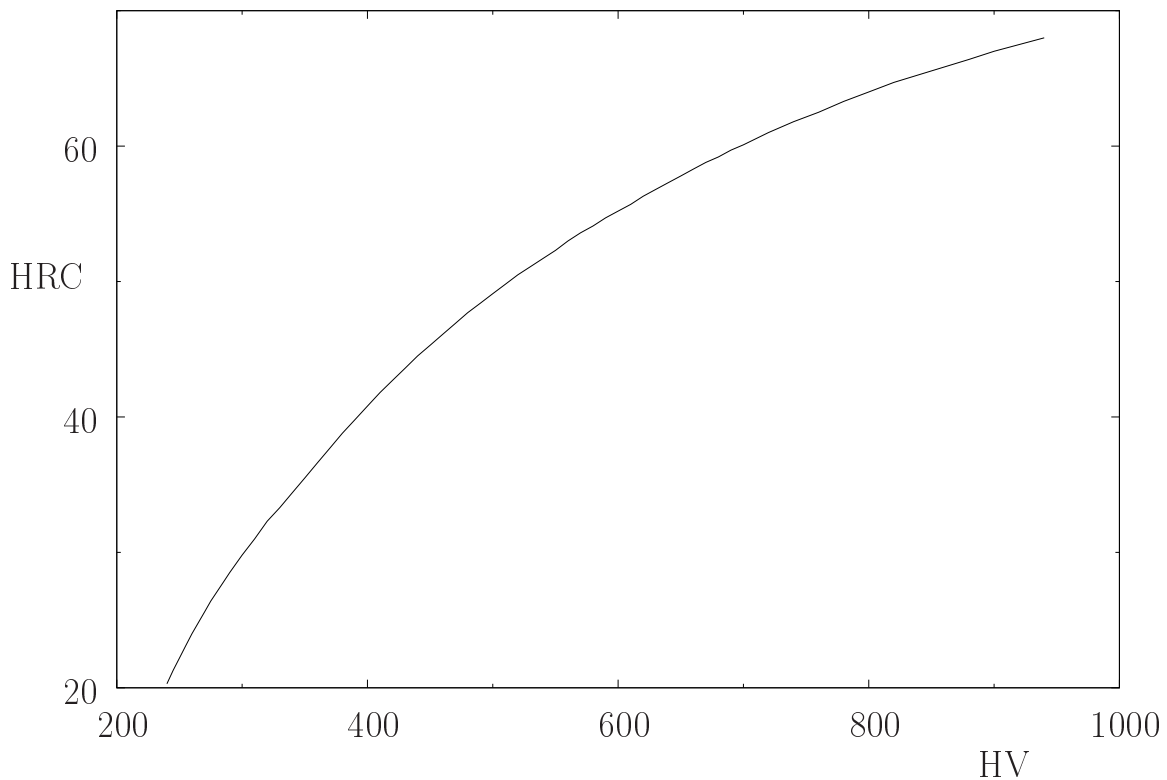


Figure 3.8: Empirical relationship between Vickers hardness and Rockwell C hardness as given in Reference [90].

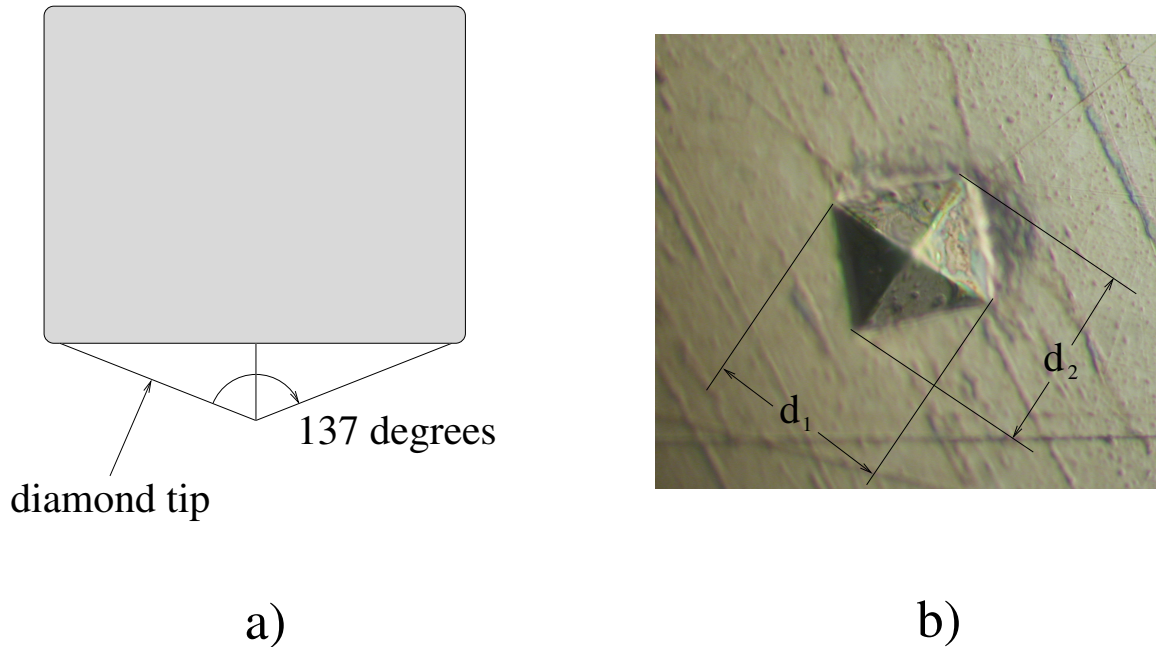


Figure 3.9: The Vickers hardness test. a) Geometry of the Vickers diamond indenter. b) Micrograph showing indentation and definition of diagonals  $d_1$  and  $d_2$ .

The Vickers hardness test was developed in the 1920's by the Vickers Ltd. company and uses a square-based pyramidal indenter with a 137 degree angle at the tip as shown in Figure 3.9 (a). The indenter is pressed into the test material for  $\sim 15$  seconds and then the two diagonals,  $d_1$  and  $d_2$ , shown in Figure 3.9 (b), are measured using a microscope with a calibrated scale. The Vickers hardness is given by

$$HV = \frac{F}{A} \approx \frac{1.854M(kg)}{d_1(mm)d_2(mm)}, \quad (3.1)$$

where  $M$  is mass pressing the indenter into the sample,  $A$  is the area of the indentation, and  $d_1$  and  $d_2$  are the diagonal lengths as shown in Figure 3.9 (b). Vickers hardness values are often reported in the form  $xxxHVyy$  where  $xxx$  is the hardness in  $\text{kg/mm}^2$  and  $yy$  is the load in kg force.

The interpretation of the exact physical meaning of the Vickers hardness (or other hardness scales) is not straightforward as it depends on a complex combination of the microstructure and elastic properties of the material. Nonetheless, Vickers hardness is a useful tool for evaluating the relative strength of different materials. A convenient

approximate relation concerning Vickers hardness is  $HV \sim 3\sigma$  where  $\sigma$  is the yield strength.

For the purpose of evaluating the strength of materials used in this dissertation, a simple Vickers hardness apparatus was developed. The apparatus, machined from brass and shown in Figure 3.10 consists of a diamond cut to the Vickers indenter shape, fixed to the end of a lever arm which is properly weighted to apply 0.5 kg force to the indenter. The indenter was purchased in the correct shape from the Bruce Diamond company, Attleboro, MA. The hardness values for several materials were

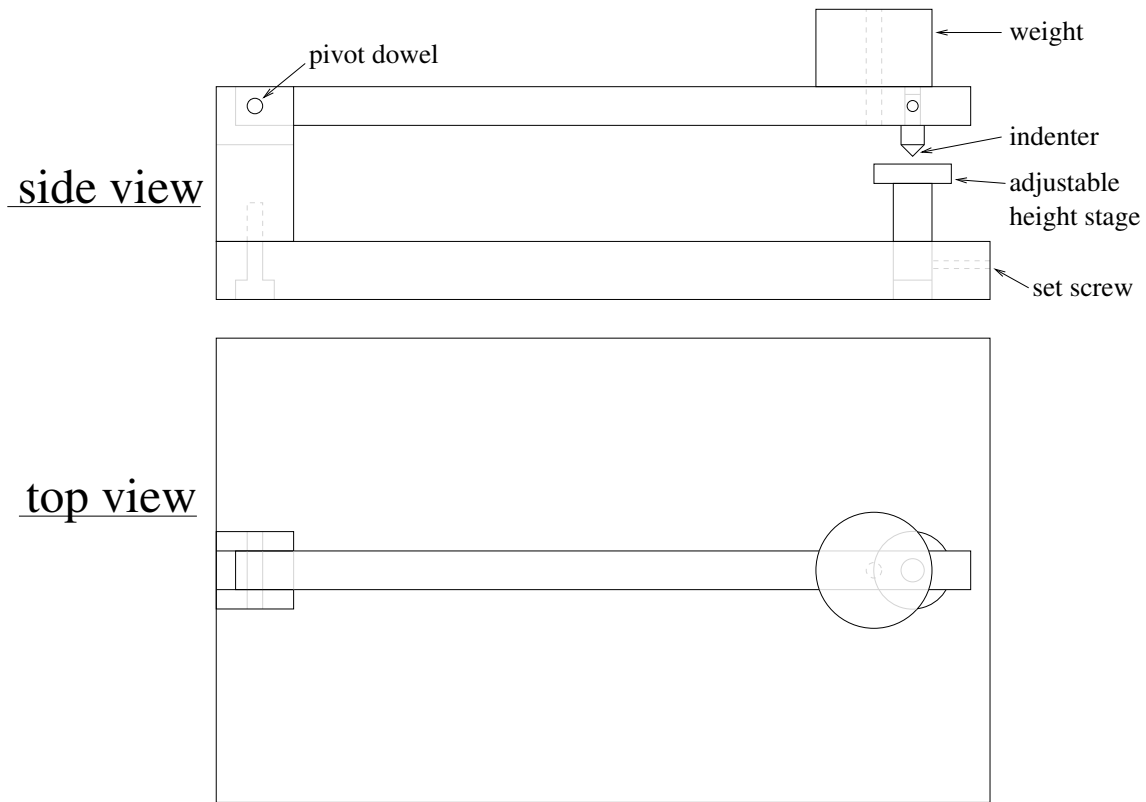


Figure 3.10: Schematic of a system for measuring Vickers hardness.

evaluated using this apparatus. The results of those measurement are summarized in Table 3.1, where the HV0.5 (Vickers hardness with 0.5 kg load) values were measured using the above described system.

Table 3.1: Vickers hardness of various materials.

material	HV0.5	HRC
Brass	95	off scale
Re (no microcracks)	553	52
Re (w/ microcracks)	304	30
W	600	55
$W_{0.75}Re_{0.25}$	579	54
SS103	450	45
Ta-W	361	37
$Re_{0.9}Os_{0.1}$	685	59
MP35N (unannealed)	445	45
MP35N (565 °C, 4.5 hrs, Argon)	595	55
MP35N (565 °C, 8 hrs, Argon)	502	49
Ni-Cr-Al (unannealed)	469	47
Ni-Cr-Al (600 °C, 7.5 hrs, air)	565	53
Ni-Cr-Al (1150 °C, 5.7 hrs, air)	183	off scale

### 3.4 Water Cooled Magnet

A signature of superconductivity is that it is suppressed by magnetic field (see Section 2.1). In ac magnetic susceptibility measurements one must have a method to test if the tiny dips in the signal are due to superconductivity rather than possible magnetic ordering phenomenon. Observation of the transition shifting to lower temperature under the application of a dc magnetic field is a strong indication of superconductivity. The diamond anvil cells used in this research are too large to fit in the bore of the lab's nine Tesla (90,000 Gauss) superconducting magnet cryostat. We decided to add the ability to apply a dc magnetic field to samples placed the continuous flow cryostat described in Section 3.2. There are two options for placing the field generating coil; inside or outside of the cryostat. A coil inside of the cryostat has the advantage of a smaller bore diameter, resulting in higher fields for lower power input. However, sample heating effects by such a coil would be significant, especially at low temperatures. Superconducting wire could be used to wind the coil but there are difficulties concerning the leads connecting to the superconducting coil. As a simple solution, we constructed a solenoid made of Cu wire wound on a brass spool form that fits outside of the cryostat (Figure 3.11). In order to avoid excessive heating in the sensitive region surrounding the cryostat, the coil employs water cool-

ing. A water volume separates the coil from the cryostat. During operation, cold tap water is continuously cycled through the coil spool. The coil was wound with 1.32 mm diameter insulated copper wire in 14 layers with an average of 58 turns per layer. The field produced by the coil was measured using a calibrated Hall probe and found to be 59.8(8) Oe per Amp. The field was also calculated and found to be 63.2 Oe per Amp. The field from the Hall probe measurement is used for values reported in this dissertation.

The coil is powered using a Kepco brand ATE-55-20DM constant current power supply capable of operating up to 55 Volts and 20 Amps. Figure 3.12 shows the average temperature of the coil windings versus the input power. Power was determined

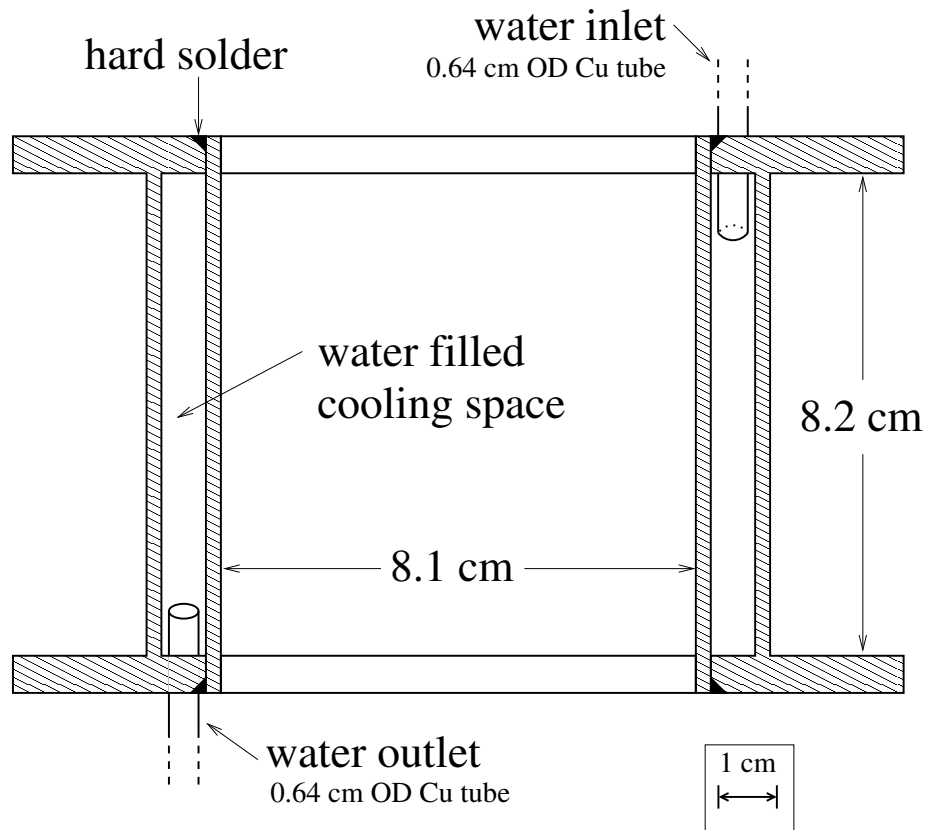


Figure 3.11: Cross sectional plan of water cooled magnet spool. Spool is machined from brass.

from the product of the input current and voltage. Temperature of the coil in degrees

Celsius is given by

$$T = T_0 + \frac{1}{\alpha} \left( \frac{R}{R_0} - 1 \right),$$

where  $R = V/I$  is the resistance at the corresponding temperature,  $R_0 = 4.5\Omega$  is the room temperature resistance of the coil,  $T_0 = 22\text{ }^\circ\text{C}$  is room temperature and  $\alpha = 0.0039\text{ }^\circ\text{C}^{-1}$  is the temperature coefficient of resistivity for copper. For safety reasons, the coil should be operated below  $100\text{ }^\circ\text{C}$  (boiling point of the water coolant). The coil reaches  $100\text{ }^\circ\text{C}$  at 450 Watts, corresponding to a field of approximately 550 Oe for the present windings. The power supply reaches its voltage limit of 55 Volts close to the same operating condition of 450 Watts and 550 Oe. Increasing the cooling power appears to be the only way to increase the maximum achievable field using the present coil spool; a more detailed analysis has shown that the maximum achievable field does not depend strongly on the diameter of the copper wire used to wind the coil.

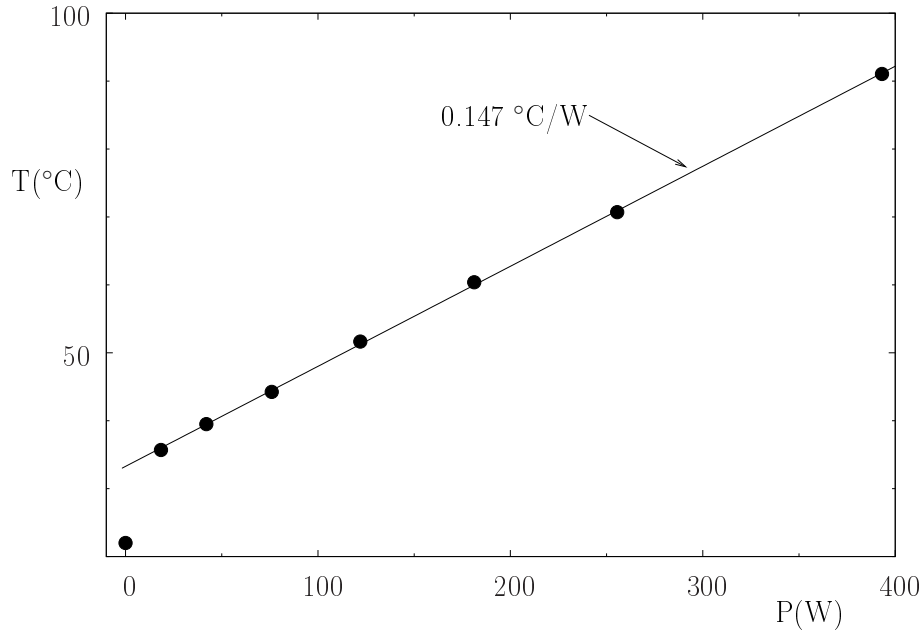


Figure 3.12: Temperature versus power for the water cooled magnet.

## 3.5 Optical Measurements in the Diamond Anvil Cell

The various types of optical measurements performed during my dissertation work are described in the following sections (Sections 3.5.1-3.5.4). Appendix B contains a complete overview the optical system that was used for most of these measurements.

### 3.5.1 Ruby Fluorescence Manometer

A survey of the history of high pressure research reveals that much early effort was devoted to the development of practical and accurate methods for measuring the applied pressure [28]. After the invention of the diamond anvil cell in 1959, [29] accurate pressure determination in the small sample volume of the diamond anvil cell was problematic; many traditional manometers could not be adapted to the diamond anvil cell and calculations could only provide very rough estimates of the applied pressure. For over a decade, the lack of an accurate manometer prevented the widespread adoption of the diamond anvil cell as an experimental tool. After studying the pressure dependence of the fluorescence spectrum of many materials, scientists working at the National Bureau of Standards discovered, in 1972, that the fluorescence spectrum of ruby ( $\text{Al}_2\text{O}_3$  doped with  $\text{Cr}^{3+}$ ) exhibits exceptionally strong, sharp peaks that display a large, linear red-shift under pressure [30]. The high intensity of the ruby fluorescence meant that small ruby chips on the order of one percent of the total sample space volume could provide a rapid and precise means of determining pressure in the diamond anvil cell. The years following the development of the ruby fluorescence manometer saw a rapid increase in the number of laboratories employing diamond anvil cells. In the 13 years after the invention of the diamond anvil cell and before the development of the ruby fluorescence manometer, only  $\sim 10$  papers relating to the phrase “diamond anvil cell” were published. In the 5 years immediately following the calibration of the ruby high pressure scale, at least  $\sim 60$  papers were published concerning “diamond anvil cells” (see Figure 3.1).

## Fluorescence Mechanism

Fluorescence is a phenomena in which the absorption of a photon by a material leads to the emission of a photon with lower energy. First, the material is “pumped” into an excited state by illumination in one of the absorption bands of the material. This excited state rapidly decays into a meta-stable state by a so-called fast, non-radiative decay (usually via emission of a phonon). Finally, the decay from the meta-stable state to the ground state results in the emission of a photon.

Transition to ground state		Energy (cm <sup>-1</sup> )
Y		25200
		24400
U		18450
		18000
R <sub>2</sub>		14430
R <sub>1</sub>		14400

Figure 3.13: Energy levels associated with ruby fluorescence. Figure adapted from Reference [91].

A simplified representation of the energy levels associated with ruby fluorescence (at ambient pressure) is shown in Figure 3.13. There are two primary absorption bands, denoted Y and U. Ruby can be efficiently pumped into an excited state by illumination with blue (Y band) or green (U band) light. Following pumping into the Y or U band, there is a fast non-radiative decay into one of two meta-stable states denoted R<sub>1</sub> and R<sub>2</sub>. The decay from R<sub>1</sub> and R<sub>2</sub> to the ground state results in the characteristic fluorescence spectrum of ruby, used in many of the experiments of this dissertation as a manometer. Under pressure, the R<sub>1</sub> and R<sub>2</sub> levels shift to lower

energy and thus the fluorescence lines become red-shifted with pressure. For reasons discussed below, the shift in the R<sub>1</sub> line is used to determine pressure.

### Temperature Dependence of Ruby Fluorescence

At room temperature, the populations of the R<sub>1</sub> and R<sub>2</sub> states nearly equilibrate due to thermal energy and thus the intensity of the R<sub>1</sub> and R<sub>2</sub> lines are roughly the same. As temperature is decreased, the population of the R<sub>2</sub> state (higher energy) becomes small compared to that of the R<sub>1</sub> state (lower energy). Thus at low temperature, the R<sub>2</sub> fluorescence line is suppressed. This results in a somewhat greater intensity of the R<sub>1</sub> line at low temperature. Also, the locations of the R<sub>1</sub> and R<sub>2</sub> lines are weakly temperature dependent. The temperature dependence of the R<sub>1</sub> line was found by Buchsbaum *et al.* [92] to be given by

$$\nu_0(t) = 14422.0 - 36.612t^{3/2} + 169.77t^2 - 265.54t^{5/2} + 112.14t^3, \quad (3.2)$$

where  $\nu_0(t)$  is given in  $\text{cm}^{-1}$ ,  $t = T/(300\text{K})$  and the temperature  $T$  is in Kelvin. Figure 3.14 shows the temperature dependence of the R<sub>1</sub> line plotted as wavelength versus temperature. Fortunately the temperature and pressure dependences of these lines appear to be independent, easing the calculation of pressure for a given wavelength shift at a given temperature [93, 94].

### Pressure Dependence of Ruby Fluorescence

Since the development of the ruby fluorescence manometer, a number of different calibrations of the fluorescence wavelength versus pressure have been used as standards. Piermarini *et al.* [30, 95] calibrated ruby versus the equation of state of NaCl up to 19.5 GPa in a 4:1 methanol:ethanol mixture; this calibration will hereafter be referred to as PBBF75 after the authors and year of publication. In 1978, Mao *et al.* [96] calibrated ruby versus the equation of state of several metals using no pressure medium (ruby directly pressed between diamond and gasket) up to 100 GPa; this calibration will be referred to as MBSS78. Mao *et al.* calibrated ruby versus the equation of state of copper up to 80 GPa in argon pressure medium [97] and later confirmed

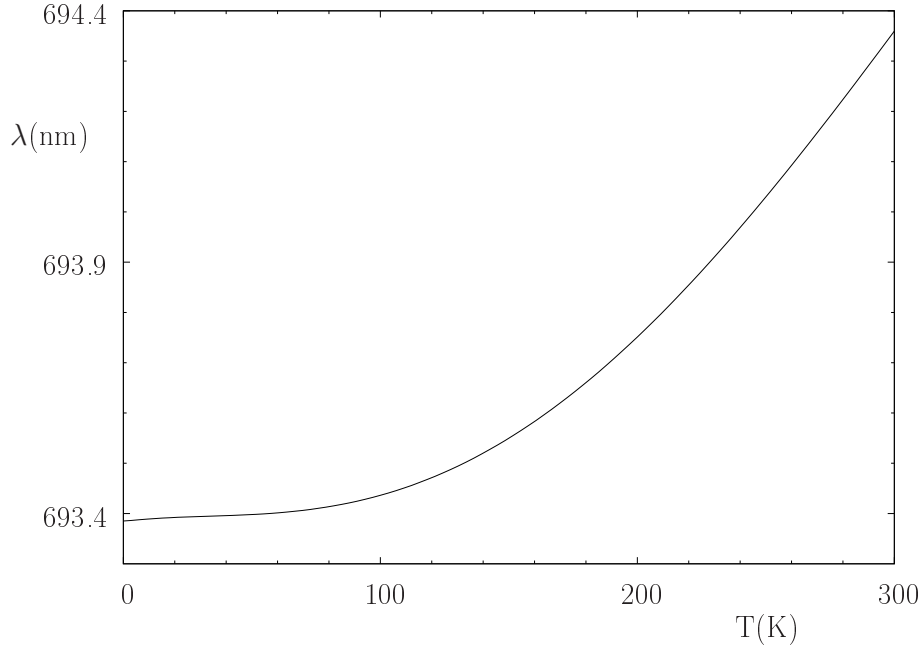


Figure 3.14: Temperature dependence of the  $R_1$  ruby fluorescence line at ambient pressure as given by Reference [92].

the calibration to 110 GPa versus the equation of state of tungsten in neon pressure medium [98]; this calibration will be referred to as MXB86. For years, MXB86 has been the most frequently used standard. Very recently, evidence has accumulated that the earlier ruby pressure scales systematically underestimated pressure in the upper pressure range and new calibrations have been suggested [36, 99–101]. At this time the most comprehensive and accurate pressure calibration appears to be that of Chijioke *et al.* [100], which takes into account the results of many hydrostatic calibrations and is referred to here as CNSS05. Pressure versus the wavelength of the  $R_1$  line,  $\lambda$  is given by the CNSS05 calibration as

$$P(\text{GPa}) = \frac{1876}{10.71} \cdot [(\lambda/\lambda_0)^{10.71} - 1], \quad (3.3)$$

where  $\lambda_0$  is the wavelength of the  $R_1$  line at ambient pressure.

Figure 3.15 (a) shows the pressure versus wavelength shift for each of the calibrations discussed above and Figure 3.15 (b) shows the differences between the various scales relative to the commonly used MXB86 scale; this plot can be used as a conve-

nient means for correcting older measurements the new, more accurate CNSS05 ruby scale.

### **Effect of non-Hydrostatic Pressure on Ruby Fluorescence**

Under non-hydrostatic pressure the ruby line becomes broadens and the  $R_1$  to  $R_2$  separation increases. Figure 3.16 shows examples of the ruby  $R_1$  line under conditions varying from nearly strain free to highly strained (non-hydrostatic). This line broadening effect can be used to estimate the magnitude of non-hydrostatic pressure components within the cell from the full width at half maximum (FWHM) of the  $R_1$  line [102]. It has been suggested that the separation between the  $R_1$  and  $R_2$  lines is mainly determined by shear stresses while the width of the ruby lines is determined by pressure inhomogeneities (gradients) within the cell [103]. In experiments with no pressure medium (such as the resistivity measurements described in Section 3.7) the pressure gradients appear to increase linearly and reversible with pressure. Figure 3.17 shows the FWHM of the  $R_1$  line versus pressure during one of the resistivity measurements described in Section 4.2.2. At the highest pressure, the FWHM of the ruby line corresponds to a range of pressures from 68 to 97 GPa.

### **Ruby Manometer above One Megabar**

Above one megabar, several effects make measurement of the ruby lines difficult. To reach one megabar, diamonds with small culets must be used, limiting the amount of ruby that can be placed in the sample cell (the fluorescence intensity is proportional to the volume of ruby). The increasing width of the ruby line at high pressures makes it difficult to resolve.

At pressures above  $\sim 120$  GPa the diamond itself begins to fluoresce, giving rise to a broad sloping background with increased intensity at shorter wavelengths (see Figure 3.16). The superposition of the ruby line on top of this sloping background can create a falsification in the peak location; to eliminate this falsification, a linear background was subtracted in the vicinity of the peak before determining the location of the peak. Eventually the diamond fluorescence completely obscures the ruby fluorescence peak. The fluorescence lifetime of the ruby increases monotonically with

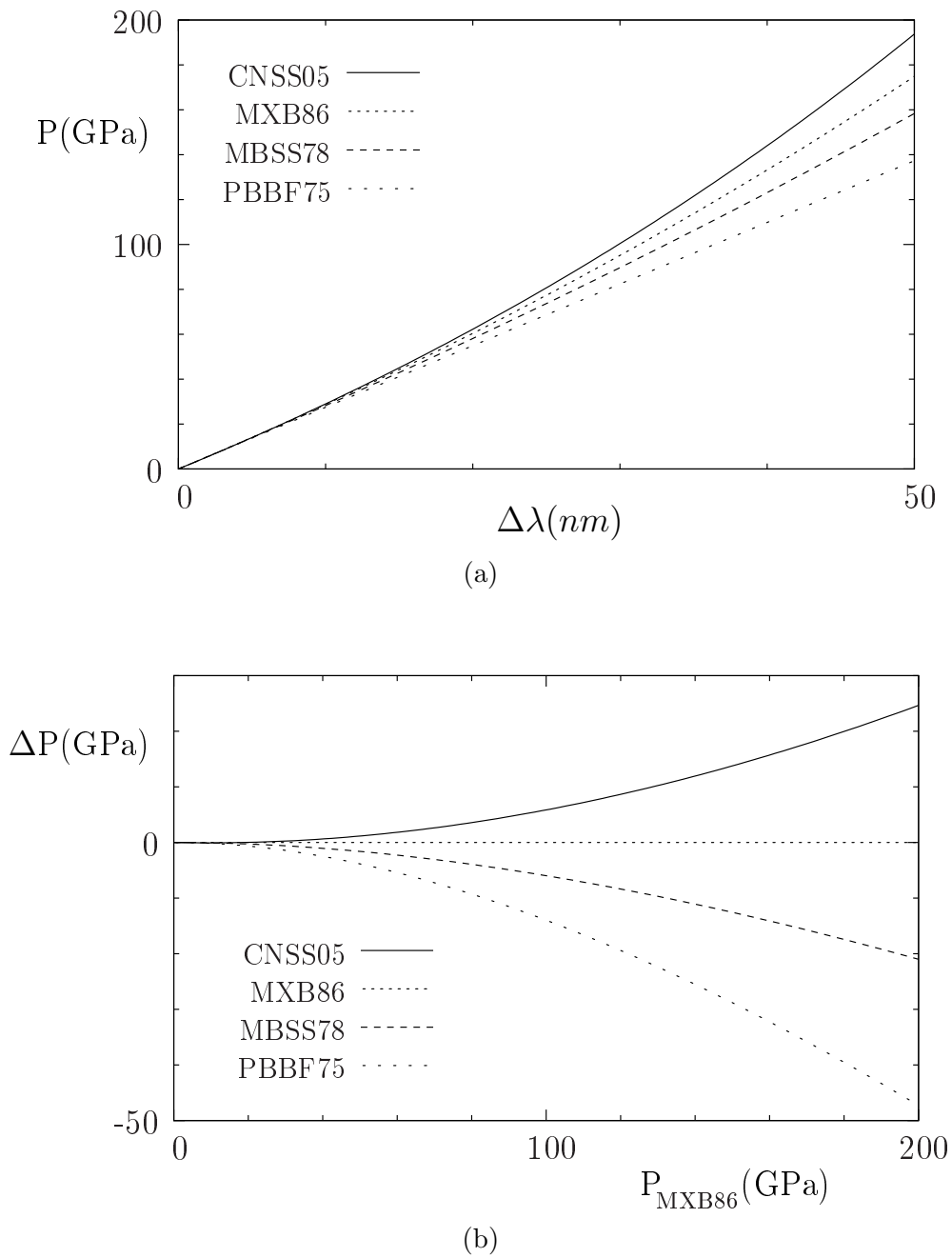


Figure 3.15: Comparison of different ruby manometer calibrations. (a) Pressure dependence of R1 ruby fluorescence peak shift according to the calibrations discussed in the text. (b) Difference between the popular MXB86 scale and the other ruby manometer calibrations.

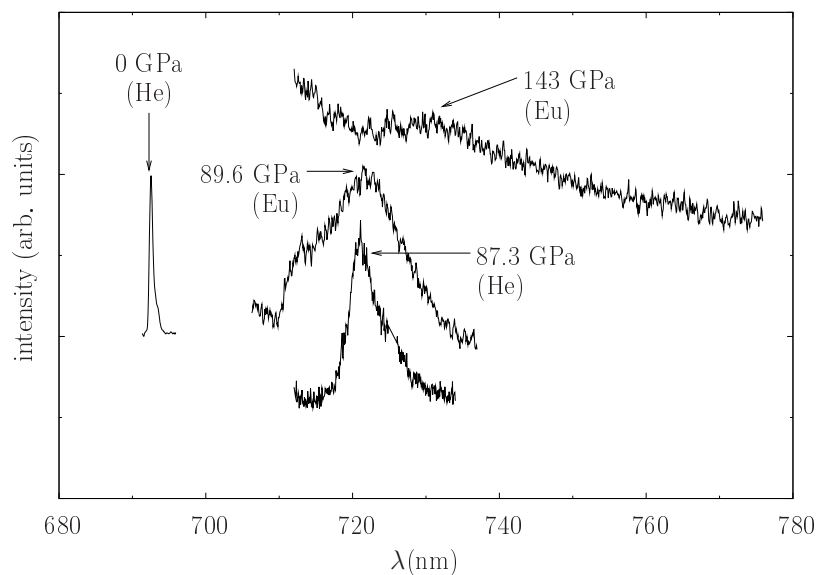


Figure 3.16: Ruby measurements taken at various pressures. The intensities of the high pressure measurements have been scaled up by 550 percent relative to the ambient pressure measurement. Note the appearance of a strong background at 143 GPa due to the fluorescence of the diamond. All measurements were taken at low temperature so the  $R_2$  line is suppressed.

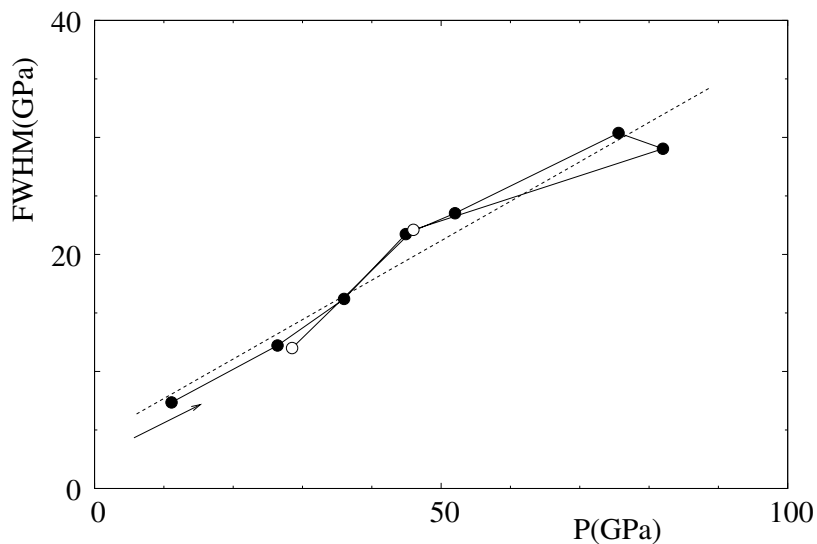


Figure 3.17: FWHM versus pressure of the ruby  $R_1$  line in a resistivity measurement without pressure medium. Filled and open circles show points taken on loading and unloading, respectively.

pressure from 3 ms at ambient pressure to 25 ms at 1.3 Mbar [70] whereas the lifetime of the diamond fluorescence is on the order of a few ns. This fact allowed Silvera *et al.* [104] to develop a method utilizing optical choppers to eliminate the diamond fluorescence from the measured spectrum.

The U and Y bands shift to higher energy, so that above  $\sim 70$  GPa the 514 nm line of the Ar<sup>+</sup> laser is too low in energy to efficiently pump the ruby fluorescence. Likewise, above one megabar, pumping with the 441.6 nm line of the He-Cd laser begins to become very inefficient leading to a rapid drop in the intensity of the ruby fluorescence. Near 250 GPa the U and Y bands shift above the absorption edge of diamond (which shifts to lower energies with pressure) thus making it impossible to excite the ruby fluorescence by pumping these bands [105]. Silvera *et al.* [91, 106] have outlined a method to pump the ruby fluorescence at pressures up to 4-5 megabar using a tunable dye laser.

### 3.5.2 Diamond Vibron Manometer

As discussed in Section 3.5.1, above 100 GPa the R1 fluorescence line of ruby becomes weak, broad and increasingly difficult to measure. A convenient alternative to the ruby fluorescence manometer is to use the Raman spectrum of the diamond anvil itself to determine pressure.

The Raman effect was first observed by K. S. Krishnan and Sir C. V. Raman in 1928, a discovery for which Raman won the 1930 Nobel Prize in Physics. The effect occurs when photons are inelastically scattered by a material through the emission or absorption of a phonon. For backscattering geometry (photons scattered through 180 degrees) conservation of energy and momentum gives

$$nq' = nq \pm k, \quad (3.4)$$

where  $q$ ,  $q'$  and  $k$  are the wavenumbers of the incident photon, scattered photon and phonon, respectively, and  $n$  is the index of refraction of the material. The “+” sign refers to the *anti-Stokes* component (phonon absorbed) component of the scattered spectrum and the “−” sign refers to the *Stokes* (phonon emitted) component. Equation 3.4 describes the single photon process which gives rise to the *first-order* Raman

spectrum; two photon scattering gives rise to the much weaker *second-order* Raman spectrum. The key components of a modern Raman spectrometer are an excitation laser, a sensitive, high resolution spectrometer and a sharp edge or notch filter for separating the very strong Rayleigh (elastically) scattered signal from the very weak Raman scattered signal.

The first-order Raman spectrum of diamond was first studied by Ramaswamy in 1930 (for a comprehensive bibliography of early work on the Raman spectrum of diamond see Reference [107]). The spectrum consists of a single peak (referred to here as the diamond vibron) located at  $1333.1 \text{ cm}^{-1}$  at room temperature, shifting slightly to  $1333.3 \text{ cm}^{-1}$  at 15 K [108]. The pressure dependence of the diamond vibron was measured to high pressure (27 GPa) by Boppart *et al.* [109] under quasi-hydrostatic conditions and was found to shift monotonically to higher frequencies under pressure. A small chip of diamond was loaded into the cell and surrounded by hydrogen, argon or xenon pressure medium; great care had to be taken to separate the Raman spectrum of the diamond chip from that of the anvils, reducing the ease of use of this method as a monometer. Hanfland *et al.* [110] suggested that the high frequency edge of the anvil itself could be used as a convenient manometer. The pressure throughout the anvil varies from zero at the table in the optical port up to the maximum pressure at the center of the culet. Since the diamond vibron shifts monotonically to higher frequency under pressure, the high-frequency edge of the anvils Raman spectrum gives the pressure at the center of the culet where the sample is located. The most recent calibration of the high-frequency edge of the Raman spectrum of the diamond anvil is that of Akahama *et al.* [111] who performed a calibration to 310 GPa using the equation of state of platinum as a standard and found that the calibration is nearly independent of the gasket material, sample or pressure medium. They found that the pressure is given by

$$P(\text{GPa}) \cong K_0 \frac{\Delta\nu}{\nu_0} \left[ 1 + \frac{1}{2}(K'_0 - 1) \frac{\Delta\nu}{\nu_0} \right], \quad (3.5)$$

where  $\nu_0 = 1334 \text{ cm}^{-1}$ ,  $K_0 = 547(11) \text{ GPa}$  and  $K'_0 = 3.75(20)$ . Equation 3.5 is plotted in Figure 3.18.

An advantage to using the Raman vibron of the diamond anvil to determine

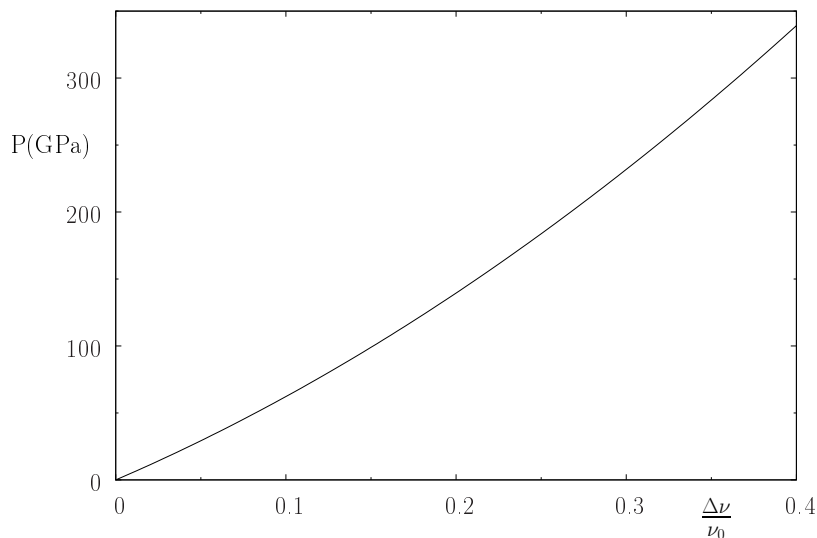


Figure 3.18: Pressure versus relative shift in high pressure edge frequency of the diamond vibron, as given by Reference [111].

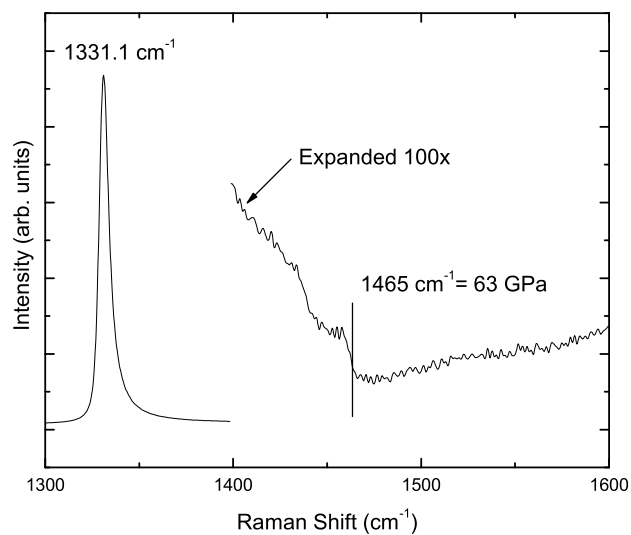
pressure is that one does not have to include a pressure calibrant inside the cell. This may be particularly useful in the case of optical absorption measurements where having ruby within the cell may falsify the results since some of the light will pass through the ruby pieces instead of the sample. In addition, the diamond vibron manometer is useful in the case of studies (such as resistivity) which often use no pressure medium; in this situation large pressure differences may exist between the sample and ruby if they are not directly on top of each other (often the case). With the diamond vibron of the anvil, one can always measure the pressure at the same lateral location as the sample.

With the assistance of B. Wopenka, we tested this method of determining the pressure in two separate experiments using the Raman spectroscopy apparatus (a Kaiser Optical Systems multi-channel Hololab employing the 532 nm line of an Ar<sup>+</sup> laser) in the Department of Earth and Planetary Sciences, Washington University. The apparatus uses a confocal microscope to allow sampling of the Raman spectrum from areas as small as a few microns, depending on the objective used. The microscope has a variety of objectives from 5× to 80×. We attempted to measure pressure using the Raman line of the diamond anvil in a cell for which pressure was measured at 75 GPa using the ruby fluorescence manometer. The Boehler type cell (see page 30)

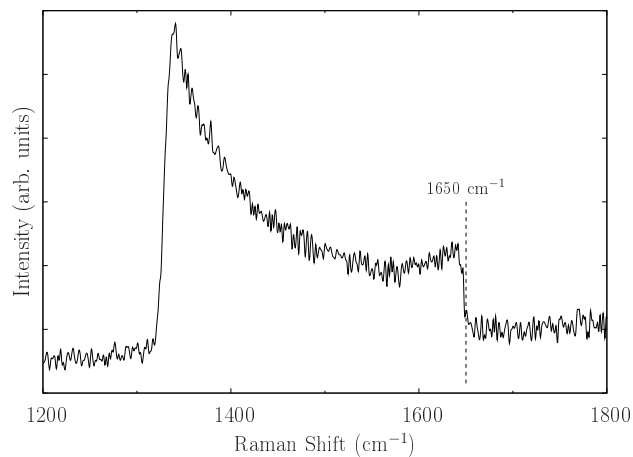
was used for this test. The cell used diamonds 0.3 mm diameter culets, a Re gasket and was loaded with ruby chips and a sample of  $\text{LiAlH}_4$ . Figure 3.19 (a) shows the measured Raman spectrum. The high frequency edge of the diamond vibron line appears at  $1465 \text{ cm}^{-1}$ ; using Equation 3.5 this gives a pressure of 63 GPa compared to 75 GPa measured with the ruby. The discrepancy was probably due to the fact that only the  $5\times$  objective had a working distance long enough to reach to the diamond culets, so the sampled area must have been large, obscuring the signal from the small section of the diamond at the highest pressure.

In a second experiment we measured the Raman spectrum of the diamond tip at much higher pressures, when the ruby fluorescence signal had become too small to detect. The diamonds were beveled from 350 to  $180 \mu\text{m}$  and the sample was Lu (additional details of this experiment are given in Section 4.1.1). For this test we used our laboratory's  $40\times$ , long working-distance (21.1 mm) objective. Despite the fact that our objective has a 210 mm tube length and the Raman microscope is designed for infinity-corrected objectives, we observed no degradation in the image quality. Figure 3.19 (b) shows the Raman spectrum from this experiment. The intensity drops to zero near  $1650 \text{ cm}^{-1}$  indicating a pressure of 174 GPa. Notice that the ambient pressure peak near  $1334 \text{ cm}^{-1}$  is significantly suppressed due to the small area sampled with the high magnification objective.

It would be very useful to be able to use the diamond vibron manometer to determine the pressure on cells inside of the group's Oxford cryostat. To this end, some preliminary design was carried out to adapt the ruby fluorescence system to measure Raman spectra. Fortunately the modifications to accomplish this are relatively minor. We purchased an edge filter designed to filter out the intense elastically scattered laser light from the weak Raman signal. The filter is designed to be used with the 441.6 nm line of the He-Cd laser. This filter should replace filter F2 in Figure B.1 to perform Raman measurements. It appears that the photomultiplier tube connected to the monochromator is not sensitive enough to accurately measure Raman signals. To this end, we have purchased a Hamamatsu HC236 two stage cooled CCD system which is known to be capable of measuring Raman signals. Finally, placing a lens inside the cryostat and drilling a larger hole into the backing material would offer



(a)



(b)

Figure 3.19: Raman spectra of diamond anvils under pressure. (a) Spectrum measured using 5 $\times$  objective. The high energy edge of the diamond vibron gives a pressure of 63 GPa while the ruby fluorescence measurement gives 75 GPa. (b) Spectrum measured using 40 $\times$  objective. High energy edge of the diamond vibron at 1650 cm<sup>-1</sup> corresponds to a pressure of 174 GPa.

significantly improved sensitivity as discussed at the end of Appendix B. The resolution of the present spectrometer should be sufficient for determining the pressure to within better than  $\pm 5$  GPa using the diamond vibron manometer.

### 3.5.3 Optical Absorption Measurements

Optical absorption measurements can be performed in our laboratory over the limited range of 20,000 to 12,500  $\text{cm}^{-1}$  (2.48 to 1.55 eV or 500 to 800 nm). These measurements can be performed within the cryostat (see Appendix B) or using the metallographic microscope (see Appendix C). In order to cover a larger spectral range we performed measurements at the department of Earth and Planetary Sciences, Washington University in the laboratory of A. M. Hofmeister, which is equipped with a Bomem DA3.02 Fourier transform infrared spectrometer (FTIR) capable of spectral measurements over the entire range from 200 to 20,000  $\text{cm}^{-1}$  (0.0248 to 2.48 eV and 50,000 to 500 nm).

An FTIR is essentially a Michelson interferometer (see Figure 3.20). Light from the source is split into two separate beams by a partially reflective beam splitter; the two beams are then recombined after traversing two different paths. By moving mirror in one of the beam paths, the length difference between the two paths and thus the interference between the two beams can be altered. Each wavelength of light produces an intensity at the detector that varies sinusoidally with the mirror position; the frequency of these oscillations is inversely proportional to the wavelength of light. The sum of all the sinusoidal oscillations adds up to what is known as an interferogram (intensity versus mirror position). The Fourier transform of the interferogram gives the spectrum of light (intensity versus wavelength). A more detailed introduction to FTIR spectrometry is given in Reference [112].

The fraction of light transmitted through a sample is given by  $T = I_{trans}/I_0$  where  $I_{trans}$  is the intensity of light transmitted through the sample and  $I_0$  is the intensity of the light transmitted through the empty cell.  $T$ ,  $I_{trans}$  and  $I_0$  are all functions of wavelength. Figure 3.21 shows an example of spectra taken with the Bomem FTIR spectrometer.

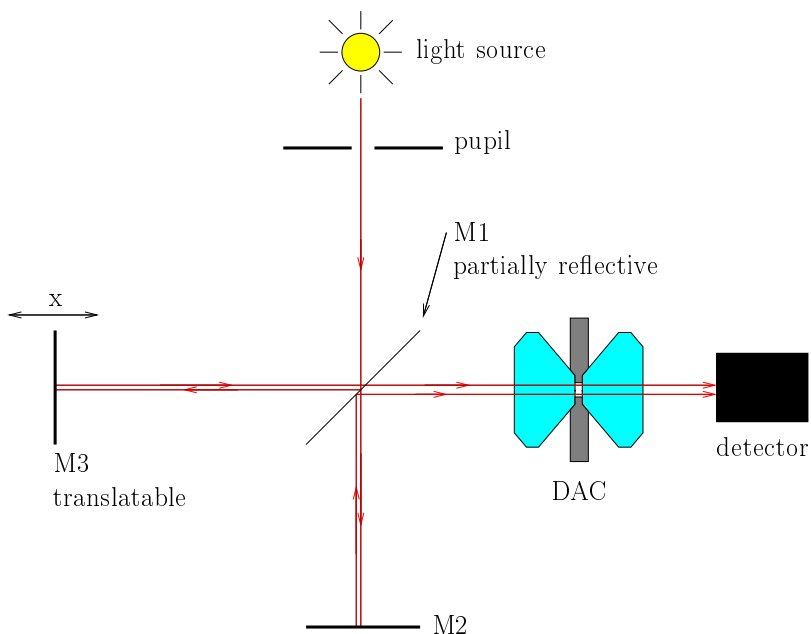


Figure 3.20: Schematic of a Fourier Transform Infrared Spectrometer (FTIR).

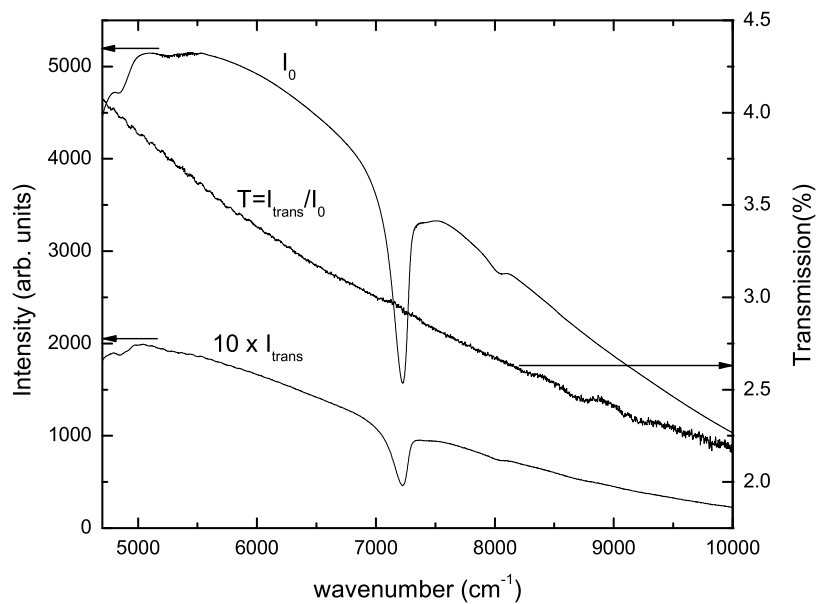


Figure 3.21: Example of extracting the fraction of light transmitted by a sample as a function of wavelength. Here,  $I_0$ , and  $I_{trans}$  are the measured intensity for an empty cell and a cell loaded with  $\text{LiAlH}_4$ , respectively. The  $I_{trans}$  curve has been expanded by a factor of 10 for clarity.

### 3.5.4 Measuring Gasket Thickness

In many experiments, it is important to know the thickness of the gasket under pressure. In experiments utilizing a hydrostatic pressure medium, it is vital to know that the diamond anvils do not press directly against the sample, ruining the hydrostaticity of the sample environment. By determining the sample thickness at the start of the experiment and measuring the gasket thickness at high pressure, it is possible to determine whether the separation between the diamond anvils remains greater than the sample thickness throughout the experiment.

Mechanical means may be used to measure the thickness of the gasket under pressure, but these methods are usually not particularly accurate because it is difficult to separate the compression of the gasket from the deformation that occurs in the other parts of the high pressure clamp. The most accurate methods for measuring gasket thickness under pressure are optical. The optics required for this type of measurement are already provided by the ruby fluorescence measurement apparatus.

There are two primary means of optically measuring gasket thickness under pressure [89, 113]. The first involves the measurement of interference rings produced between the anvils when illuminated with monochromatic light. This method has the disadvantage that rather high resolution microscopes are required in order to resolve the interference rings. The resolving power of the microscope used for viewing the sample in experiments within the cryostat was not high enough to allow the use of this method. The second method involves observing the interference spectra produced by white light illumination of the hole in the gasket.

The diamond culets form a *Fabry-Pérot interferometer*, two parallel partially reflecting surfaces separated by a gap. The transmission spectrum of a Fabry-Pérot interferometer displays peaks at certain wavelengths where there is constructive interference between different light paths. Consider the two light paths shown in Figure 3.22.

When the wavelength is equal to  $2nd$  (where  $d$  is the distance between the surface and  $n$  is the index of refraction between the surfaces) there will be constructive interference between the two light paths and the transmission spectrum will display a maximum at this wavelength. The separation between two adjacent maxima in the

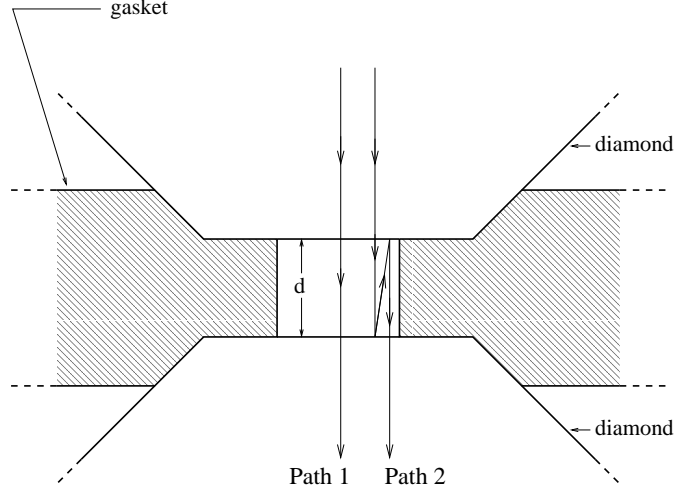


Figure 3.22: First and second order reflections illustrated by light Paths 1 and 2 give rise to a Fabry-Pérot interference spectrum.

transmission spectra is known as the *free spectral range* (FSR) and is related to the distance,  $d$  between the reflecting surfaces by

$$\Delta\lambda = \frac{\lambda^2}{2nd}, \quad (3.6)$$

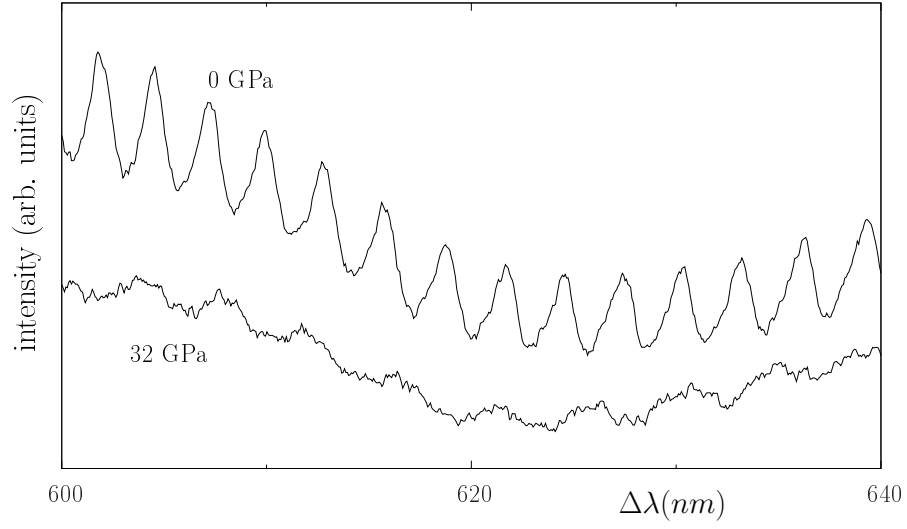
where  $\lambda$  is the approximate wavelength. From Equation 3.6 it is clear that a measurement of the FSR actually gives the product,  $nd$ , of the distance between the culets and the index of refraction of the pressure medium. There are two possibilities for isolating the thickness from this equation. One can measure the interference spectra produced by white light passing through the cell at different angles, providing independent measurements of both the separation of the anvils and the index of refraction of the material in the cell. This method has been used fruitfully by many researchers to determine the index of refraction of various materials under pressure (see Section 2.4.2 for a discussion how the pressure dependence of the index of refraction is related to the metallization of insulators). The second method for separating  $n$  and  $d$  is to use an independent measurement of the pressure dependence of  $n$ .

The experimental arrangement for capturing Fabry-Pérot interference is illustrated by Figure B.1. White light is coupled into optical fiber OF1 and the light transmitted through the cell is coupled into the spectrometer. Mirror M3 must be removed and an

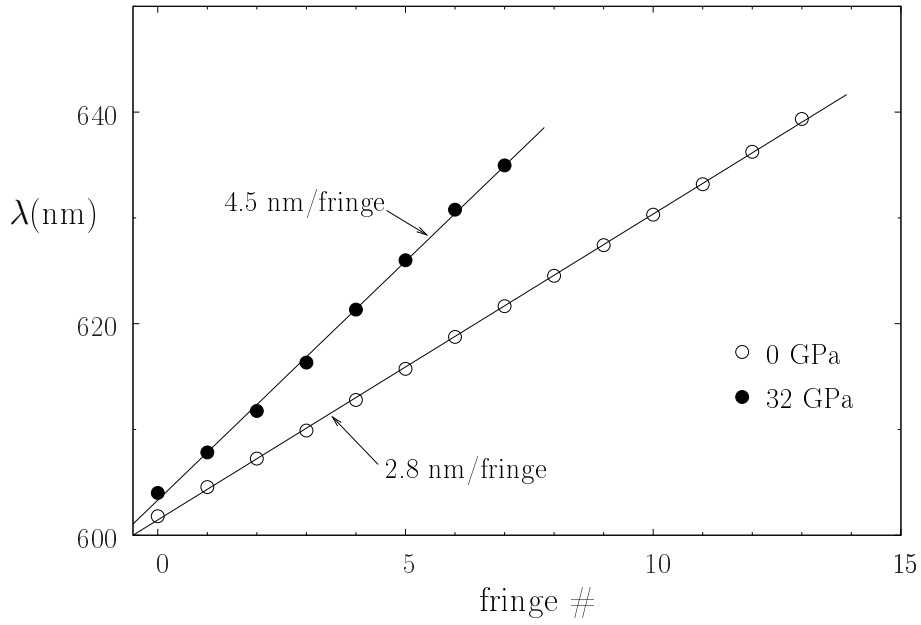
additional pupil of  $\lesssim 3$  mm diameter must be placed between lenses L2 and L3 in order to insure that only light passing perpendicularly through the cell is captured. If fringes passing through the cell at many angles are allowed to enter the spectrometer, the interference pattern is washed out. The interference spectra are measured close to 600 nm because this is where the system provides peak sensitivity. Spectra are collected over a wide enough range to collect 5-10 maxima. The wavelength range measured is determined using the calibrated dials of the monochromator which are accurate to approximately 0.5 nm, accurate enough to determine the thickness of the gasket to within 1  $\mu\text{m}$  given a precise knowledge of the index of refraction. Figure 3.23 (a) shows typical interference spectra captured at ambient pressure and high pressure (32 GPa) during an experiment utilizing He pressure medium. At higher pressure, the fringe contrast is reduced due to cupping of diamonds [113]; this makes it difficult to measure gasket thickness using this method above about 30 GPa. The location of each peak is located visually. The spacing between the peaks is found from the linear slope of a plot of peak order versus wavelength as shown in Figure 3.23 (b); this method limits the impact of uncertainties associated with locating the peaks visually. The value of  $\lambda$  for Equation 3.6 is taken as the average of the wavelengths of the longest and shortest wavelength peaks in the measured range. The index of refraction of helium under pressure was measured up to 20 GPa by Dewaele *et al.* [113] who found that the index is given by

$$n = \begin{cases} 0.8034 + 0.20256(1 + P)^{0.12763} & \text{if } P(\text{kbar}) < 116 \\ -1.033 + (1 + P)^{0.052} & \text{if } 116 < P(\text{kbar}) < 202 \end{cases} \quad (3.7)$$

The accuracy of the above described method was checked by comparing the thickness of gaskets measured mechanically with micrometer to the thickness measured at ambient pressure using the Fabry-Pérot interference spectra. In all cases the two values agreed to within 1  $\mu\text{m}$  (the accuracy of the micrometer). Figure 3.24 shows an example of thickness versus pressure as determined using white light interference spectra.



(a)



(b)

Figure 3.23: Spectral measurements used to determine the separation between the diamond culets. (a) Transmitted intensity versus wavelength at ambient pressure and 32 GPa. At 32 GPa the fringe contrast has been reduced to the limit of detection. (b) Spacing between fringes as given by a linear fit of wavelength versus fringe order.

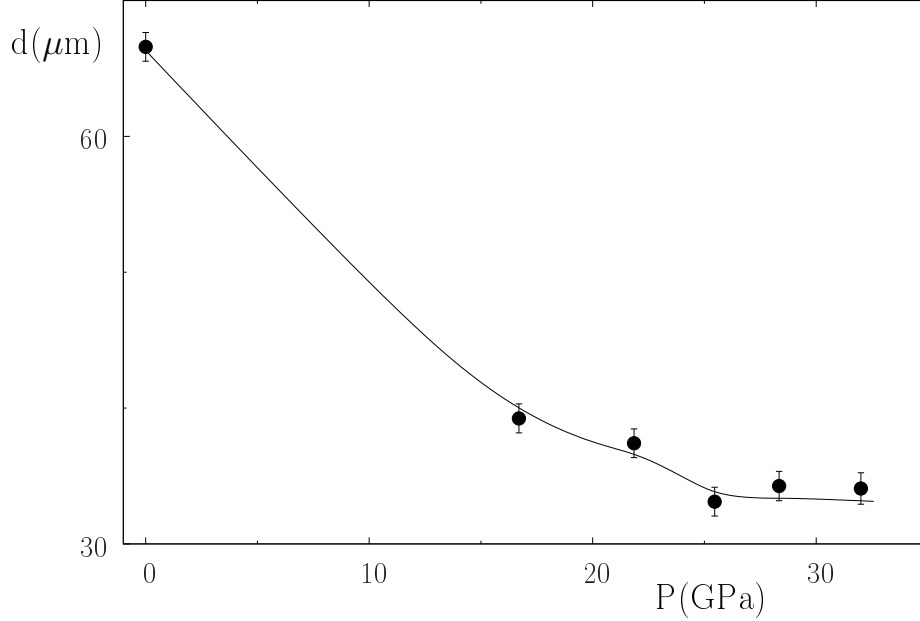


Figure 3.24: Example curve of thickness versus pressure, as determined by Fabry-Pérot interference spectra, for an experiment utilizing diamonds with 0.5 mm culets, He pressure medium, and a Re gasket initially pre-indented to 67  $\mu\text{m}$ . The solid line is a guide to the eye.

### 3.6 Coil System and AC Magnetic Susceptibility

The basic principle of the ac magnetic susceptibility measurement is shown in at the left of Figure 3.25. The sample is surrounded by a pickup coil and a separate coil subjects the sample to an alternating magnetic field. The alternating flux through the pickup coil produces an ac voltage which is the measured signal. Above  $T_c$ , the applied field penetrates the sample. When the sample is cooled below  $T_c$ , the field is expelled from the sample due to the superconducting shielding effect, forcing some of the flux lines out of the pickup coil. This leads to a reduction in the induced voltage in the pickup coil. Thus, a sudden drop in the pickup coil voltage is expected when the sample becomes superconducting.

Measuring the ac magnetic susceptibility of samples contained in a diamond anvil cell presents several difficulties. Because the coils are usually placed outside of the gasket<sup>2</sup>, the sample takes up a very small portion of the coil, in contrast to the schematic

<sup>2</sup>Several groups are now using so called “designer anvils” [114], where the coil system is actually inside of the diamond, just below the culet. Such anvils are fabricated by depositing several loops on the anvil

$$H = H_0 \cos(\omega t)$$

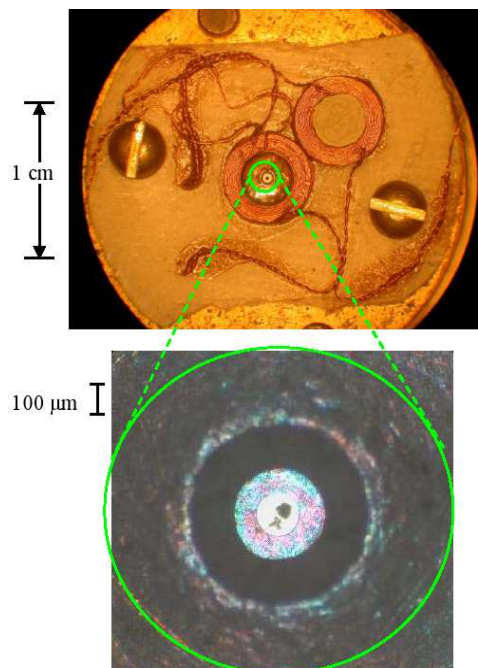
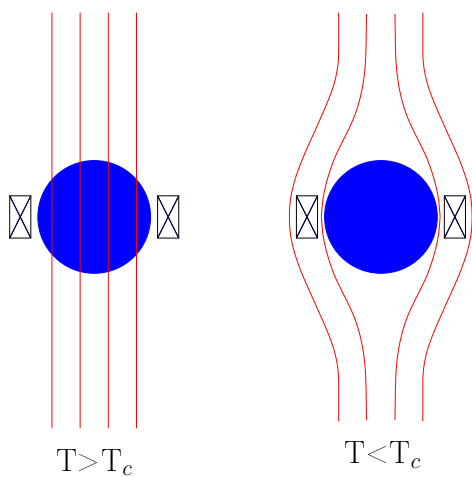


Figure 3.25: Overview of the ac magnetic susceptibility technique and coil system. (Left) Schematic illustrating the basis of the ac magnetic susceptibility technique as described in the text. (Right) Photo of actual coil system with zoomed view showing a small sample of scandium loaded into the cell with several ruby spheres.

picture shown in at the left of Figure 3.25. Therefore, the drop in the signal at the superconducting transition is a miniscule fraction of the total induced voltage. To eliminate this large background voltage, we connect the pick-up coil in series with an identically wound “dummy coil”, which is connected with opposite polarity, to cancel out the large background signal. In practice, there is a residual temperature-dependent background due to slight differences in the magnetic environments of the pick-up coil and dummy coil. In order to minimize this temperature-dependent background, one must choose a gasket material that is non-magnetic down to the lowest measurement temperatures. In addition, the gasket should have low enough conductivity that eddy currents do not significantly shield the applied field. If the gasket material becomes superconducting, clearly there is no hope of performing useful measurements on the sample.

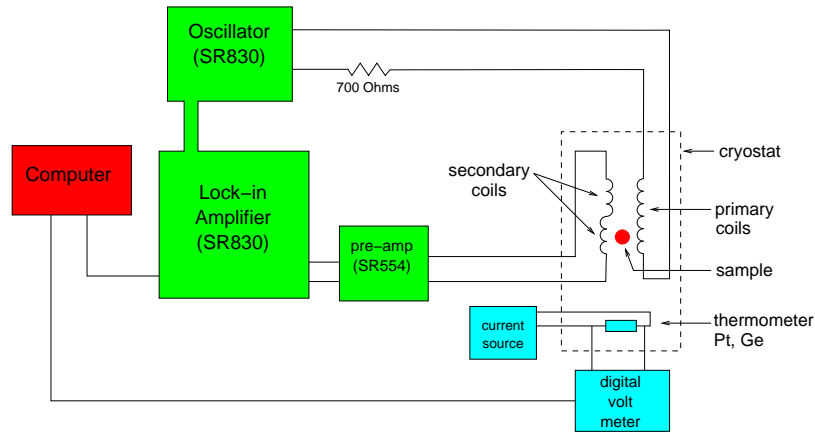


Figure 3.26: Schematic of the ac magnetic susceptibility circuit.

Figure 3.26 shows the circuit used to measure ac magnetic susceptibility. In order to allow measurements on the smallest possible samples, we enhance the signal-to-noise ratio by using a lock-in amplifier to measure the induced voltage. Functionally, the lock-in amplifier acts as a phase sensitive ac voltmeter coupled to a very narrow bandpass filter that rejects nearly all of the noise from frequencies other than the measurement frequency. A pre-amplifier connected to the circuit just outside of the cryostat provides  $100\times$  amplification to minimize the effect of noise pick-up surface and then growing a layer of diamond over the leads. Finally, the diamond is re-polished into the correct shape. The coils are much closer to the sample but have only a few turns.

in the cabling going from the cryostat to the lock-in. One could further reduce the noise by placing a preamplifier inside the cryostat, as close as possible to the coil system. We have not attempted to put a preamplifier inside the cryostat because temperature dependent gain could introduce significant temperature dependence in the background.

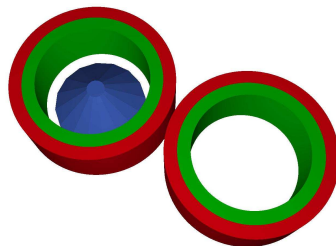


Figure 3.27: Model of the coil system. Light grey represents the secondary (pick-up) windings and dark grey represents the primary (field) windings. At left is the measurement coil (surrounding the diamond anvil) and at right is the compensation coil.

The coil system used for all of the ac magnetic susceptibility studies described in this dissertation was designed by V. G. Tissen. A photograph of the coil system is shown at the right of Figure 3.25. The system is capable of measuring superconducting transitions in samples with dimensions less than  $100 \mu\text{m}$ . Figure 3.27 shows a model of the coil system indicating the locations of the primary and secondary coils. The coils are wound from  $60 \mu\text{m}$  insulated copper wire and each consist of 6 layers with 30 turns per layer. The inner diameter of the pickup coil is 3.46 mm and the height of the coils is 1.95 mm. The field generated by each primary is calculated to be 0.432 Oe/mA. The coil is usually operated at 6.8 mA (root-mean-square), generating a field of  $\sim 3 \text{ Oe}$  ( $3 \times 10^{-4}$  Tesla).

In MKS units, the voltage induced,  $S$  in a pickup coil by a magnetic dipole is

$$S = \frac{\pi f \alpha H V N}{R(1 - D)} \chi, \quad (3.8)$$

where  $f$  is the frequency of the applied field,  $H$  is the magnitude of the applied field,  $V$  is the volume of the sample,  $N$  is the number of turns in the pickup coil,  $R$  is the radius of the pickup coil,  $D$  is the demagnetization factor, and  $\alpha \equiv 1/\sqrt{1 + (L/R)^2}$  with  $2L$  being the length of the coil. In these units,  $\chi = -1$  for a superconductor.

Although Equation 3.8 indicates that higher frequencies always lead to larger signals, the impedance matching characteristics of our lock-in amplifier and pre-amplifier eventually lead to a reduction in the signal-to-noise ratio at increasing frequency. Several tests have shown that we achieve optimal signal-to-noise when  $f \sim 1$  kHz, thus in all studies we have used  $f = 1023$  Hz. Inserting the values for the coil system described above, at 3 Oe applied field, and using convenient units, the signal for full shielding is given by

$$S(nV) = \frac{8.17 \times 10^{-5} \cdot V(\mu m^3)}{1 - D}. \quad (3.9)$$

The demagnetization factor,  $D$  depends only on the geometry of the sample. Given a field applied parallel to the axis of symmetry,  $D$  is very small for a needle shaped sample and large for a pancake shaped sample. Thus for a given volume of sample, a larger signal  $S$  will be obtained when the sample is pancake shaped (oblate). Demagnetization factors for cylinders have been calculated by Joseph [115] and those for rectangular prisms by Aharoni [116]. In hydrostatic experiments, the sample geometry can usually be well approximated by a thin, rectangular platelet, whereas non-hydrostatic experiments, the sample takes on the shape of an oblate cylinder. Typical sample dimensions in a hydrostatic experiment using 0.5 mm anvils are  $\sim 80\mu m \times 80\mu m \times 25\mu m$ , yielding  $D \sim 0.60$ . For our highest pressure, non-hydrostatic experiments, typical sample dimensions are not more than roughly  $80\mu m$  diameter by  $15\mu m$  thickness yielding  $D \sim 0.75$ . The former yields  $S \sim 33$  nV while the latter yields  $S \sim 25$  nV, according to Equation 3.9.

We now consider the effect of poor sample connectivity on the size of the transition. If the sample is broken into several pieces, shielding currents are unable to flow around the perimeter of the entire sample. This results in a reduction in the size of the drop in the signal at  $T_c$ . To obtain an approximate understanding of the effect of breaking up the sample on the transition size we imagine a sample of dimensions  $a \times a \times b$  broken up into  $N$  samples with dimensions  $(a/\sqrt{N}) \times (a/\sqrt{N}) \times b$  where  $b$  is the thickness of the sample along the c-axis (parallel to the applied field). This corresponds roughly to a picture of cracks propagating vertically through the sample along the c-axis. We further reduce all of the sample dimensions by the superconducting penetration depth  $\lambda$  so that we now have  $N$  samples with dimensions  $(a/\sqrt{N} - 2\lambda) \times (a/\sqrt{N} - 2\lambda) \times$

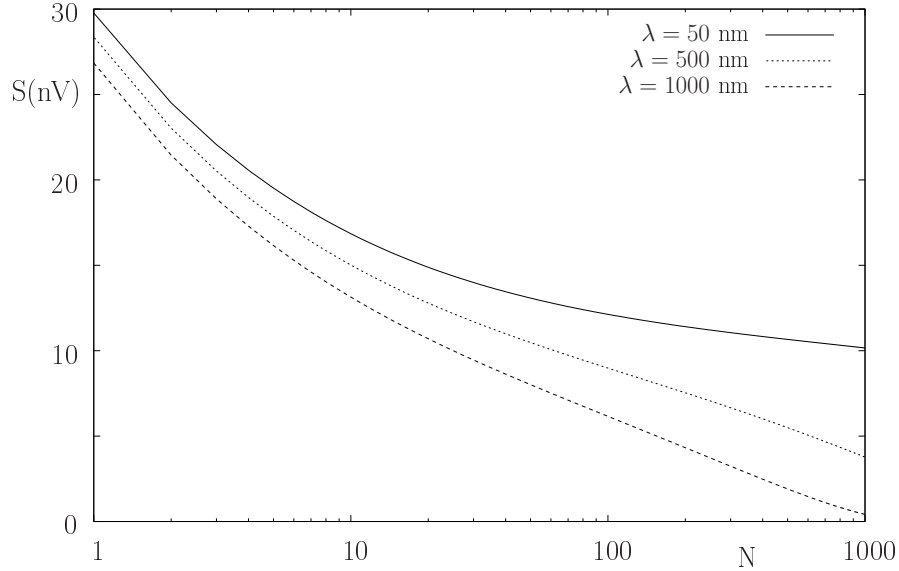


Figure 3.28: Estimated ac magnetic susceptibility signal for several values of the penetration depth  $\lambda$  and a sample of starting dimensions  $80\mu\text{m} \times 80\mu\text{m} \times 20\mu\text{m}$  broken into  $N$  pieces as described in the text. Demagnetization factors are calculated using Equation (5) from Reference [116].

$(b - 2\lambda)$ . One can then calculate  $S$  for  $N$  samples using values of  $V$  and  $D$  given by the modified sample dimensions. As an example, Figure 3.28 show the results of such a calculation for a sample with starting dimensions  $80\mu\text{m} \times 80\mu\text{m} \times 20\mu\text{m}$  and several values of  $\lambda$ . The reduction in sample size can be most problematic in materials with short coherence length  $\xi$  since polycrystalline samples of such materials can have large  $N$  if the grains are not extremely well connected.

### 3.7 Resistivity Measurements in the Diamond Anvil Cell

The technique for resistivity measurements in a diamond anvil cell was taught to our group by T. Matsuoka from Osaka University, Osaka Japan. The key difficulty in this measurement is creating an insulating layer that isolates the electrodes and sample from the gasket. The insulation between the electrodes must hold up even under extreme pressure. To accomplish this, first a metal gasket is preindented and drilled. The preindented area is then filled with an insulating mixture of diamond or alumina powder and Stycast epoxy. The powder is then pressed to a few GPa using

the diamonds. A sample chamber can be drilled into the insulating material by hand using a fine tungsten wire or acupuncture needle. Electrodes with sharp tips ( $\sim 10 \mu\text{m}$  wide) are cut, with a razor blade, from  $5 \mu\text{m}$  thick platinum foil and secured in place using a combination of tape and glue. Further details of the resistivity method are outlined in the DAC manual. The technique is inherently non-hydrostatic because the wires contacted to the sample by pressing the wires against the sample with the diamond anvil.

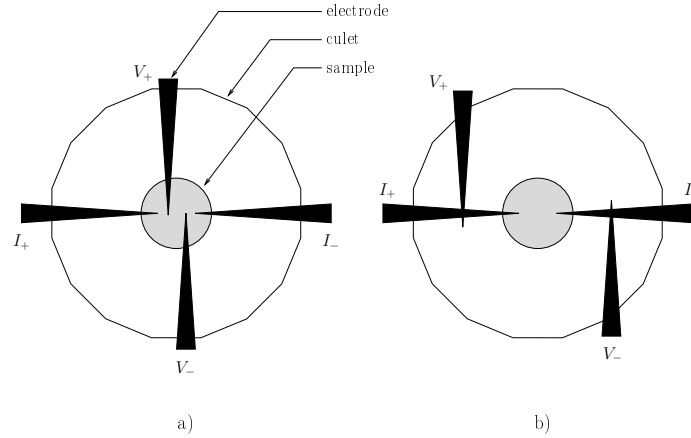


Figure 3.29: a) four-point and b) quasi four-point arrangement of leads used for measuring resistivity in a DAC.

Accurate resistivity measurements should use a four wire configuration to isolate the resistivity of the sample from the resistivity of the wires. Contacting a tiny sample on the order of  $50 \mu\text{m}$  diameter with four independent electrodes presents a challenge. Often it is only possible to achieve a “quasi-four point” configuration of electrodes in which only two electrodes contact the sample, two other electrodes are connected very close to the sample (see Figure 3.29 b)).

In order to reduce noise in the measurement and to eliminate the effect of thermovoltages, we measured ac resistivity using a lock-in amplifier. Optimizations performed by M. Debessai determined that a frequency of 13 Hz was high enough to produce a satisfactory signal-to-noise ratio and low enough to avoid parasitic voltages due to inductive coupling between the wiring and wiring environment. Figure 3.30 shows the circuit we used for measuring ac resistivity.

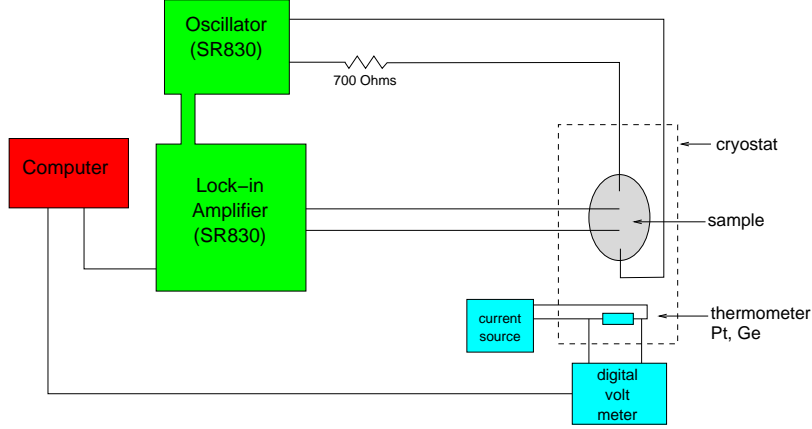


Figure 3.30: Circuit for measuring ac resistance using a lock-in amplifier.

### 3.8 General Considerations for Reaching Higher Pressures

The highest pressure reached during the course of this research was 174 GPa (Section 4.1.1), reached using diamonds beveled from 350  $\mu\text{m}$  to 180  $\mu\text{m}$  tips. There are few groups capable of reaching multi-megabar pressures and, to the author's knowledge, no groups capable of ac magnetic susceptibility measurements at multi-megabar pressures). In order to reach multi-megabar pressures, diamonds with significantly smaller tip diameters will have to be employed. V. Tissen has suggested [88] that the maximum pressure regularly attainable is related to the culet diameter by

$$P_{max}(GPa) = 12.5/d^2, \quad (3.10)$$

where  $d$  is the diameter of the diamond culet in mm. This equation suggests a maximum pressure of 50, 78 and 139 GPa for culet diameters of 0.5, 0.4 and 0.3 mm respectively. It's not clear how this empirical formula should be applied to beveled anvils but one could take  $d$  as the average of the culet and tip diameters. For diamonds beveled from 350  $\mu\text{m}$  to 180  $\mu\text{m}$  this would give  $d = 0.265$  mm, suggesting a maximum pressure of 178 GPa.

Aside from the increased difficulty of accurately aligning diamonds with smaller tips and problems measuring the ruby fluorescence above one megabar (see Section 3.5.1), there are problems associated with performing quantitative measurements

on ever smaller samples. In the case of ac magnetic susceptibility measurements, for samples of similar shape, the size of the signal is proportional to the volume (see Equation 3.8). Increased pressure gradients at megabar pressures may broaden the superconducting transition, further increasing the difficulty of extracting small sample signals from a large background. The coil system and lock-in technique described in Section 3.6 would produce a  $\sim 1$  nV signal for a sample 30  $\mu\text{m}$  diameter by 5  $\mu\text{m}$  thick, given 100% shielding. A  $\sim 1$  nV signal is at the limit of detection and we'll see in Chapter 4 that frequently we do not find 100% shielding. In order to perform ac magnetic susceptibility measurements at multi-megabar pressures, a more sensitive coil system may have to be designed. Resistivity measurements have the advantage that the size of a drop in resistance at a superconducting transition should become larger for thinner samples (for a given separation between the leads). The primary roadblock to performing resistivity measurements at higher pressures is the difficulty in manually placing four electrodes on a micron-sized sample. This could be overcome by automating the electrode fabrication by, for example, sputtering the electrodes onto the diamond using a mask.

# Chapter 4

## Results and Discussion

### 4.1 Superconductivity in d-Electron Metals

The d-electron metals are comprised of the transition metals, the lanthanides (elements 57 through 71), and the heavy actinides. In Section 2.3 we noted that the majority of ambient pressure superconductors are d-electron metals, i.e. elements with a partially filled d-shell. Considering elements up to number 98 (Californium), of the non-magnetic d-electron metals, only Sc, Y, Lu and Ac, and the noble metals Cu, Ag, and Au have not been found to be superconductors at ambient pressure. While Sc, Y and Lu have not been found to be superconducting at ambient pressure down to mK temperatures, Wittig *et al.* found all three become superconducting under sufficient pressure [117–119]. Despite theoretical predictions of high  $T_c$  values in actinium [81], this has not been confirmed in experiment, probably due to the extreme difficulty of working with this highly radioactive element. Interestingly, all four of these metals are trivalent in the solid state and share the valence electron configuration  $nd^1(n+1)s^2$  where  $n=3, 4, 5$  or  $6$  for Sc, Y, Lu and Ac respectively. Why are these metals not superconducting? Conversely, why is fcc-La, the only other trivalent metal sharing the same valence electron configuration ( $n=5$ ) a rather good superconductor at ambient pressure, with  $T_c \sim 6K$ ? Europium is divalent and magnetic at ambient pressure. At pressures as high as 40 GPa, Eu remains magnetic and non-superconducting down to 2.3 K [120, 121]. Europium is predicted to undergo a divalent to trivalent transition at pressures between 20-40 GPa [76]. Will trivalent Eu become superconducting

under pressure like the other trivalent rare earths? With these questions in mind we explored the superconducting properties of Sc, Y, Lu, and Eu to pressures as high as 1.74 Mbar, in some cases nearly an order of magnitude higher pressure than earlier studies.

#### 4.1.1 Experiment

In the course of my dissertation research, several high pressure experiments were carried out on elemental d-electron metals. All experiments used the membrane-loaded Cu-Be diamond anvil cell (see Section 3.1) and type-Ia diamond anvils. Cooling to temperatures as low as  $\sim 1.55$  K was provided by the Oxford continuous flow cryostat described in Section 3.2. A variety of culet diameters were used, depending on the maximum pressure to be reached. Gasket material selection depended on the desired maximum pressure (limited by strength of gasket) and lowest measurement temperature (limited by  $T_c$  of gasket). The thickness of the pre-indented region and diameter of the hole were kept within  $\sim 20\%$  of the values described in Section 3.1. In experiments with helium pressure medium the gaskets were sputtered with a layer of gold approximately 100 nm thick to improve sealing at the gasket-diamond interface. Pressure has been determined using either the ruby fluorescence manometer or, in one case, the diamond vibron manometer. Pressure measurement was always performed as close as possible to  $T_c$ . Ruby fluorescence pressures are determined using the calibration of Chijioke *et al.* [100] while diamond vibron pressures are determined using the calibration of Akahama *et al.* [111]. Superconducting transitions were detected using the coil system described in Section 3.6, operating at a frequency of 1023 Hz and an applied field of 3 Oe (root-mean-square) or, in a few cases, the resistivity technique described in Section 3.7. Each pressure or  $T_c$  value mentioned in the following sections represent the average of at least two consecutive measurements. DC magnetic fields up to 500 Oe were applied using the water cooled magnet described in Section 3.4.

## Yttrium

A total of four separate high pressure experiments were performed on yttrium. These experiments are referred to as runs A, B, C, and D. All runs used 1/6-carat, type-Ia diamond anvils. Run A used anvils with 0.5 mm diameter culets, runs B and C used 0.3 mm culets and run D used culets beveled from 0.35 mm to 0.18 mm (bevel angle of 7 degrees). Runs A, B and D used Re as gasket material while run C used Ni-Cr-Al (Russian alloy) heat treated to provide a Vickers hardness of  $\sim 500$  HV0.5. In runs A, B and C the sample was completely surrounded by helium pressure medium, providing the most hydrostatic pressure environment possible. In run D, no pressure medium was utilized and the sample completely filled the hole in the gasket. In runs A, B and C pressure was always changed between 150 K to 180 K and the temperature was kept below 180 K throughout the entire course of the experiment to reduce the possibility that helium diffuses into the diamonds and causes failure. In run D the pressure was always changed at room temperature. Runs A, B, C and D reached maximum pressures of 48, 89, 77 and 115 GPa, respectively. Runs B and C ended when the diamond anvils shattered on increasing the pressure. Pressure was released to ambient pressure, without anvil failure, in runs A and D.

In Figure 4.1 we show the ac susceptibility measurements run D and, for comparison, run B from the nearly hydrostatic measurements. The real part of the ac susceptibility is seen to decrease abruptly by 1-2 nV upon cooling through the superconducting transition. A temperature-dependent background signal  $\chi'_b(T)$  has been subtracted from the data;  $\chi'_b(T)$  is obtained by measuring the ac susceptibility at pressures too low to induce superconductivity. The relatively low noise level is achieved primarily by averaging multiple measurements. For run D, the 1-2 nV magnitude of the superconducting transition is consistent with our expectation from the estimated sample dimensions and Equation 3.9. However, for runs A, B and C the magnitude of the superconducting transition is a factor of  $\sim 3$  smaller than expected for full shielding. Figure 3.28 shows that a relatively small number of poorly connected grains could explain the apparently small shielding fraction. We observed significant broadening of the ruby fluorescence line in run D (no pressure medium) relative to runs A, B and C (dense helium pressure medium), verifying the presence of

non-hydrostatic pressure when no pressure medium is used. Despite this, Figure 4.1 shows there is no significant broadening of the superconducting transition in the non-hydrostatic measurements with no pressure medium (run D) relative to the nearly hydrostatic measurements with helium pressure medium (run B). In run A, near 40 GPa and under applied dc magnetic fields up to  $\sim 500$  Oe,  $T_c$  shifted down at a rate of  $\sim 0.5$  mK/Oe indicating type-II superconductivity.

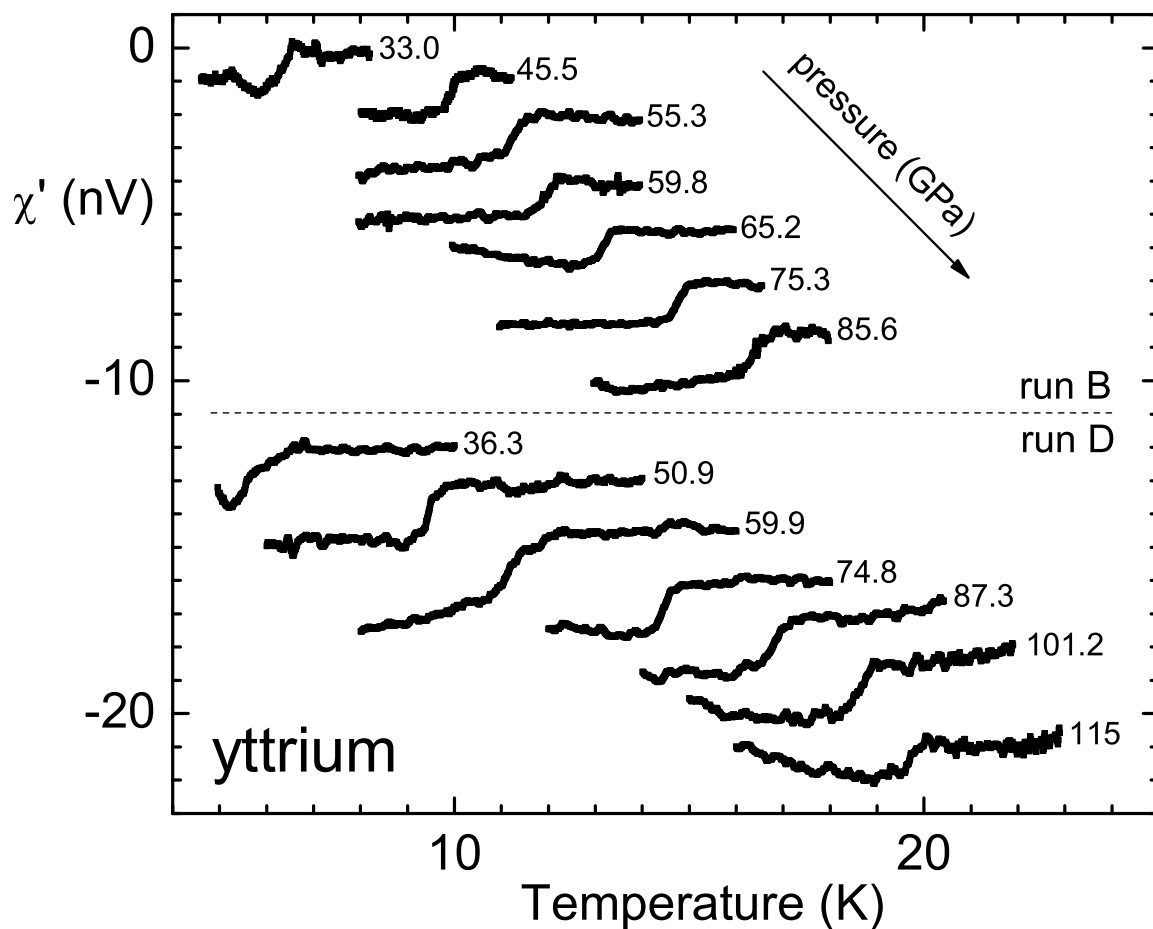


Figure 4.1: Real part of the ac magnetic susceptibility for yttrium at a variety of different pressures ranging from 33 to 115 GPa. Measurements from run B and D are shown.  $T_c$  is seen to increase monotonically with pressure in both runs.

In Figure 4.2 we compare the pressure dependence of  $T_c$  in the nonhydrostatic pressure study (run D) to that obtained under nearly hydrostatic conditions (runs A, B, C). In all experiments  $T_c$  is seen to increase monotonically with pressure. The value of  $T_c$  is determined from the transition midpoint in all four runs; the transition

midpoint typically lies  $\sim 0.5$  K lower than the transition onset. At the highest pressure of 115 GPa transition midpoint lies at 19.5 K with the onset at 20.0 K. At the time, this was highest values of  $T_c$  yet observed for an elemental superconductor, matching that reported [122] for Li at 48 GPa. Today, among the elements, the  $T_c$  of yttrium is exceeded only by calcium with  $T_c = 25\text{K}$  at 160 GPa [50], and in a very recent measurement performed by M. Debessai by Sc with  $T_c = 19.6\text{K}$  (ac susceptibility midpoint) at 106 GPa. The values for Li and Ca were determined by Shimizu *et al.* from the transition onset in the electrical resistivity. It is well known that the resistivity onset typically lies at a higher temperature than the susceptibility onset.

At our highest pressure,  $115 \pm 5$  GPa, the ruby fluorescence line became very broad and weak, resulting in the relatively large uncertainty in our pressure determination for this point, as seen in Figure 4.2. After the measurement at 115 GPa, we increased the force applied to the anvils, but  $T_c$  did not change; unfortunately, we were no longer able to detect the ruby fluorescence line. Presumably either the applied force did not lead to an increase in pressure in the cell or  $T_c(P)$  reached a maximum at these pressures. Subsequent further experience with diamond anvils of the same geometry leads us to believe that the pressure did not saturate, suggesting that  $T_c$  indeed passes through a maximum near 115 GPa. There is excellent agreement between the  $T_c(P)$  dependences for Y in the three nearly hydrostatic runs A, B, C in Figure 4.2. It seems rather remarkable that these dependences agree so closely with the  $T_c(P)$  dependence obtained in the nonhydrostatic experiment (run D) where no pressure medium was used and the diamond anvils pressed directly onto the Y sample. As pointed out previously [123], there are significant differences between the present  $T_c(P)$  dependences and those from earlier studies [117] under quasihydrostatic pressure with solid steatite pressure medium. However, these differences may be due at least in part to the differing techniques used to determine the pressure.

At room temperature, yttrium undergoes a Sm-type to dhcp transition at 32 GPa and a dhcp to trigonal transition at 44 GPa [124]. Assuming that these structural phase boundaries do not depend strongly on temperature, the data in Figure 4.2 does not extend to low enough pressure to comment on the effect of the Sm-type

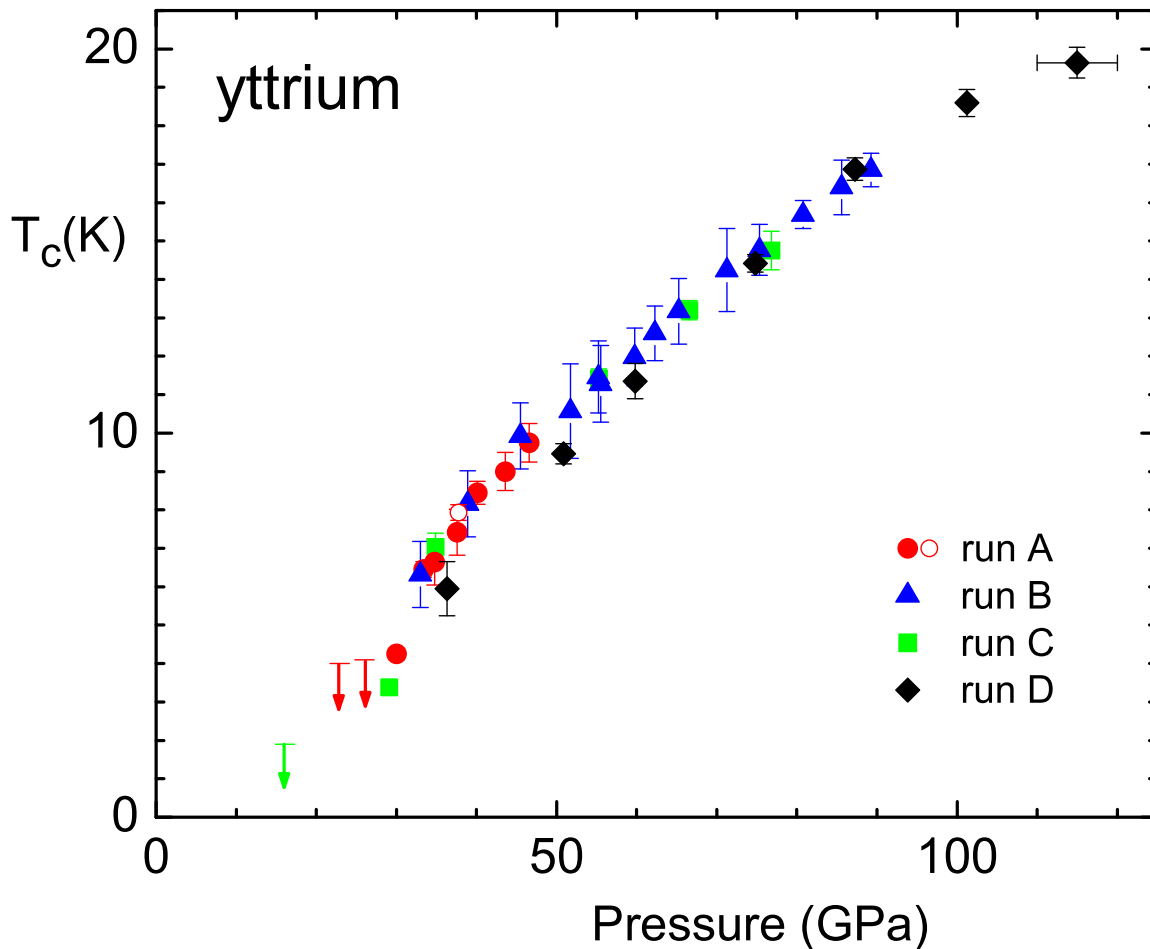


Figure 4.2: Data points give midpoint of the superconducting transition in the ac susceptibility of yttrium metal versus pressure. Vertical error bars represent the width of the transition. Data for all runs taken with increasing pressure except for the final point (open red circle) in run A. Vertical arrows for  $P \leq 30$  GPa indicate the absence of superconductivity above lowest measured temperature.

to dhcp transition on superconductivity. The dhcp to trigonal transition appears to have little, if any, effect on  $T_c$ . It appears that the structure of yttrium has not been studied to pressures higher than 50 GPa [124]. Structural information to much higher pressures (preferably at low temperature) would clarify whether the possible maximum in  $T_c$  for yttrium near 115 GPa is due to a structural phase transition.

### Scandium

I performed a single high pressure experiment on pure scandium metal. The culet diameter of the diamonds was 0.4 mm. A miniature Sc sample ( $\sim 50 \mu\text{m}$  square by  $\sim 20 \mu\text{m}$  thick) was cut from a high purity ingot (99.98% metal basis) obtained from R. W. McCallum and K. W. Dennis of the Materials Preparation Center of the Ames Laboratory and placed in a  $180 \mu\text{m}$  hole in a gasket of  $\text{Ni}_{0.85}\text{Mo}_{0.15}$  alloy preindented to  $45 \mu\text{m}$  thickness. The space surrounding the sample is filled with helium. At the highest pressure, the Sc sample remained completely surrounded by the nearly hydrostatic dense helium. The  $R_1$  ruby fluorescence line remains sharp up to the highest pressures confirming the near hydrostaticity of the pressure environment. To reduce the possibility of He diffusion into the diamond anvils, the temperature was kept below 180 K during the entire experiment. Following the initial compression at 1.6 K to seal the superfluid helium inside the cell, the pressure was only changed between 100 and 180 K.

In Figure 4.3, we show the results of the Sc ac magnetic susceptibility measurements for nearly hydrostatic pressure from 54.3 to 74.2 GPa. The real part of the ac susceptibility  $\chi'(T)$  decreases sharply by 3-4 nV on cooling through the superconducting transition. Similar to the Y experiments, the magnitude of the superconducting transition is a factor of 2-3 smaller than expected for 100% shielding. With pressure,  $T_c$  is seen to increase monotonically. Signal fluctuations and artifacts arising from the  $^4\text{He}$  boiling point and superfluid transition prevented the acquisition of reliable data below 4 K. Scandium is known to remain in the Sc-II crystal structure over the entire range in pressure of the present experiment [125]. The shift in  $T_c \simeq 8.2$  K under an applied dc magnetic field up to 500 Oe was less than the experimental resolution, implying that  $|dT_c/dH| \lesssim 0.3$  mK/Oe. Since values of  $dT_c/dH$  at low fields for for

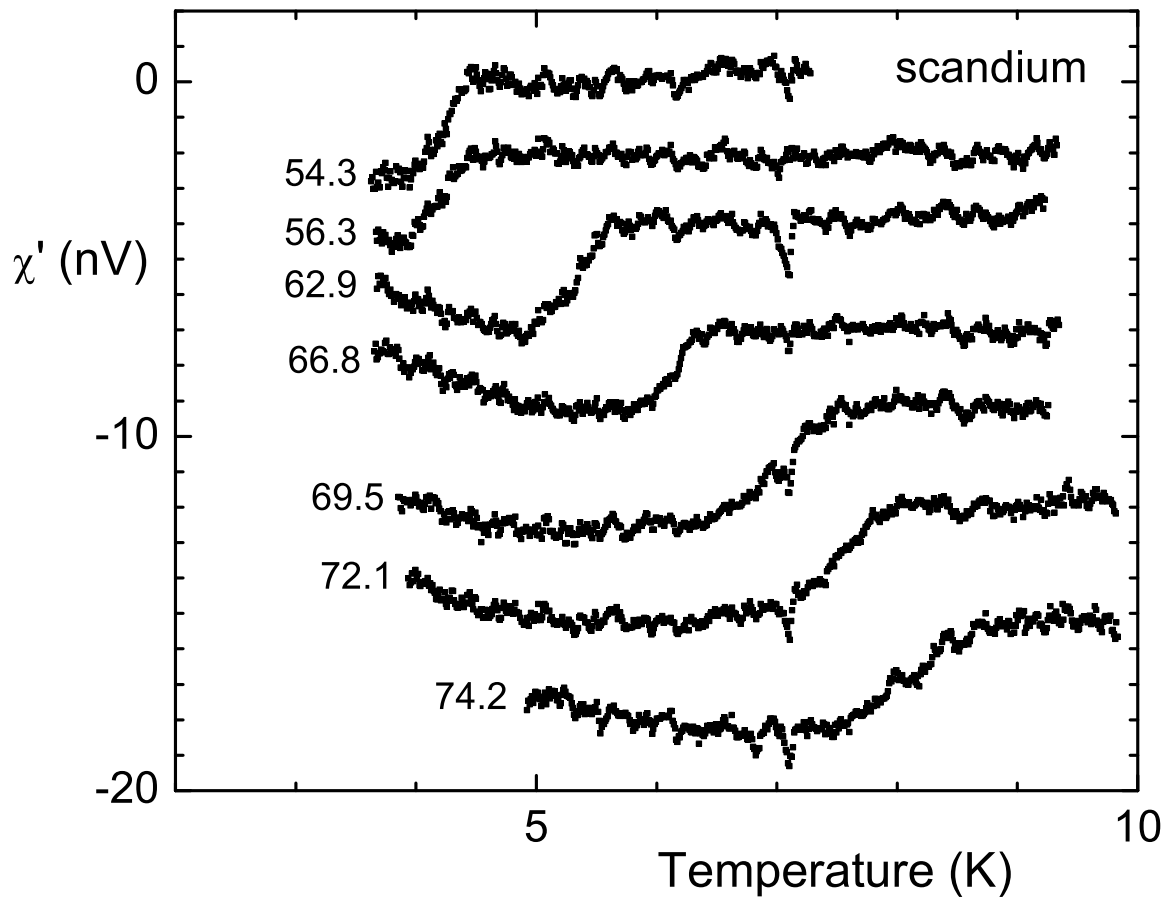


Figure 4.3: Real part of the ac magnetic susceptibility in nanovolts versus temperature for Sc at different pressures ranging from 54.3 to 74.2 GPa. Curves are shifted vertically for clarity. The superconducting transition temperature  $T_c$ , which is defined by the transition midpoint, is seen to increase monotonically with pressure.

type I superconductors are typically a few mK/Oe, the superconductivity in Sc is likely type II, as in La and Y.

In Figure 4.4, the dependence of  $T_c$  on pressure for Sc is shown from the present experiment to 74.2 GPa and compared with the previous quasihydrostatic pressure results of Wittig *et al.* [118] to 21.5 GPa. Note that the dependence of  $T_c$  on pressure appears to be reversible within this pressure range. It is worth noting that, in contrast to the results for Y, the dependence of  $T_c$  on pressure for Sc exhibits an upward (positive) curvature, in spite of the fact that the compressibility decreases with increasing pressure. The accelerating increase in  $T_c$  with pressure in Sc gives hope that much higher values of  $T_c$  can be reached in future experiments. This is confirmed in a recent experiment of M. Debessai where  $T_c \sim 19.6$  K (ac susceptibility midpoint) at 106 GPa.

## Lutetium

A single high pressure ac susceptibility experiment was performed on pure lutetium metal. Anvils beveled from 350 to 180  $\mu\text{m}$  (7 degree bevel angle) were used. The gasket material was the alloy  $\text{W}_{0.75}\text{Re}_{0.25}$ . The gasket was preindented to 29  $\mu\text{m}$  and a 90  $\mu\text{m}$  hole was drilled (spark-cut) through the center of the gasket. In this experiment, no pressure medium was used in order to keep the sample as large as possible. Several small chips of lutetium were cut from an ingot provided by R. W. McCallum and K. W. Dennis of the Materials Preparation Center of the Ames Laboratory and packed into the hole in the gasket along with about five ruby spheres. Lutetium is quite corrosion resistant and so samples were loaded in air rather than inside the argon-filled glovebox as some of the other materials were. The initial pressurizing of the sample was performed at room temperature. Pressure is gradually increased until the hole completely closes around the lutetium sample; at this point the pressure on the sample was approximately 20 GPa and the diameter of the sample was 83  $\mu\text{m}$ . The thickness of the sample was estimated to be less than 25  $\mu\text{m}$ .

After the initial pressurization, the sample was cooled down and the susceptibility monitored for a superconducting transition. Because the  $\text{W}_{0.75}\text{Re}_{0.25}$  gasket superconducts below 5 K, useful data could not be collected at or below this temperature.

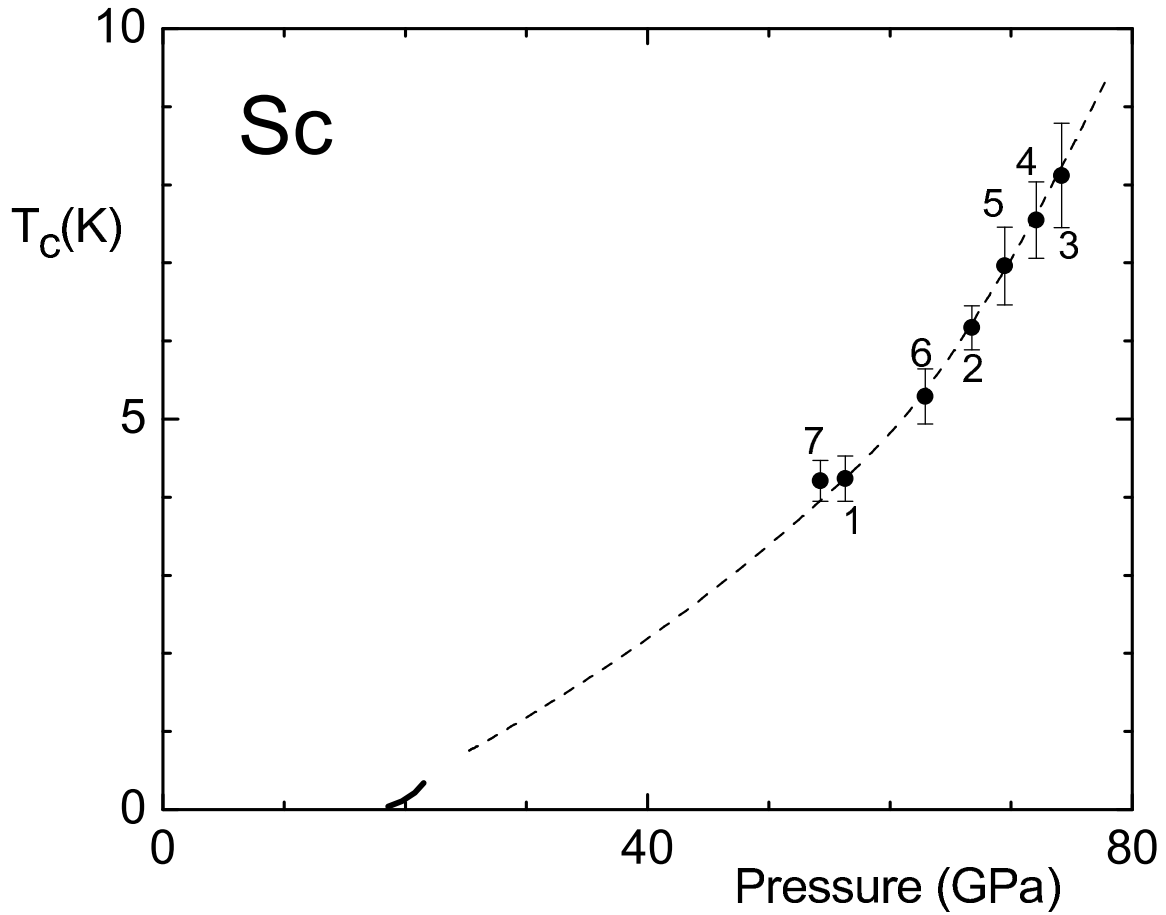


Figure 4.4: Superconducting transition temperature  $T_c$  versus pressure to 74.2 GPa for Sc. Numbers give order of measurement. Dashed line is guide to the eyes and links present data ( $\bullet$ ) to previous results of Wittig *et al.* [118] to 21.5 GPa (short solid line).

Pressure was increased up to a maximum value of 174 GPa and then released back down to ambient pressure without catastrophic failure of the anvils. After releasing, only one of the anvils showed the standard ring crack pattern [89] expected for bevelled anvil experiments in this pressure range.

Above 140 GPa the ruby signal became too small to detect. At 140 GPa the membrane pressure was 45 bars. AC susceptibility curves were measured at several membrane pressures between 45 bars and 80 bars. The dependence of sample pressure on membrane pressure below 45 bars is well described by a simple linear fit, making extrapolation of this curve to higher pressures seem reasonable. However, in order to check the validity of this extrapolation, we measured the pressure using the diamond vibron manometer. The measurements were performed using our 40 $\times$  objective (21.1 mm working distance); the high magnification resulted in a Raman spectrum originating from a region  $\sim 20 \mu\text{m}$  in diameter near the tip of the diamond; the Raman signal from outside of this region was rejected by the confocal<sup>1</sup> microscope optics. The result of this measurement is shown in Figure 3.19 (b). Noting that the intensity of the diamond vibron signal drops sharply near  $1650 \text{ cm}^{-1}$ , we estimate the pressure  $P = 174 \text{ GPa}$  using Equation 3.5. Extrapolation of the membrane pressure severely overestimates the pressure in the cell. This is not too surprising given the way that most of the loading curves shown in Figure 3.3 take on negative curvature at higher pressures. The saturation of sample pressure at high membrane pressure in this experiment may be due to “cupping” of the diamond anvils. At high pressure the diamonds begin to deform, so that the culets become concave (cupped). Figure 4.5 shows a photograph of the sample and gasket at 174 GPa. It appears that the dark halo just inside of the edge of the diamond tip is a signature of cupping. When the diamonds cup, one expects the region of the diamond gasket interface near the edge of the tip to show the greatest angle with respect to the incident illumination thus reducing the brightness of this area.

Several measurements of susceptibility versus temperature were taken at pressures of 40, 62 and 69 GPa and no superconducting transition was detected between 5 and 40 K. The first superconducting transition was detected after increasing the pressure

---

<sup>1</sup>Confocal microscopy is discussed briefly in Appendix C.

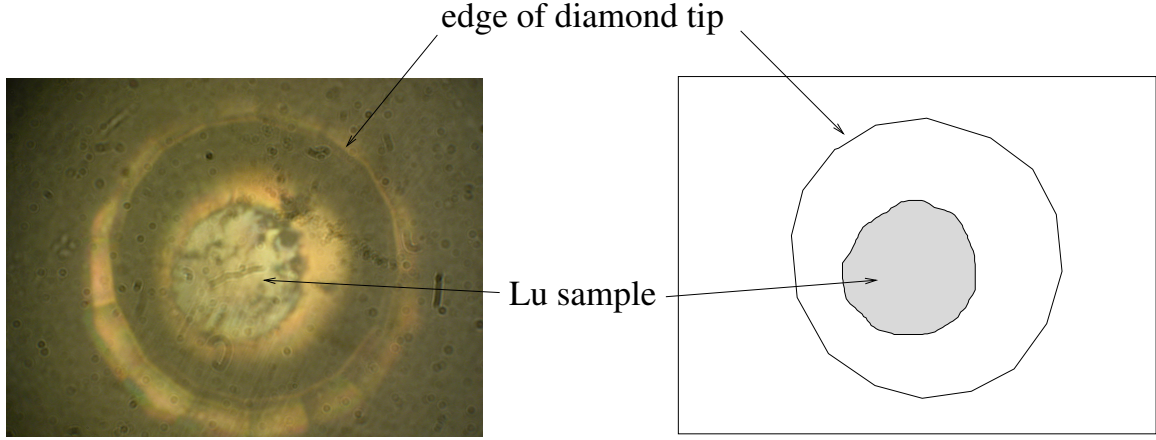


Figure 4.5: Image of the Lu sample at 174 GPa. To the left is a photograph taken using the Nikon Optiphot microscope and 40 $\times$  objective with reflected light illumination. To the right is a traced drawing indicating the location of the edge of the diamond tip and the sample. The diameter of the diamond tip is  $\sim 180 \mu\text{m}$ .

to 88 GPa. As we continued to increase the pressure up to 174 GPa,  $T_c$  increased monotonically. In Figure 4.6, we show samples of the superconducting transitions. It can be seen that the susceptibility drops by nearly 30 nV at  $T_c$ . The measured sample diameter combined with the estimated thickness of  $15 \mu\text{m}$  suggests a transition of 28 nV using Equation 3.9, indicating that the shielding for this sample must be at or near 100%. The quality of the data given the extremely tiny sample size is quite remarkable.

At most of the pressures, the field dependence of  $T_c$  was measured by applying a dc field up to 500 Oe. In Figure 4.7 we show superconducting transitions measured at 140 GPa and fields of 0, 167, 333 and 500 G. The transition temperature is observed to shift downward monotonically and reversibly, as expected for a superconductor. No difference in behavior was observed depending on whether the field was applied above or below  $T_c$  indicating an absence of flux trapping effects. The initial slope of  $T_c$  versus field remains approximately constant over the entire pressure range studied, with the average value of  $\sim 0.6 \text{ mK/Oe}$  consistent with type II superconductivity. The size of the transition is seen to become smaller with increasing field. Recall from Section 3.6 that the field near the edge of a pancake shaped superconductor will be larger than the average field by  $1/(1 - D)$  where  $D$  is the demagnetization

factor. For this experiment the demagnetization effect leads to approximately a  $3\times$  enhancement of the field at the edge of the sample. The size of the transition is reduced with increasing field because the effective size of the sample is reduced when the critical field at the edge of the sample is exceeded. The ability to resolve such behavior is a testament to the high sensitivity of the present apparatus.

In Figure 4.8 we show the pressure dependence of the  $T_c$  in lutetium to 174 GPa. We measured several transitions between 140 and 174 GPa where we have no measurement of the pressure. For these points we estimate the pressure from the membrane pressure using a linear interpolation between 140 GPa at 45 bars on the membrane to 174 GPa at 80 bars on the membrane. In Figure 4.8 the open circles indicate points for which the pressure was interpolated. Lutetium has been found to transform from a dhcp to hR24 structure near 88 GPa (at room-temperature) and remain in this structure up to at least 163 GPa [126]. However, our data does not extend to low enough pressure to comment on the effect of this structural transition on  $T_c$ .

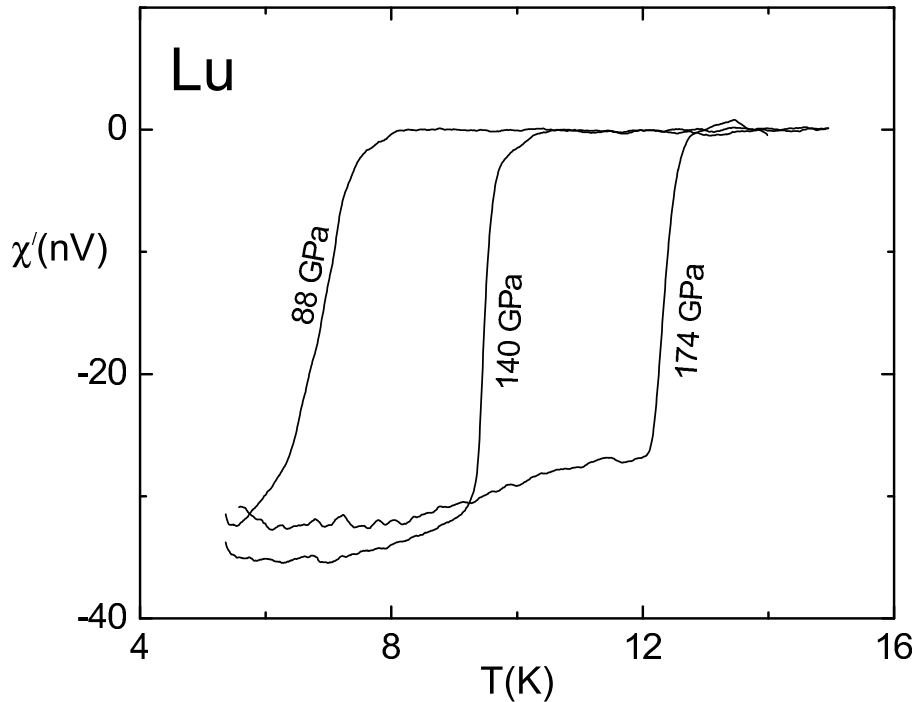


Figure 4.6: Ac susceptibility versus temperature for Lu at several pressures. At 174 GPa the midpoint of the superconducting transition reaches 12.35 K.

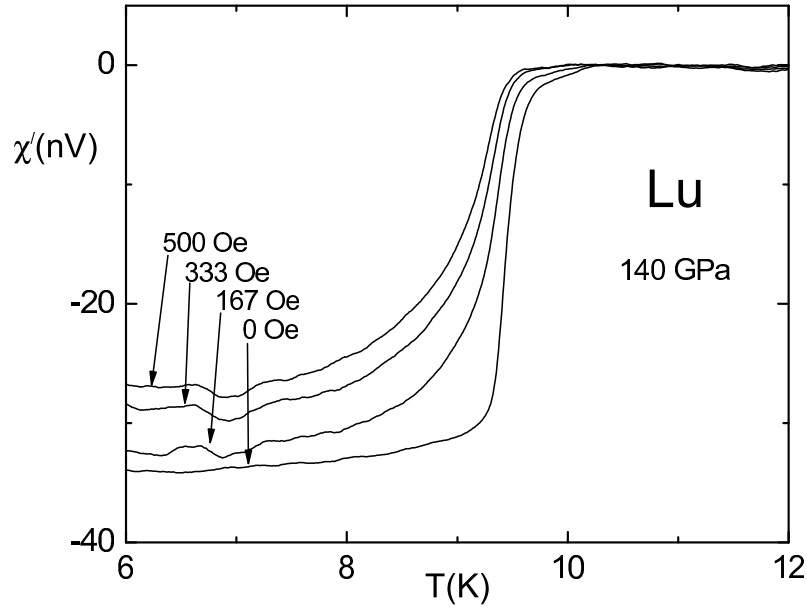


Figure 4.7: Dependence of superconducting transition on dc magnetic field for Lu at 140 GPa.  $T_c$  is determined from the midpoint of the transition in the ac magnetic susceptibility.

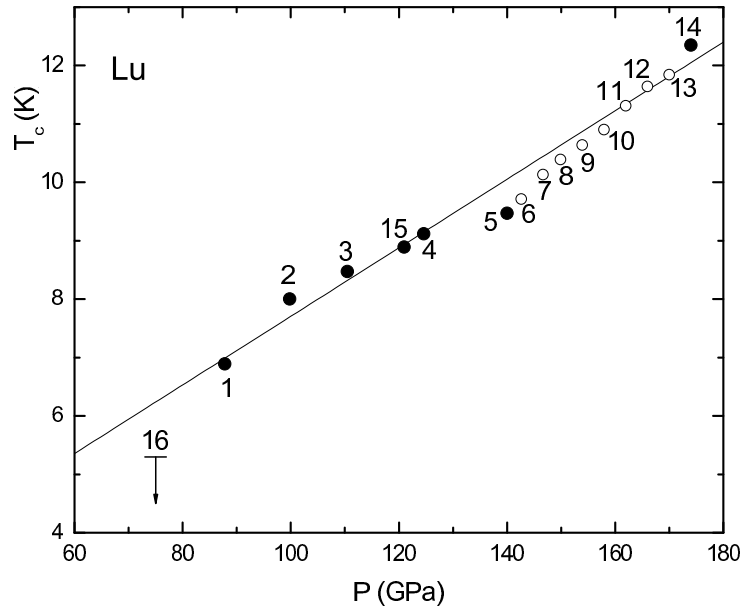


Figure 4.8:  $T_c$  versus pressure for pure Lu metal. Numbers indicate order of measurement. The open circles indicate points for which we have estimated the pressure from the membrane pressure as described in the text.

## Europium

A total of three separate experiments were carried out on europium metal. The europium sample was received from R. W. McCallum and K. W. Dennis of the Materials Preparation Center of the Ames Laboratory. The first experiment was 4-point resistivity, the second experiment was quasi 4-point resistivity and the third experiment was ac susceptibility. The resistivity experiments were performed using the technique described in Section 3.7 using rhenium as gasket material and synthetic type Ib anvils with 0.3 mm diameter culets. Preparation of the resistivity leads and sample loading was performed by T. Matsuoka in both resistivity experiments. Because europium is extremely reactive, samples were loaded inside the argon-filled glovebox for all three experiments. The ac resistivity technique (see Figure 3.30) employed a Stanford Research lock-in amplifier operating at 13 Hz. In all three experiments, following initial pressurization at room temperature, the temperature of the cell was kept below 180 K in order to prevent any reaction between the europium and the diamonds or gasket.

In the first resistivity measurement, pressure was increased monotonically and temperature versus resistance was measured at pressures of 14, 34 and 36.4 GPa. Upon increasing the pressure above 36.4 GPa, several of the wires appeared to short to the gasket, forcing us to stop the experiment. No superconducting transition was detected down to 1.6 K.

The second resistivity experiment was planned to be another 4-point resistivity experiment but during loading of the sample, two of the platinum electrodes broke. The remaining two electrodes contacted the sample and the method of Figure 3.29 (“quasi four-point”) was used to measure resistance. We proceeded with the measurement since it would still be possible to resolve a superconducting transition using such a technique. At the beginning of the experiment pressure was immediately increased to 50 GPa. From that point, pressure was increased monotonically to 63 and 80 GPa. Above 63 GPa the size of the ruby fluorescence peak became too small to resolve and so the final pressure 80 GPa was determined through an extrapolation of the membrane pressure versus sample pressure curve. At this pressure (80 GPa) we observed a sharp drop in the resistivity near 4 K, indicating a possible superconducting transition (Figure 4.9). We measured this transition several times. Figure 4.10

shows the result of applying a dc magnetic field of 500 Oe. This data was collected by allowing the system to slowly warm up from 1.6 K and flipping the field on and off every  $\sim 30$  seconds. This method allows extremely accurate comparison of the zero dc field and 500 Oe data. The transition is seen to shift down by approximately 0.4 mK/Oe, comparable with the expectation for a type II superconductor and similar to the values observed for Sc, Y and Lu.

Having approached the maximum pressure possible using the present configuration, we reduced the pressure (rather than risk a failure of the diamonds on increasing the pressure) in order to check if the feature at 4 K indeed shifted under pressure. Upon reducing the pressure the leads appeared to short to the gasket, again making further experimentation impossible. This leads one to suspect that the transition observed at 4 K may have in fact resulted from a small short between the electrodes and gasket combined the superconducting transition of the rhenium gasket itself (since strained rhenium is known to superconduct at approximately 4 K).

The third measurement using ac susceptibility was performed in order to see if we could confirm that the transition observed at 4 K was due to the europium sample. Type Ia diamonds beveled from 350 to 180  $\mu\text{m}$  (7 degree bevel angle) were used with a gasket of the  $\text{W}_{0.75}\text{Re}_{0.25}$  alloy, pre-indented to 50  $\mu\text{m}$ . Europium and several ruby spheres were loaded into the cell. Data was collected between 5 and 35 K at pressures of 62, 86, 100, 114, 135 and 143 GPa, but no superconducting transition could be resolved. Three more measurements were performed at pressures higher than 143 GPa. Linear extrapolation of the sample pressure versus membrane pressure would give pressures of 157, 169 and 181 GPa. However, in light of the results of the diamond vibron measurement during the Lu experiment, the maximum pressure of the sample probably did not exceed  $\sim 160$  GPa. At the highest pressure the clamp was removed from the cryostat and the sample was carefully examined under a high powered microscope. It was found that the diameter of the sample was  $\sim 30$   $\mu\text{m}$ . At this size, with full shielding, one would expect a transition of not more than 1-2 nV. Therefore, it would only be possible to detect the transition if the shielding were near 100% and the transition remained sharp (less than  $\sim 2$  K wide). If either of these conditions were not met, one could fail to detect a transition that was in fact

present.

Thus, at this point, there remains a question as to whether the feature observed near 4 K at 80 GPa in the second resistivity experiment was indeed the first observation of pressure induced superconductivity in europium or was due to superconductivity of the gasket. A susceptibility experiment utilizing a significantly larger sample could settle this question.

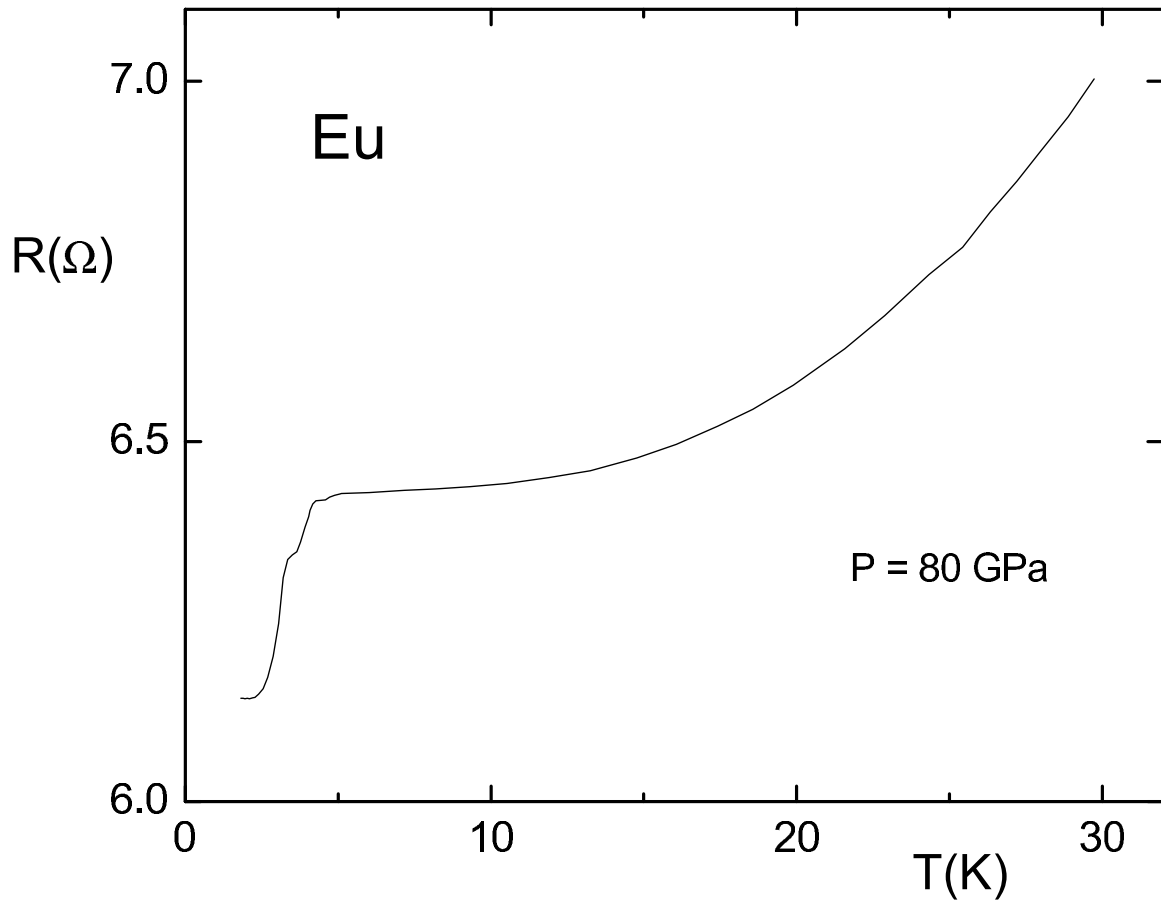


Figure 4.9: Resistance versus Temperature for Eu at 80 GPa in a two-point resistivity measurement. There appears to be a superconducting transition near 4 K.

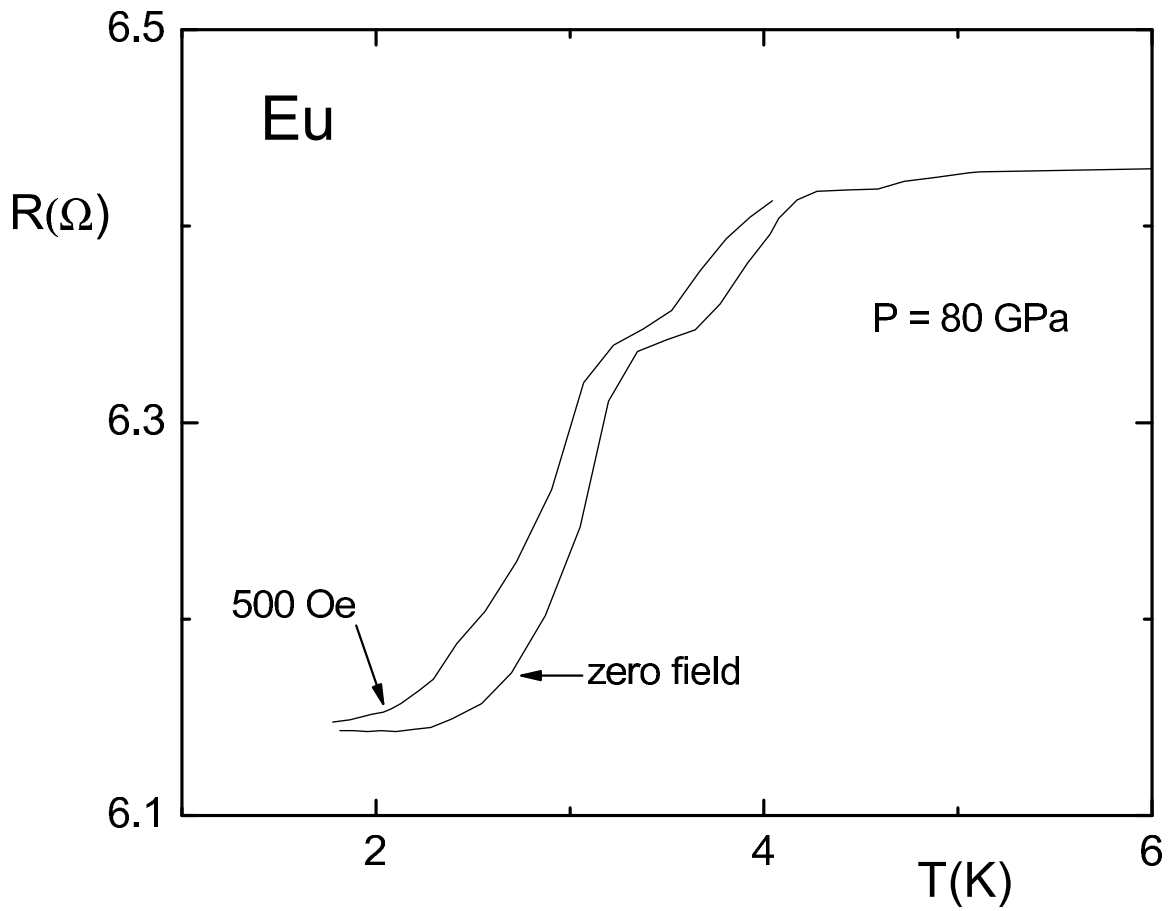


Figure 4.10: Field dependence of the possible superconducting transition in Eu at 80 GPa. Both curves are measured during the same warming run by switching the magnetic field on and off every  $\sim 30$  s.

## 4.1.2 Analysis

### McMillan Equation Fits

We now consider our results in light of the McMillan equation [46, 127]

$$T_c \simeq \frac{\langle \omega \rangle}{1.20} \exp \left[ \frac{-1.04(1 + \lambda)}{\lambda - \mu^*(1 + 0.62\lambda)} \right], \quad (4.1)$$

which is a generalization of the BCS formula (Equation 2.1) valid for moderately strong electron-phonon coupling ( $\lambda \leq 1.5$ ). Equation 4.1 relates  $T_c$  to the electron-phonon coupling parameter  $\lambda$ , an average phonon frequency  $\langle \omega \rangle$ , and a Coulomb repulsion term  $\mu^*$ . We assume  $\mu^*$  is independent of pressure and assign  $\mu^* = 0.1$ . The electron-phonon coupling parameter is given by

$$\lambda = \frac{N(E_F) \langle I^2 \rangle}{M \langle \omega^2 \rangle}, \quad (4.2)$$

where  $\eta \equiv N(E_F) \langle I^2 \rangle$  is the Hopfield parameter [47] given by the product of the electronic density of states and the average-squared electron-phonon matrix element and  $M$  is the ionic mass. To explore how  $T_c$  can behave under pressure, it remains to find expressions for the volume dependence of  $\langle \omega \rangle$  and  $\lambda$ .

Following previous analyses [128, 129], we integrate the definition of the lattice Grüneisen parameter,  $\gamma \equiv -d \ln \langle \omega \rangle / d \ln V$ , to obtain an expression for the volume dependence of the average phonon frequency

$$\langle \omega \rangle_V = \langle \omega \rangle_{V_0} [V/V_0]^{-\gamma}. \quad (4.3)$$

Introducing the parameter  $\varphi \equiv \partial \ln \lambda / \partial \ln V$  and integrating, one finds an expression for the volume dependence of the electron-phonon coupling parameter

$$\lambda(V) = \lambda(V_0) [V/V_0]^\varphi, \quad (4.4)$$

where it is easy to show that  $\varphi = \partial \ln \eta / \partial \ln V + 2\gamma$ . The parameter  $\partial \ln \eta / \partial \ln V$  is negative and normally lies near -1 for s,p-metals or -3 to -5 for d-metals [48]. Since  $2\gamma$  is positive, whether  $\lambda$  (and  $T_c$ ) increases or decreases with pressure depends on

whether  $|\partial \ln \eta / \partial \ln V| > 2\gamma$  or vice versa.

We assign the Grüneisen parameter  $\gamma$  values of 1.10, 1.08 and 1.00 for Sc, Y and Lu<sup>2</sup> respectively, based on an average of the values listed in Reference [130]. We assume  $\gamma$  does not vary with pressure. One can estimate the average phonon frequency using the empirical relation [131]  $\langle \omega \rangle \simeq 0.69\Theta_D$ ; for the Debye temperature  $\Theta_D$  we use values from Reference [132] of 345.3 K, 244.4 K and 183.2 K for Sc, Y and Lu respectively. Substituting Equation 4.3 and 4.4 into Equation 4.1 and using the experimentally determined values mentioned above, one obtains an expression for the volume dependence of  $T_c$ . In the present analysis  $\lambda(V_0)$  and  $\partial \ln \eta / \partial \ln V$  are used as fit parameters which, as for  $\gamma$ , are assumed to be independent of pressure. Note that in materials which superconduct at ambient pressure  $\lambda(V_0)$  can be determined directly from Equation 4.1 by inserting the ambient-pressure values of  $T_c$  and  $\Theta_D$ . If only one of  $\lambda(V_0)$  or  $\partial \ln \eta / \partial \ln V$  is used as a fit parameter, and the other is fixed at some estimated value, a good fit to the data is generally not obtained.

We convert pressure to relative volume ( $V/V_0$ ) using the equations of state given for Sc, Y and Lu<sup>3</sup> by Refs. [125], [124] and [126] respectively. Having converted pressure to relative volume, we fit the McMillan equation (Equation 4.1) to the data using the above described procedure. For the Y data, we perform two separate fits, one for the nearly hydrostatic data (runs A, B and C) for  $V/V_0 \geq 0.65$  and one for the non-hydrostatic data (run D). The fits are shown in Figure 4.11 where we plot  $T_c$  versus relative volume. The obtained fit parameters are summarized in Table 4.1. The values for  $\lambda(V_0)$  given in Table 4.1 are reasonably consistent with values estimated by Knapp *et al.* [133] by comparing heat-capacity data at high and low temperatures and with theoretical calculations (see, for example, Refs. [134–136]). The aforementioned references give  $\lambda(V_0)$  in the range 0.3-0.6 for all three elements. At the highest pressures (lowest volumes) we attained in these experiments,  $\lambda$  reaches 0.57, 0.78 and 0.74 for Sc, Y and Lu, respectively, indicating that Equation 4.1 ought to remain valid over the entire range in which we detect superconductivity. The trend that we find in  $\lambda$  under pressure for Sc agrees remarkably well with that found in a

---

<sup>2</sup>The various values of  $\gamma$  given for Lu in Reference [130] vary appreciably from 0.66 to 1.45

<sup>3</sup>For Lu we use the equation of state claimed by Reference [126] to be valid for the pressure range 93-163 GPa

Experiment	$\partial \ln \eta / \partial \ln V$	$\lambda(V_0)$
Sc	-4.17	0.20
Y (runs A, B and C)	-2.90	0.44
Y (run D)	-2.91	0.43
Lu	-2.81	0.37

Table 4.1: Parameters obtained by fitting  $T_c$  versus relative volume data shown in Figure 4.11 with the McMillan Equation (Equation 4.1).

recent calculation by Nixon *et al.* [137]. Our obtained values for  $\partial \ln \eta / \partial \ln V$  are close to the range ( $-3 \lesssim \partial \ln \eta / \partial \ln V \lesssim -5$ ) normally found for transition metals [47]. We note that our fit curves would predict at ambient pressure that  $T_c$  equals 0.76  $\mu$ K, 1.1 K and 300 mK for Sc, Y and Lu respectively. Experimentally,  $T_c < 6$  mK for Y [138] and  $T_c \lesssim 50$  mK for Lu and Sc [118, 119]. However, structural phase transitions [124] occur between ambient pressure and the maximum pressures of our experiments so that one would not expect such extrapolations to ambient pressure to be very reliable. Extrapolating to high pressure would predict  $T_c$  reaches 30 K at 130, 165 and 575 GPa for Sc, Y, and Lu, respectively.

The above phenomenological analysis shows that the  $T_c(P)$  dependence observed for Sc, Y and Lu appears consistent with moderately strong-coupled, phonon-mediated superconductivity using reasonable values of the averaged parameters. However, to pinpoint the mechanism responsible for the significant increase in  $T_c$  with pressure in experiment, detailed electronic structure calculations for are clearly needed. Such calculations, which included pressure-dependent changes in the lattice vibration spectrum, have very recently been carried out for Y by Yin *et al.* [53]. They conclude that the large positive value of  $dT_c/dP$  arises from a pressure-induced softening in the transverse phonon modes, i.e. a negative mode Gruneisen parameter, in contrast to the positive value  $\gamma \simeq +1.08$  used in the above phenomenological analysis. Calculations by Lei *et al.* [139] for Y and Nixon *et al.* [137] for Sc, indicate that a drop in  $N(E_F)$  under pressure is more than compensated by the rapid increase of  $\lambda$  and  $\eta$  leading the observed increase in  $T_c$ .

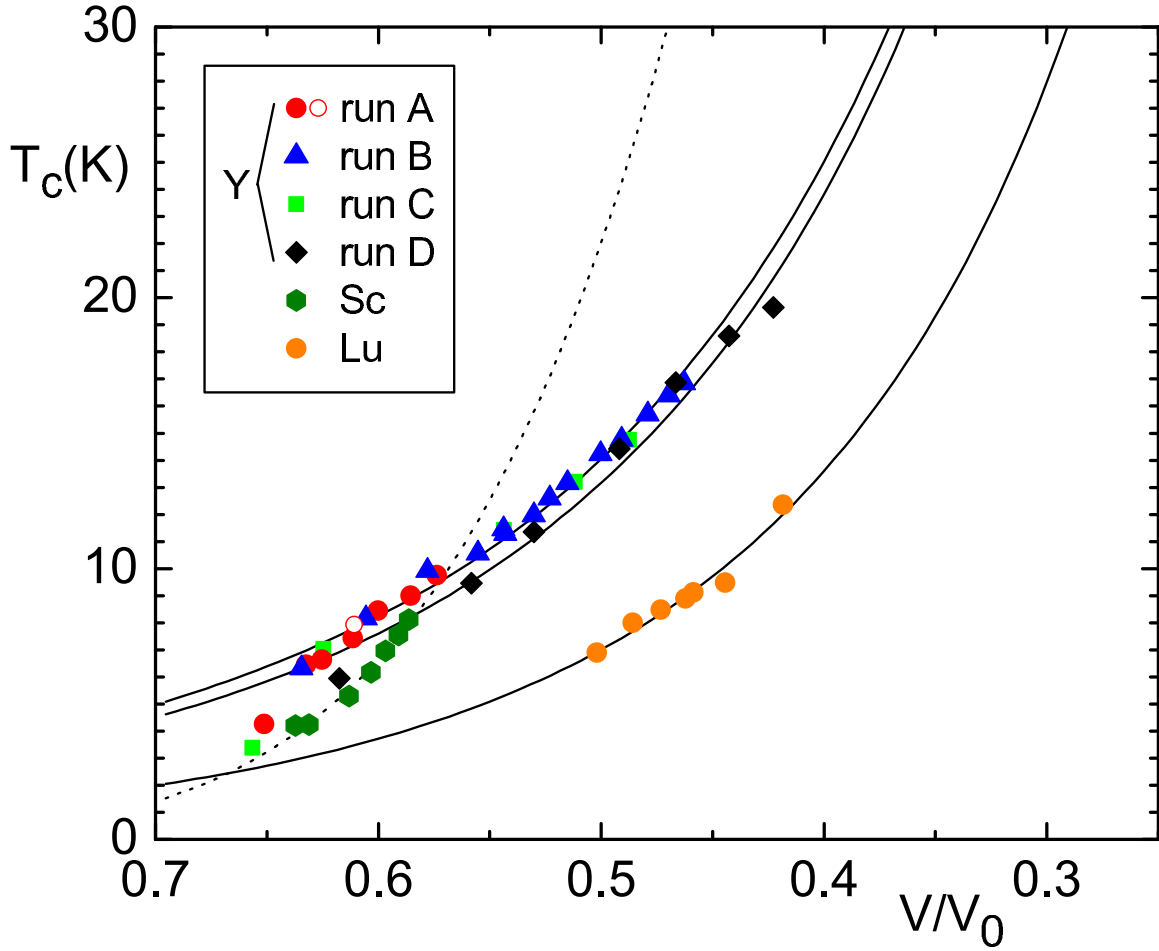


Figure 4.11:  $T_c$  versus relative volume for Sc, Y and Lu shown with the McMillan equation fit curves described in the text. The upper curve through the Y data is a fit of the nearly hydrostatic data (excluding the two lowest pressure data points at  $V/V_0 \geq 0.65$ ) while the lower curve through the Y data is a fit of the non-hydrostatic data. The dashed curve is the fit for Sc.

## d-Band Occupancy

Here we carry out an analysis of our results in terms of  $R_{WS}/R_c$ , the ratio of the Wigner-Seitz radius to the ion core radius and relate this ratio to the occupancy of the d-band. Similar ratios were discussed at length in Section 2.4 as applied to magnetism, the crystal structure of the rare-earths and the metal-insulator transition. Many years ago, Johansson and Rosengren showed that the  $T_c$  values of Y, La, Lu, and alloys thereof, are a smooth function of a similar ratio<sup>4</sup> with  $T_c$  increasing as the ratio decreases [81]. In the present analysis, values of  $R_{WS}$  at ambient pressure are calculated using Equation 2.10 with the molar volumes given by Reference [80]. For  $R_c$  we use the trivalent ionic radii from Reference [80] and neglect the details of crystal structure by using the values for coordination number equal to 8. We assume that  $R_c$  is independent of pressure. Table 4.1.2 contains a summary of these values. To determine  $R_{WS}/R_c$  at high pressure we simply scale the ratio by  $(V/V_0)^{\frac{1}{3}}$  where  $V/V_0$  is given by the equations of state for Sc, Y, La and Lu in References [125], [124] and [126].

In Figure 4.13 we plot  $T_c$  versus  $R_{WS}/R_c$  for the non-magnetic, trivalent, rare-earth metals Sc, Y, La and Lu. The rather complex behavior of La under pressure has been attributed by Tissen *et al.* [140] to the presence of van Hove singularities in the density of states. One should keep in mind when examining Figure 4.13 that both hydrostatic and quasi-hydrostatic pressure experiments have been plotted together. That the hydrostaticity of the experiment can have some influence on the result is evident from a comparison of the earlier data on La of Wittig [119] (solid blue line) with that of later, more hydrostatic experiments of Tissen *et al.* [140] (dashed blue line). In addition, the earlier experiments of Wittig *et al.* determined pressure from the  $T_c$  of a Pb sample, while the present results have used the ruby fluorescence manometer (or in the case of the highest pressure point for Lu, the diamond vibron manometer). These various calibrations may lead to differences in the  $T_c(P)$  dependences.

In spite of all of these qualifications, some simple systematics are evident in Figure 4.13.  $T_c$  generally increases with pressure (decreasing  $R_{WS}/R_c$ ), with the three

---

<sup>4</sup>In fact, Reference [81] discusses  $T_c$  in terms of  $R_{WS}/R_c$  where  $R_{WS}$  is the Wigner-Seitz radius which minimizes the energy for a given value of the pseudopotential core radius  $R_c$ . The basic idea is the same but in the present treatment we use empirically determined values for the radii.

non-superconducting metals becoming superconducting under pressure. It appears that the  $T_c$  values of all four elements do not exceed  $\sim 1$  K until ratio  $R_{WS}/R_c$  is reduced below  $\sim 2.1$ . This clarifies why La is the only member of this series that is superconducting at ambient pressure; at ambient pressure  $R_{WS}/R_c = 2.02$  for La whereas the other three metals have  $R_{WS}/R_c > 2.1$ .

Under pressure, the number of d-electrons in Sc, Y, La and Lu increases. Duthie and Pettifor [83] have shown that the occupation of the d-band is closely related to the relative volume of the ion core ( $R_{WS}/R_c > 2.1$ ) with smaller relative volumes leading to greater occupation of the d-band. The effect of compression on the d-band occupancy has been calculated for Y, La and Lu by Pettifor *et al.* [83,141] and for Y and Sc by Pickett [142]. It would be preferable to have  $N_d$  versus pressure calculated for all four metals within one consistent framework, but such results do not appear to be available. In Figure 4.12, we plot  $N_d$  versus  $R_{WS}/R_c$  for all four metals. Noting the differences in the dependences for Y calculated by Pettifor and Pickett, it becomes apparent that one should not attempt to take the exact values of  $N_d$  too literally. However, it is clear that all four metals show a similar, roughly quadratic increase in  $N_d$  as a function of  $R_{WS}/R_c$ . In order to make some general arguments, we make the simplifying approximation that the dependence of  $N_d$  on  $R_{WS}/R_c$  is the same for all four metals, and take that dependence to be an average of all of the calculated values shown in Figure 4.12. Since all of the individual dependences are well fit by quadratic curves, we formulate the average dependence as a quadratic

$$N_d \approx 0.60 \left( \frac{R_{WS}}{R_c} \right)^2 - 3.79 \left( \frac{R_{WS}}{R_c} \right) + 7.42. \quad (4.5)$$

This average dependence is shown in Figure 4.12 by the thick grey line. When  $N_d = 3$ , all of the s-electrons have been dumped into the d-band and  $N_d$  ceases to increase under pressure. On average, this ought to happen when  $R_{WS}/R_c \sim 1.54$ , although it looks like for La completion of s-d transfer may occur at somewhat higher values of the ratio and for Y it may occur at somewhat smaller values. Since  $T_c$  is increasing with  $N_d$ , one expects that when the d-occupation reaches a constant value of  $N_d = 3$  the pressure dependence of  $T_c$  should change, perhaps passing through a maximum.

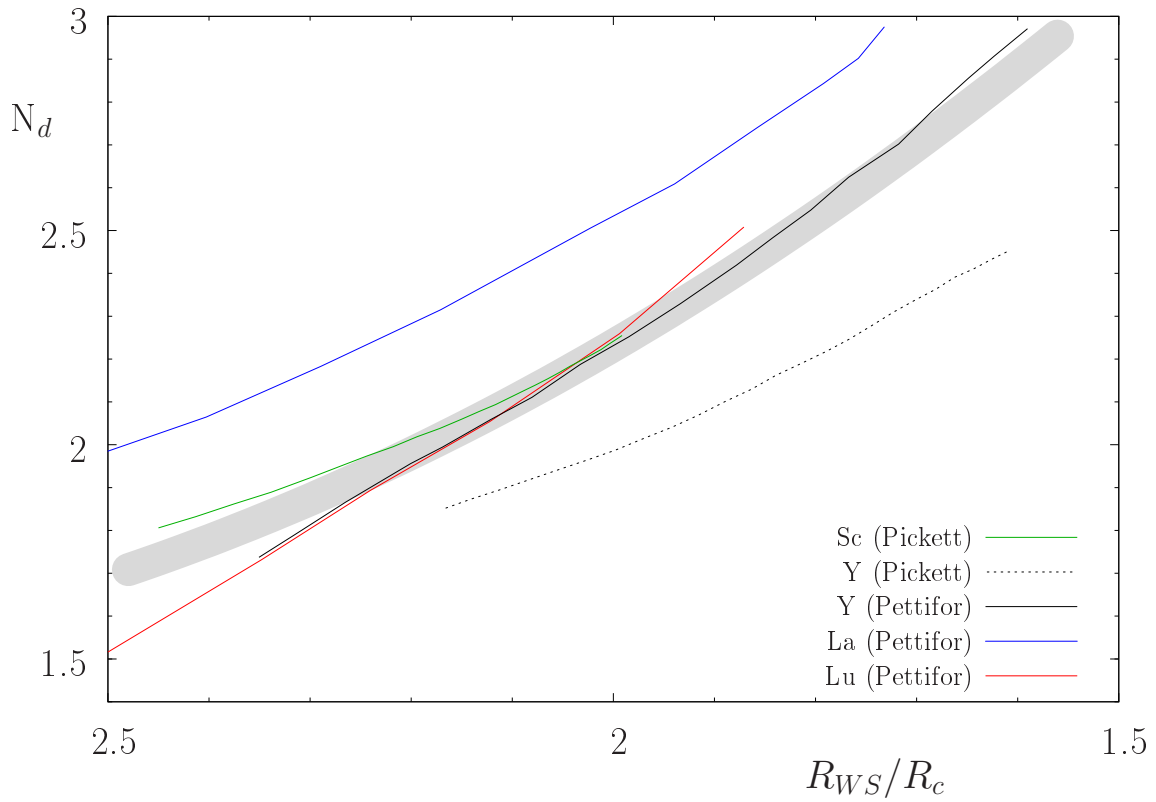


Figure 4.12: Calculated d-band occupancy  $N_d$  versus  $R_{WS}/R_c$ . Y, La and Lu curves from Pettifor *et al.* [83,141] and Y and Sc curves from Pickett [142]. The thick grey line represents a quadratic fit of all of the curves. When  $N_d$  reaches 3, all of the s-electrons have been transferred into the d-band.

element	$R_{WS}(\text{\AA})$	$R_c(\text{\AA})$	$R_{WS}/R_c$
Sc	1.84	0.75	2.45
Y	1.99	0.90	2.21
La	2.08	1.03	2.02
Lu	1.92	0.86	2.23

Table 4.2: Ambient pressure values of  $R_{WS}$ ,  $R_c$  and  $R_{WS}/R_c$  as determined from data given in Reference [80].

Thus, perhaps the maximum in the  $T_c$  of La is related to completion of s-d transfer. Despite the rather significant approximation of assuming that  $N_d$  is a single function of  $R_{WS}/R_c$  for all four metals, one can at least be reasonably confident in the following statement: Sc, being the least compressible and having the largest ambient pressure value of  $R_{WS}/R_c$ , is the farthest from completion of s-d transfer<sup>5</sup>. This suggests that the present trend in Sc of rapidly increasing  $T_c$  with compression may continue to significantly higher pressures. As we mentioned before, a very recent experiment of M. Debessai has found that  $T_c$  of Sc reaches 19.6 K (ac susceptibility midpoint) at 106 GPa. Above this pressure  $T_c$  drops abruptly to 8 K, probably when the sample transforms from the Sc-II to Sc-III phase. Upon further pressure increase from 106 to 123 GPa (where the experiment ended),  $T_c$  again rises although at a significantly smaller rate than that below 100 GPa.

The Sc-II phase, in which scandium exhibits the highest  $T_c$ , is an unusual incommensurate host-guest crystal structure [125]. This type of crystal structure was only recently found to exist in high pressure phases of elemental solids [143]. It would certainly be interesting to study these metals to much higher pressures in order to investigate if and when the  $T_c$  for Sc, Y and Lu ceases to increase under pressure, as for La. Such ultra-pressure experiments on Sc are particularly interesting given its exceptionally high  $T_c$ . In addition, Sc undergoes a further structural transition to Sc-IV at 130 GPa [125] that may influence superconductivity.

---

<sup>5</sup>For Sc, it should take pressure on the order of 1 TPa before s-d transfer is completed at  $R_{WS}/R_c = 1.54$

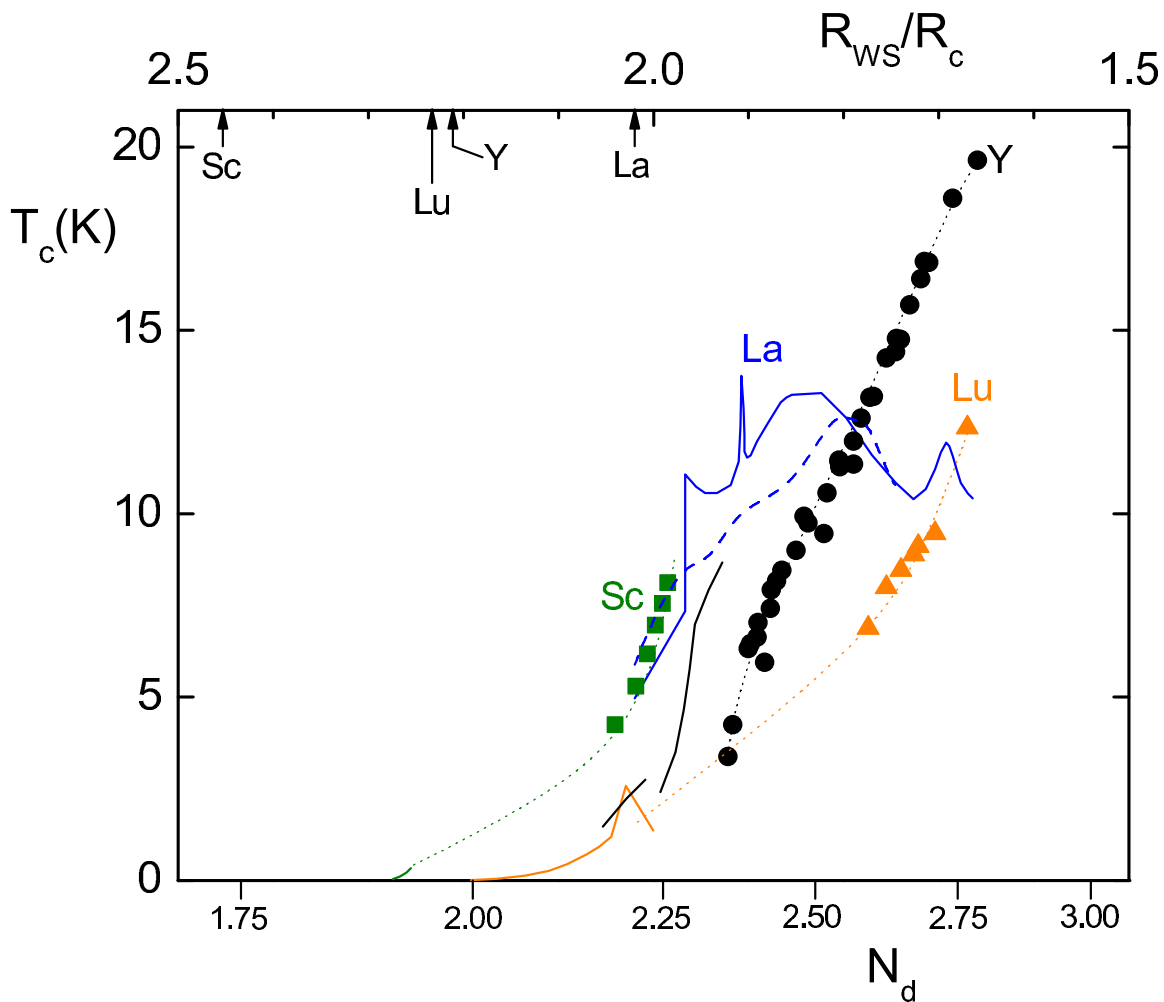


Figure 4.13:  $T_c$  versus  $R_{WS}/R_c$  for the non-magnetic, trivalent, rare-earth metals Sc, Y, La and Lu. The fine dotted lines are a guide to the eye. Solid green, black, blue and orange lines are the data of Wittig *et al.* for Sc [118], Y [138], La [119] and Lu [138] respectively. Dashed blue line is the La data of Tissen *et al.* [140]. Vertical arrows below the upper axis show ambient pressure values of the ratio  $R_{WS}/R_c$  for the indicated elements. Bottom axis shows d-electron occupation as estimated by Equation 4.5.

## 4.2 Low-Z Materials

In Section 2.3 we mentioned that solid metallic hydrogen, by virtue of its very low ionic mass, has been predicted to be superconducting at temperatures as high as room-temperature [55]. The idea of low mass (low  $Z$ ) leading to higher transition temperatures has been around at least since the discovery of the isotope effect in 1950 [21, 22]. Several recent events have resulted in increased interest in low- $Z$  materials as promising candidates for high temperature superconductivity. In March of 2001, Nagamatsu *et al.* [144] reported the discovery of superconductivity at 39 K in  $\text{MgB}_2$ . The critical temperature of  $\text{MgB}_2$  significantly exceeded that of the previous high-temperature record for phonon-mediated superconductivity: 33 K in  $\text{Cs}_x\text{Rb}_y\text{C}_{60}$  [145]. The current record holder for high-temperature, phonon-mediated superconductivity ( $\text{MgB}_2$ ) can certainly be called a low- $Z$  compound.

In 1999, Neaton and Aschroft [146] predicted that Li, the prototypical free-electron metal at ambient pressure and the lightest of the elemental metals, ought to depart radically from free-electron behavior at high pressure. In particular, they suggested that, under pressure, Li would adopt lower symmetry crystal structures and experience band *narrowing*, both contrary to conventional expectation. These effects can largely be attributed to the exclusion of the conduction electrons from the atomic cores. We note that Ca, the current record holder for high- $T_c$  in an element, also experiences a similar band narrowing under pressure [139]. In 1986, Lin and Dunn [147] had tentatively suggested that Li became superconducting under pressures of 20-30 GPa. Superconductivity in Li was finally confirmed in 2002, first by Shimizu *et al.* [122], then by Struzhkin *et al.* [148] and then in the first nearly hydrostatic experiments by Deemyad and Schilling [149]. At pressures near 30 GPa,  $T_c$  of Li reached 15-20 K; at the time, this was a record high  $T_c$  for an elemental superconductor. Clearly, a detailed experimental survey of the superconductive properties of low- $Z$  materials is in order.

We have explored two separate approaches to the search for superconductivity in low- $Z$  materials: (1) combine Li, the lightest metal, with other low- $Z$  metals (2) combine hydrogen with other low- $Z$  elements. For approach (1) we have carried out experiments on Li, the alloy  $\text{Li}_{0.9}\text{Mg}_{0.1}$  and the compound  $\text{CaLi}_2$ . For approach (2)

we investigated two complex hydrides,  $\text{LiBH}_4$  and  $\text{LiAlH}_4$ .

#### 4.2.1 Li and Li(Mg) Alloy

Binary intermetallics including Li or the other alkali metals have been far less extensively examined for superconductivity than, for example, transition metal intermetallics. At ambient pressure, alloys of Li and Mg have been found not to superconduct down to  $\sim 3$  K at atomic concentrations of 1, 5 and 10% [150]. Pure Mg appears to remain non-superconducting up to  $\sim 1$  Mbar [151], while, under pressure, Li has one of the highest  $T_c$  values amongst the elements. The binary phase diagram for Li-Mg [152] indicates that Mg is miscible in Li up to 75% atomic percentage. Thus, a useful aspect of an alloying study on these elements is that properties may be investigated across a wide compositional range more or less continuously. How then will the superconducting phase diagram evolve across the compositional range of Li-Mg alloys? One possibility is that the  $T_c$  value of pure Li will rise as one increases the electron density through alloying divalent Mg into the monovalent Li. Therefore, we undertook to explore how the superconducting phase diagram evolves in alloys of Li and Mg as one gradually increases the concentration of Mg. These studies are in their early stages and here we describe the results of experiments on pure Li and a single composition,  $\text{Li}_{0.9}\text{Mg}_{0.1}$ .

#### Lithium

The first experiment carried out during the course of this dissertation research was a hydrostatic (helium pressure medium) experiment on pure lithium metal. The experiment utilized diamonds with 0.5 mm culets, and a Re gasket preindented to  $\sim 70 \mu\text{m}$ . At pressures of 22.8, 23.7, 25.2, 27.8 and 30.7 GPa the field dependence of  $T_c$  was measured at fields up to 500 Oe. Pressure was determined using the ruby fluorescence manometer.

Figure 4.14 shows  $T_c$  versus pressure for the present experiment (solid circles) compared with the earlier work of Reference [149]. The complex behavior of  $T_c$  under pressure has been attributed to structural phase transitions. The onset of superconductivity near 20 GPa is likely due to the transition from the Rh6 to the

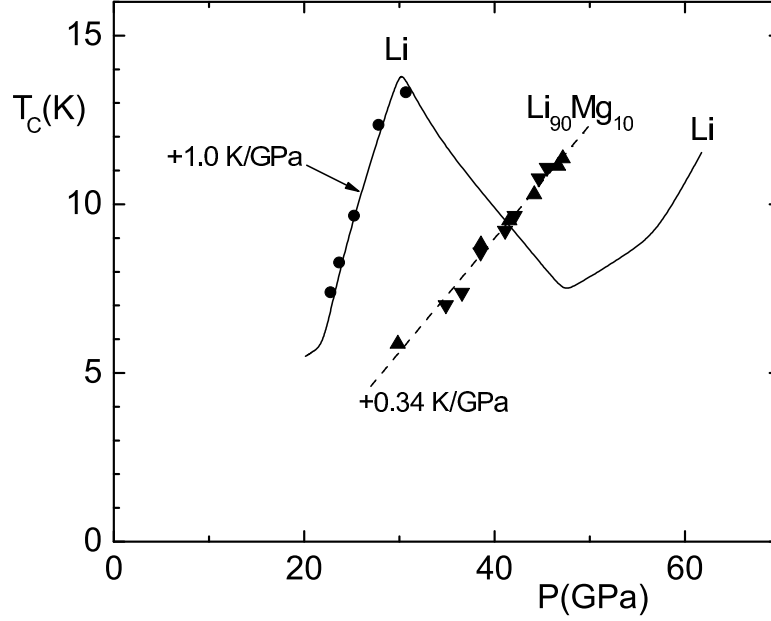


Figure 4.14:  $T_c$  versus pressure for pure Li and  $\text{Li}_{0.9}\text{Mg}_{0.1}$ . Solid line represents the original hydrostatic data on Li from Reference [149]. Dashed line is a linear fit of the  $\text{Li}_{0.9}\text{Mg}_{0.1}$  data.

fcc structure [122, 147, 148]. After rising steeply to  $\sim 14$  K at 30 GPa,  $T_c$  abruptly begins to drop sharply with pressure. This change in dependence has been tentatively suggested [149] to be due to the transition from the fcc to CI16 structure [38]. At present, whether the broad minimum in  $T_c$  near 50 GPa or the sudden disappearance of superconductivity above 62 GPa are due to additional structural phase transitions is unknown. The primary motivation for this experiment was to study the field dependence of  $T_c$  to higher fields than previous work, in order to gain more information about the nature of the various features in the superconducting phase diagram.

Figure 4.15 (left) shows  $H_c$  versus  $T$  for each pressure. The curves are fit using Equation 2.4 and extrapolated to zero temperature. Figure 4.15 (right) shows the initial slope of  $(dH_c/dT)_{T_c}$  versus pressure. Note that the initial slope versus pressure is fit almost perfectly by a quadratic. The earlier data of Reference [149] (solid diamonds) which extends to somewhat higher pressure appears to exhibit a change in behavior above 32 GPa. Note that this is near the same pressure where  $T_c$  passes through a maximum. According to Equations 2.5 and 2.6 a quadratic increase in  $(dH_c/dT)_{T_c}$  under pressure would indicate a rapid increase in  $N(E_F)$  with pressure.

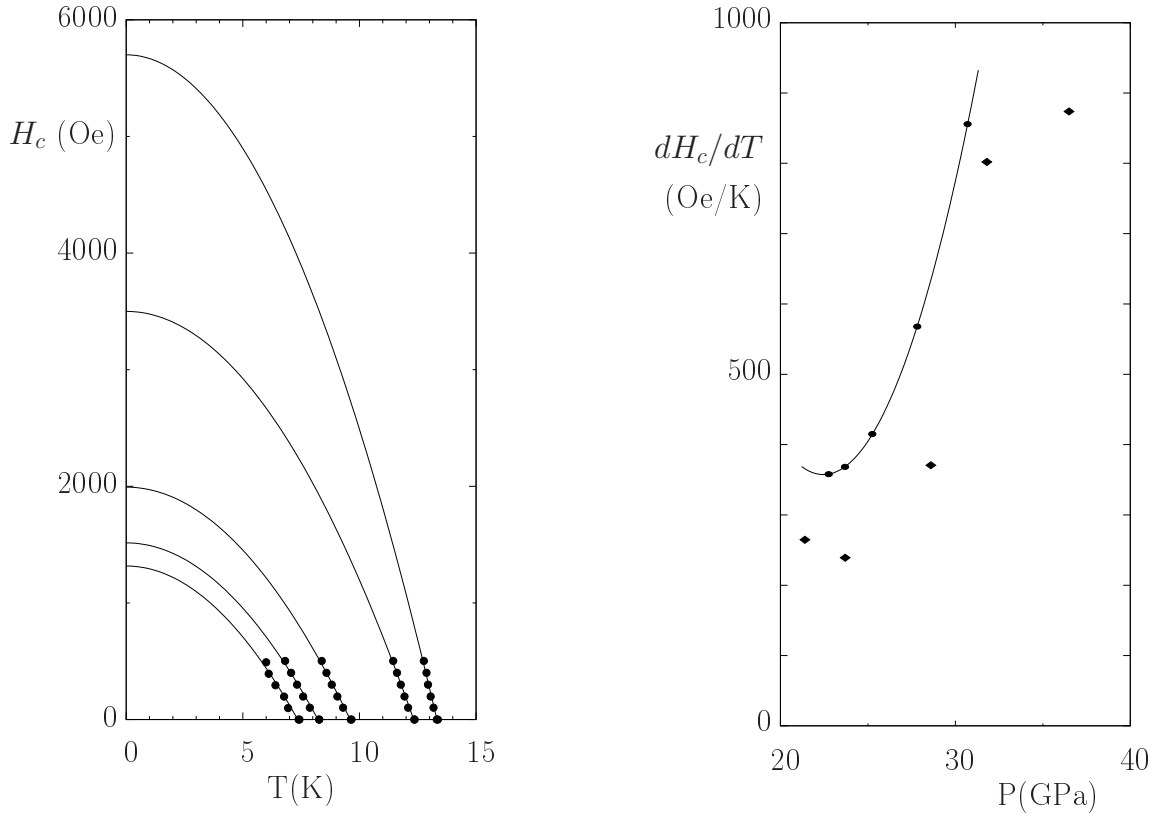


Figure 4.15: Magnetic field dependence of  $T_c$  in pure Li under pressure. (left) Critical field versus temperature at 22.8, 23.7, 25.2, 27.8 and 30.7 GPa (from left to right across the curves). Solid curves represent fits of the data using Equation 2.4. (right) Slope  $(dH_c/dT)_{T_c}$  versus pressure. Data of present work is given by solid circles and is nearly perfectly fit by a quadratic. Previous data of Reference [149] is given by solid diamonds and shows a similar pressure dependence in the region below 35 GPa.

Because the superconductivity in Li is not in the weak coupling limit, the exact dependence of  $N(E_F)$  on pressure suggested by these equations cannot be taken literally, but a rapid increase in the density of states with pressure seems likely. At low pressure, the estimated values of  $H_c(0)$  are comparable with those found for type I simple metal superconductors like Pb ( $H_c(0) \sim 780$  Oe) while, the higher values of  $H_c(0)$  at higher pressures seem to indicate a crossover to type II behavior. Further experiments are recommended, both to carry the field dependence measurements through the entire superconducting phase diagram and in order to investigate the possibility that superconductivity may reappear at much higher pressure.

### Li(Mg) Alloy

A sample of  $\text{Li}_{0.9}\text{Mg}_{0.1}$  was prepared by M. Debessai by dissolving Mg pellets into molten Li in a tantalum-foil-lined stainless steel crucible. The melt was stirred with a tantalum rod for  $\sim 30$  minutes at a temperature of near  $230^\circ\text{C}$ . A single hydrostatic helium pressure medium experiment was performed, reaching a maximum pressure of 47 GPa. The sample was roughly a square  $56\ \mu\text{m}$  on a side by  $15\ \mu\text{m}$  thick leading to an expected transition size of not more than 10 nV. Figure 4.16 shows several of the transitions from this experiment. The transitions are  $\sim 3$  nV in magnitude. Either the sample became deformed through contact with the cell walls under pressure, leading to a smaller demagnetization factor or, poor sample connectivity lead to less than 100% shielding. In Figure 4.14 the upward pointing triangles give  $T_c$  versus pressure for loading and the downward pointing triangles give the dependence on unloading. The  $\text{Li}_{0.9}\text{Mg}_{0.1}$  sample exhibits a significantly reduced initial slope  $dT_c/dP$  relative to that of pure Li.

It is well known that the sequence of crystal structures in sp metals can be related to the interaction of the Fermi surface with the Brillouin zone [153–156]. Structural transitions occur as the Fermi surface is brought into contact with the Brillouin zone boundary either through pressure or alloying. The Fermi surface is expected to expand as electron concentration increases through alloying divalent Mg into the monovalent Li. This should have an influence of the critical pressures for the structural transitions. Thus, in Li-Mg alloys, it may be possible to stabilize the fcc phase

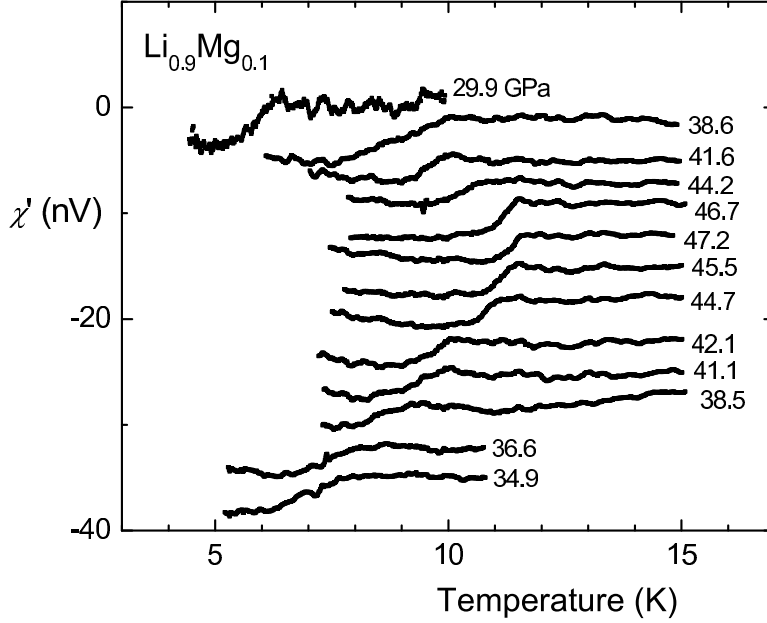


Figure 4.16: Ac susceptibility versus temperature for  $\text{Li}_{0.9}\text{Mg}_{0.1}$  at several pressures for both loading and unloading. The curves were measured in the order shown from top to bottom.

at ambient pressure. Since the onset of superconductivity in Li is believed to be associated with the transition to the fcc structure, stabilizing the fcc phase at ambient pressure could lead to ambient pressure superconductivity in Li-Mg. The data for the single alloy we have thus far studied do not extend to low enough pressure to allow a reliable estimate of the critical pressure for the onset of superconductivity. Future work at higher Mg concentration will determine if this simple picture is born-out by experiment and may also help to answer the question of why Mg appears to remain non-superconducting to such high pressures.

#### 4.2.2 $\text{CaLi}_2$ Compound

Recently, Feng *et al.* [157] predicted that like Li, the properties of  $\text{CaLi}_2$  should become highly anomalous under pressure and that a high  $N(E_F)$  combined with the low mass of Li might lead to superconductivity with significant  $T_c$ . Up until the present work, there appears to have been no examination of  $\text{CaLi}_2$  for possible superconductivity, even at ambient pressure. We therefore set out to determine if

$\text{CaLi}_2$  becomes superconducting at either ambient or high pressure.

Several high pressure experiments were carried out on polycrystalline  $\text{CaLi}_2$  samples. All samples were prepared by M. Debessai. The starting materials for syndisertation of  $\text{CaLi}_2$  were pieces of Ca from Alpha Aesar with stated purity 99.98% (metals basis) and Li rod 99.99% (metals basis) from ESPI Metals. The first sample (so-called “unannealed”) was prepared by dissolving stoichiometric amounts of Ca into molten Li. The melt was contained in a tantalum-foil-lined stainless steel crucible, heated with a hotplate to a temperature of approximately 235 °C, and stirred with a tantalum rod for approximately 30 minutes. The resulting material is a shiny, silver-colored metal that, in contrast to pure Li, is quite brittle. X-ray diffraction experiments performed by M. Debessai confirm the hexagonal crystal structure as given by Reference [158]. At ambient pressure, no superconducting transition could be detected down to 2 K in the resistivity and down to 1.10 K in an ac magnetic susceptibility experiment (performed by M. Debessai) that would have been able to detect superconductivity with shielding fraction of  $\sim 0.1\%$ .

Takahiro Matsuoka prepared a DAC for 4-point resistivity measurements. The sample size was approximately 100  $\mu\text{m}$  diameter by 10  $\mu\text{m}$  thick. The voltage leads were 20-30  $\mu\text{m}$  apart. Details of the resistivity technique are described in Section 3.7. After initially increasing pressure at room temperature, the cell was kept below 200 K in order to prevent any reaction between the sample and the cell. Pressure was increased monotonically, eventually reaching a maximum pressure of 81 GPa and then reduced to 45 and 26 GPa. Pressure was determined using the ruby manometer. At each pressure, the resistance was measured down to a temperature of 1.6 K.

The resistance versus temperature for each pressure is shown in Figure 4.17. Because the exact geometry of the sample is difficult to estimate accurately, we have plotted resistance rather than resistivity versus pressure. For the moment we focus on the normal state behavior of the resistance (the superconducting transitions are more clearly presented in Figure 4.18). The normal state resistance at low temperature (15 K) is observed to increase rapidly with pressure being roughly ten times greater at 81 GPa than at 8 GPa. That this rapid increase in the low temperature resistance is intrinsic to the material, and not merely due to the introduction of lattice defects

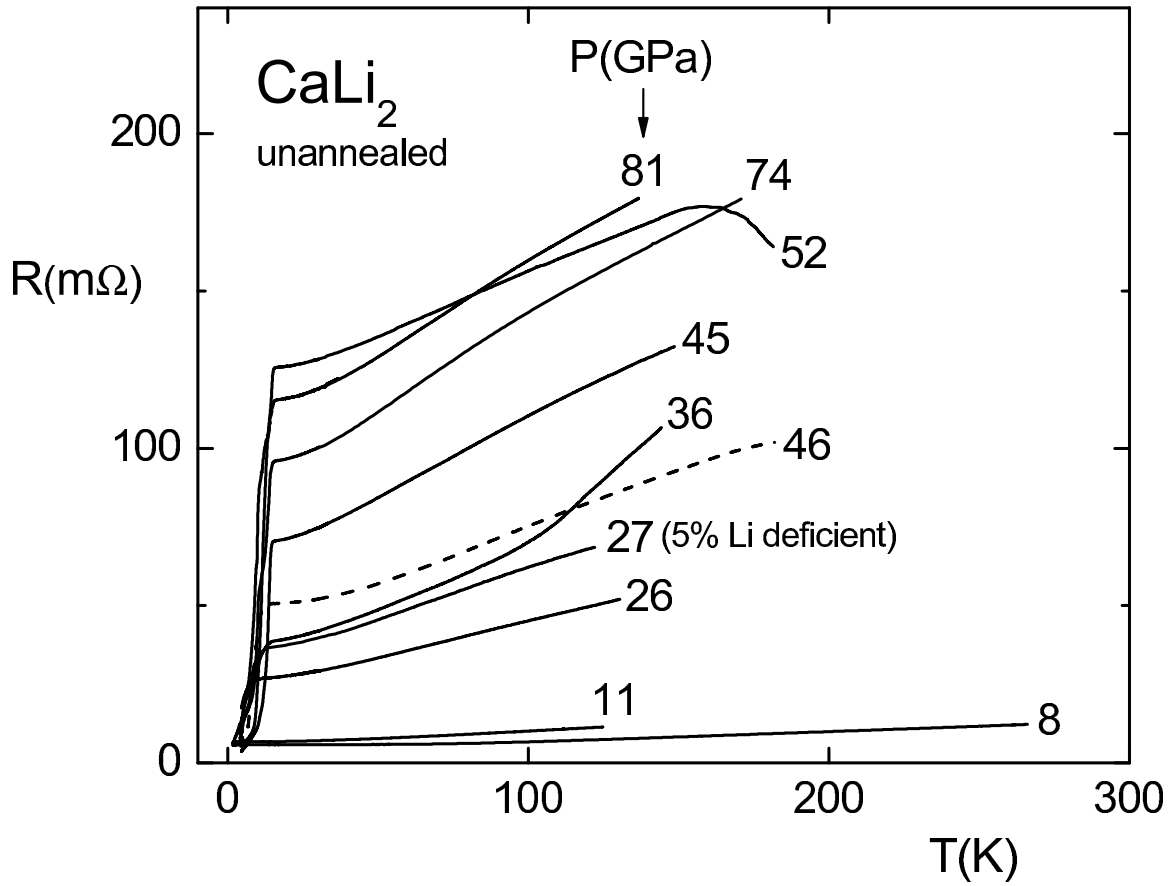


Figure 4.17: Resistance versus pressure for  $CaLi_2$  measured at 8, 11, 26, 36, 45, 52, 74, 81 and 46 GPa (in that order). The dashed line indicates that data was taken on pressure release. The normal state resistance at low temperature increases by roughly an order of magnitude between 8 and 81 GPa.

as the sample deforms under non-hydrostatic pressure, is demonstrated by the fact that the resistance drops back down when the pressure is reduced from 81 GPa to 46 GPa (dashed curve). An additional experiment performed by M. Debessai to 0.76 GPa in hydrostatic helium pressure medium found that the room temperature resistivity increased at a rate of  $\sim 13\%/GPa$ . Such a large increase in the resistivity with pressure is anomalous; in simple metals, one generally expects resistivity to decrease under pressure as the Debye temperature increases.

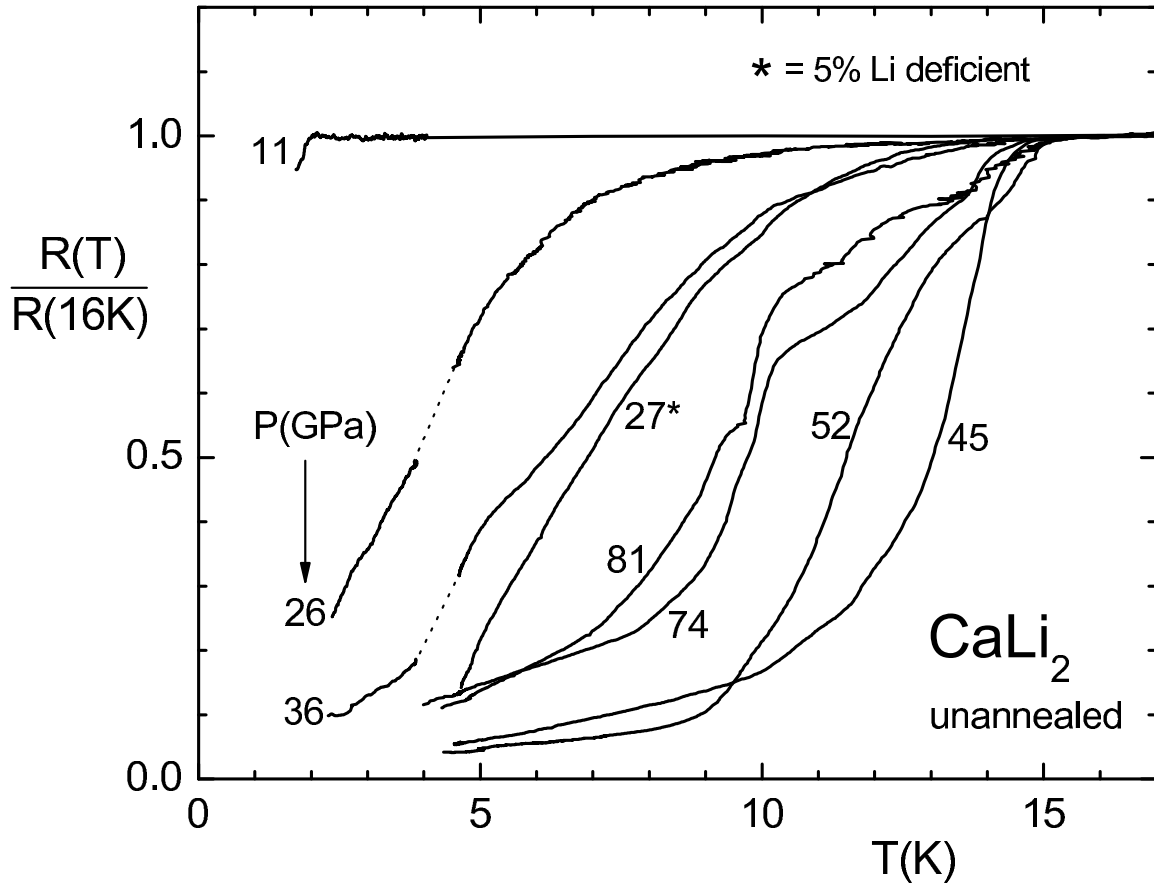


Figure 4.18: Resistance versus pressure normalized to the resistance at 16 K for  $CaLi_2$ . The dashed lines are guides to the eye to bridge gaps in the data.

Figure 4.18 highlights the superconductive transitions by plotting resistance, normalized to the resistance at 16 K, versus temperature for each pressure. A small drop in the resistance near 2 K at 11 GPa was the first sign of a superconducting transition. Upon increasing pressure the transition moves to higher temperature and it can be

seen that at the lowest temperatures the resistivity drops nearly to zero, indicating that this is indeed a superconducting transition. Subsequent measurements by M. Debessai at fields up to 500 Oe confirmed that the transition indeed shifts downward with applied field at an initial ( $T \sim T_c$ ) rate of  $\sim 0.3$  mK/Oe, consistent with type II superconductivity.

Figure 4.19 shows the pressure dependence of the critical temperature. The points are determined from the temperature at which the resistance drops to 50% of the normal state value. The vertical error bars are determined by the 20-80% transition width. Horizontal error bars are determined by the full width at half maximum (FWHM) of the ruby line. Note that because of the highly nonhydrostatic conditions present in a resistivity measurement such as this one, the uncertainty in the pressure (estimated from the width of the ruby line) reaches  $\pm 12$  GPa at the highest pressure.

The pressure dependence shown in Figure 4.19 appears rather similar to that observed for pure Li under hydrostatic pressure (Figure 4.14). That the peak in  $T_c$  occurs near 30 GPa for pure Li and 40 GPa for  $\text{CaLi}_2$  is not significant due to the uncertainty in the pressure determination for the  $\text{CaLi}_2$  experiment. This raises the question whether the superconductivity observed in  $\text{CaLi}_2$  might be a filamentary effect arising from residual pure Li in the sample, perhaps percolating through grain boundaries. In order to reduce the possibility of residual, unreacted, pure Li in the sample, we prepared a sample 5% deficient in Li. An additional high pressure experiment was performed on this sample at a single pressure of 27 GPa. The results for the 5% Li deficient sample shown in Figures 4.17, 4.18 and 4.19 show that the superconductivity remains and is consistent with the results for the stoichiometric sample, lending support to bulk  $\text{CaLi}_2$  as the source of the superconductivity. The rather small shift in  $T_c$  under applied field also suggests a bulk effect since filamentary superconductivity is usually rapidly suppressed by magnetic field.

I performed a total of five separate susceptibility experiments on  $\text{CaLi}_2$  at pressures as high as 50 GPa. Both the “unannealed” and the 5% deficient sample were tested. All five experiments failed to detect any superconducting transition. Four of these tests employed helium pressure medium. The fifth measurement was non-hydrostatic, using no pressure medium in order to test whether the superconductivity might be

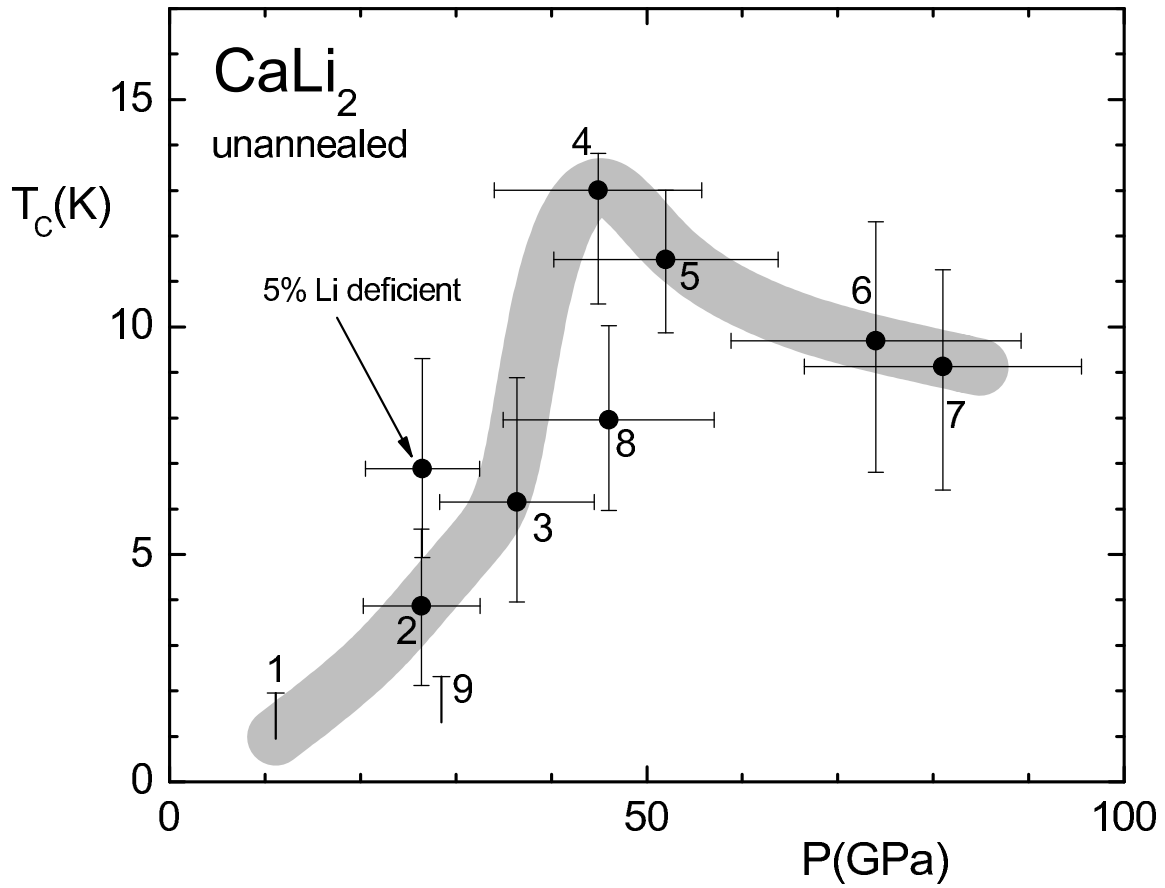


Figure 4.19:  $T_c$  versus pressure for  $\text{CaLi}_2$ . Values of  $T_c$  are determined from the midpoint of the resistive transition. Vertical error bars are determined by the 20-80% transition width. Horizontal error bars are determined by the FWHM of the ruby fluorescence line. The thick grey line is a guide to the eye. Numbers give order of measurement.

strain induced. The inability to observe transitions in the susceptibility could point towards superconductivity of a filamentary nature but it could also be the result of poor sample connectivity leading to a small shielding effect. The size of the samples for these susceptibility studies would lead to transitions not more than 10-20 nV in magnitude. If the sample were poorly connected or the transition very broad in temperature, the transition size could be reduced below the detection limit (see Figure 3.28).

Further details of our extensive measurements on this material are reported in Reference [159]. At present it still remains unresolved whether the superconductivity is a bulk effect due to  $\text{CaLi}_2$  or a percolative, filamentary effect due to unreacted pure Li. This could be resolved through single crystal studies or heat capacity measurements. Heat capacity has the advantage of providing a true signature of bulk superconductivity unlike resistivity which is sensitive to percolative effects and ac magnetic susceptibility which measures shielding currents that only flow on the surface of the sample.

### 4.2.3 Complex Hydrides: $\text{LiBH}_4$ and $\text{LiAlH}_4$

Despite the fact that hydrogen has been compressed to the enormous pressure of 342 GPa [160], it has yet to turn metallic, leaving the question of high-temperature superconductivity in metallic hydrogen unresolved. An alternative and complementary approach to ultra-high pressure is that of *chemical pre-compression*. A similar approach was used by Chu *et al.* [8] when they shrunk the lattice of LBCO by substituting smaller and isoelectronic Y for La (see Chapter 1). By combining hydrogen with other elements, it may be possible to create conditions similar to those expected for solid metallic hydrogen but at much lower pressures. Ashcroft [59, 161, 162] has highlighted primarily covalent hydrides, like  $\text{CH}_4$ ,  $\text{SiH}_4$ ,  $\text{GeH}_4$  or  $\text{PbH}_4$ , as promising substitutes for metallic hydrogen. When we speak of precompression in these systems, it is important to note that what is being precompressed is *not* the hydrogen atoms themselves; rather, one hopes, through chemistry, to modify the electronic structure in such a way as to reduce the required metallization pressure. As an example, in the solid state, methane has a significantly lower density of hydrogen atoms than pure

hydrogen. However the valence electron density of methane at 38 GPa is already equal to that of hydrogen at 150 GPa [161]. Yet, while these systems are predicted to metallize at pressures lower than that for hydrogen, the metallization pressures are still enormous. For methane, the Goldhammer-Herzfeld criterion (see Section 2.4.2) predicts metallization near 300 GPa while more sophisticated calculations predict no metallization at pressures as high as 500 GPa [163]; these pressures are at, or beyond, the limit of current static high pressure technology. Finally, due to a lack of strong intermolecular forces between the covalently bonded molecular units, hydrides of the type mentioned above generally have low melting points and are highly volatile [164]. Therefore, loading these materials into the sample chamber of a DAC presents some (not insurmountable) difficulties. Another possible route to a metallic hydrogen substitute at significantly lower pressure might be through the ternary hydrides.

We performed high pressure experiments on the two ternary, complex hydrides,  $\text{LiBH}_4$  and  $\text{LiAlH}_4$ . These materials have attracted interest as potential hydrogen storage materials due to their high weight percentage of hydrogen. At ambient pressure,  $\text{LiBH}_4$  [165] and  $\text{LiAlH}_4$  [166] crystallize with orthorhombic and monoclinic symmetry, respectively, each with four formula units per cell. Their structures are characterized by  $\text{Li}^+$  cations well separated from  $(\text{MH}_4)^-$  anions where M is B or Al. The  $(\text{MH}_4)^-$  subunits consist of four hydrogen atoms arranged around the M atom in a nearly regular tetrahedron. These compounds belong to a more general class of hydrides that display both ionic and covalent bonding within the same material; within the  $(\text{MH}_4)^-$  subunits the bonding is primarily covalent while, the bonding between the  $\text{Li}^+$  cations and  $(\text{MH}_4)^-$  anions is essentially ionic [167]. Both materials are indirect, wide-gap insulators with gaps of  $\sim 5$  eV. In an ideal ionic substance, one expects that the valence and conduction bands should be formed predominantly from the anion and cation wavefunctions, respectively [45]. Indeed, one finds this expectation met in  $\text{LiMH}_4$  where the valence band has primarily M and H character and the conduction band has primarily Li character [167]. Neither material has yet been reported to undergo a metal insulator transition under pressure.  $\text{LiAlH}_4$  has been predicted not to metallize at pressures up to 40 GPa [166]. Estimates of the metallization density using the Goldhammer-Herzfeld criterion are precluded by a lack

of data on polarizability. For organic compounds tables exist which allow estimates of the total polarizability by summing empirically estimated “bond polarizabilities”. There appear to be no such tables which would allow simple estimates of the polarizabilities of  $\text{LiBH}_4$  or  $\text{LiAlH}_4$ . However, one can say that  $\text{LiAlH}_4$  ought to be more polarizable than  $\text{LiBH}_4$ , due to the larger size of Al relative to B. Thus one would expect  $\text{LiAlH}_4$  to metallize at lower molar density than  $\text{LiBH}_4$ .

Both  $\text{LiBH}_4$  and  $\text{LiAlH}_4$  are readily available, and reasonably stable at room temperature<sup>6</sup>. The samples were obtained from the Alfa Aesar Company and used as received with stated purities of 95% for both  $\text{LiBH}_4$  and  $\text{LiAlH}_4$ . The  $\text{LiAlH}_4$  is received as grey colored pellets which, when crushed, yield small (100-500  $\mu\text{m}$ ) clear fragments. Some of the fragments appear to be contaminated with trace aluminum metal; these fragments are not selected for loading into the DAC. Both materials are air sensitive, so all samples were loaded into the DAC inside of the argon-filled glovebox. In an initial pair of experiments, the samples were loaded, along with about 3 ruby spheres (5-10  $\mu\text{m}$  diameter), into rhenium gaskets preindented with 0.5 mm diameter diamond culets. For  $\text{LiBH}_4$ , the sample was compressed up to 53 GPa. The only measurement on this sample was a visual one; white light illuminated the sample and the color of the transmitted light was observed (Appendix C describes the experimental arrangement).

Visual observation of the color of light transmitted through a sample under white light illumination is the simplest method for observing a band overlap transition from wide gap to metallic character. Photons below the band gap energy pass unimpeded through the material while photons with energy higher than the band gap energy are absorbed. Therefore, as the gap energy is reduced through the visible range, first the highest energy (blue) photons are absorbed and the sample turns yellow. Further reduction of the band gap leads to absorption of progressively lower energy photons, turning the sample orange, dark orange, red and eventually black. Note that even when the sample turns black, there still may be a substantial band gap  $\lesssim 1.8$  eV. For direct gap materials, the transmission spectrum should show a sharp edge at the band gap energy (with very small transmission at energies higher than the band gap

---

<sup>6</sup> $\text{LiAlH}_4$  is known to decompose spontaneously at room temperature but decomposition is slow enough that it does not cause problems for loading the sample into the DAC.

energy). In an indirect gap material, this edge is thermally broadened and it becomes more difficult to pinpoint the exact value of the band gap.

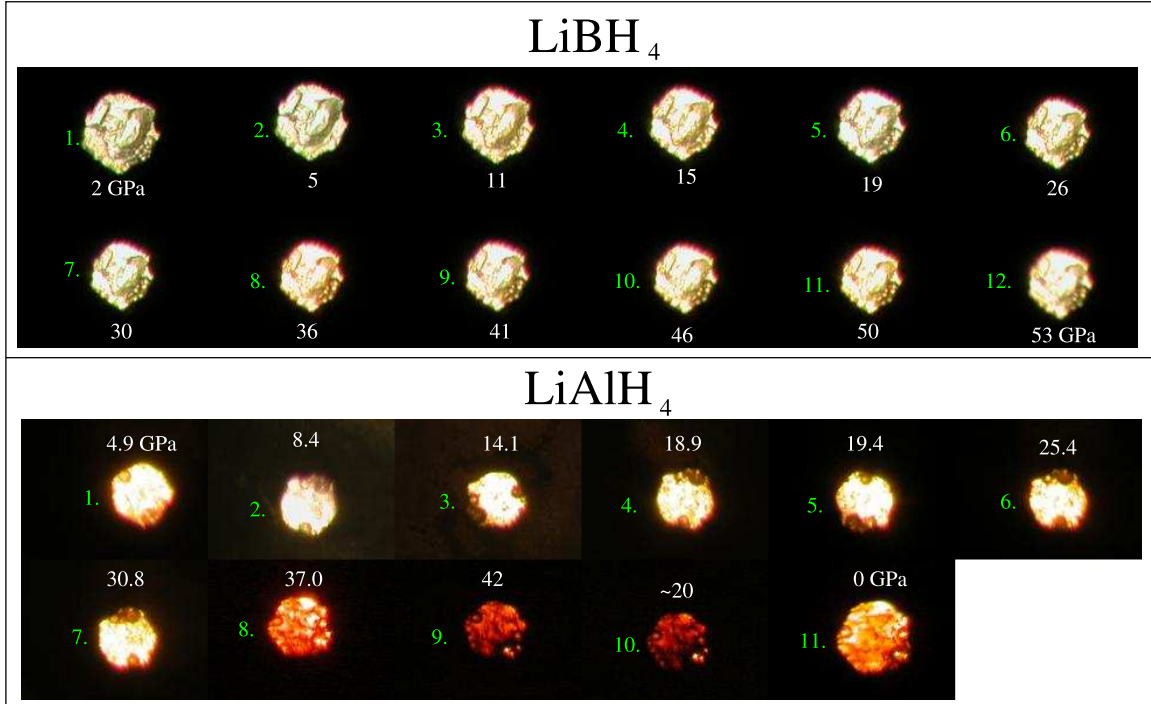


Figure 4.20: Transmitted light photographs for two of the high pressure experiments on complex hydrides.  $\text{LiBH}_4$  shows no color change up to a pressure of 53 GPa.  $\text{LiAlH}_4$  begins to turn orange near 37 GPa indicating a reduction in the band gap.

The  $\text{LiBH}_4$  sample was not observed to change color up to 53 GPa (see top of Figure 4.20). We performed a similar experiment on  $\text{LiAlH}_4$  up to a maximum pressure of 42 GPa. As Figure 4.20 clearly shows, between 30 and 37 GPa the sample turns orange, becoming progressively darker orange as the sample is further compressed to 42 GPa. Upon releasing back to ambient pressure, some of the orange color remains, possibly indicating that the color change is due to a structural phase transition which displays hysteresis on pressure release.

For  $\text{LiAlH}_4$ , in addition to the visual observation, we also performed optical absorption measurements in the range of photon energies between  $\sim 0.25 - 5$  eV. The infrared range was measured in the laboratory of Dr. A. M. Hofmeister using the Fourier transform infrared spectrometer described in Section 3.5.3 and the visible range was measured using the setup described in Appendix C. Figure 4.21 shows the

results of these measurements. The strong absorption below  $\sim 0.5$  eV is likely due to an overtone of an Al-H stretching mode for the  $(\text{AlH}_4)^-$  tetrahedra<sup>7</sup>. The region above 0.5 eV is where we see the effects of band gap closure. Because  $\text{LiAlH}_4$  is an indirect gap material and these studies are carried out at room temperature, one does not expect to observe a sharp edge in the transmission spectrum. However, Figure 4.21 clearly shows a suppression of the transmission progressively lower photon energies as pressure is increased, in line with the expectation for a pressure induced reduction in the band gap. Figure 4.21 (b) shows the data plotted on a log scale to highlight the fact that the transmission continues to drop rapidly at higher photon energy. During the initial experiment we did not measure the transmission at zero pressure. Therefore, after releasing the pressure on the first sample, I removed the sample from the gasket and reloaded the gasket with another sample for a measurement at ambient pressure. This sample, labeled “second sample” in Figure 4.21, had the same thickness as the first sample and so the results should be comparable.

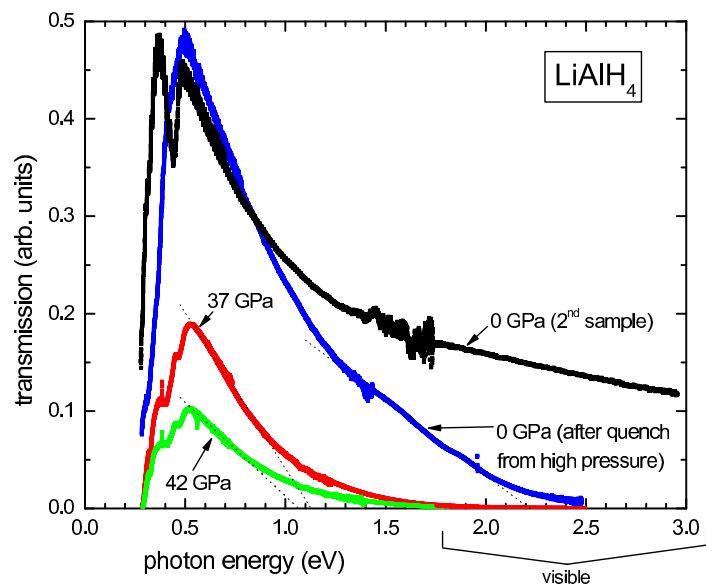
In Figure 4.21 (a) the dashed lines indicate a crude estimation of the band gap energy by extrapolating the curves to zero transmission. Clearly, the results using this method depend somewhat on the region over which the curve is fit. A similar method of estimating the gap appeared to give reasonable results in Reference [169]. A complete characterization of the optical properties would require reflectivity measurements in addition to transmission [170]. The fit for the zero pressure (“2<sup>nd</sup> sample”) was over the data above 2 eV and is not shown in the plot. This method gives gaps of 5.5, 1.12, 1.08, and 2.4 eV for zero pressure (“2<sup>nd</sup> sample”), 37 GPa, 42 GPa and zero pressure (“quenched”), respectively. Note that the 5.5 eV gap at ambient pressure is in reasonable agreement with theoretical predictions [166,167]. The gap at 42 GPa is well below the range of visible light, yet, the sample appears dark orange at this pressure; we attribute this to the broadened absorption edge due to the indirect nature of the gap. Between ambient and 42 GPa the gap closes by  $\sim 4.4$  eV; extrapolating this trend indicates band overlap near 52 GPa. However, in a subsequent experiment, we observed no further change in the color of the sample up to a pressure of 75 GPa, lending support to the notion that the color change occurred at a structural phase

---

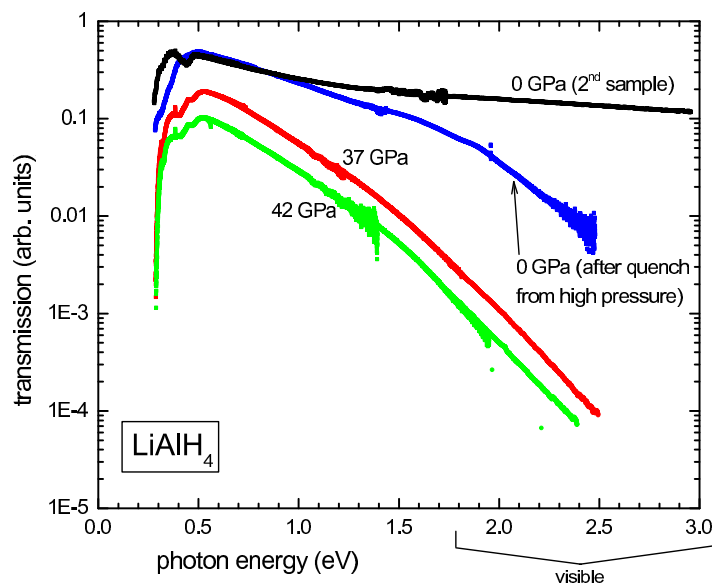
<sup>7</sup>Reference [168] lists vibrational frequencies for  $(\text{AlH}_4)^-$  tetrahedra. The largest of these frequencies is  $1757 \text{ cm}^{-1} = 0.22 \text{ eV}$ . An overtone of this mode would appear at twice the energy, 0.44 eV.

transition. A structural phase transition has been predicted to occur in  $\text{LiAlH}_4$  near 34 GPa [166].

Several possibilities exist for future studies in this direction. One could attempt to further lower the metallization density by substituting larger and more polarizable atoms for M in  $\text{LiMH}_4$  (M = B, Al, Ga, In, and Tl). Thus, perhaps  $\text{LiTlH}_4$  should be examined. Appendix A lists the R/V ratio for several materials. The substituted methane compound  $\text{CH}_2\text{Br}_2$  has the largest R/V ratio of the compounds examined; perhaps it too should be examined for a pressure-induced insulator to metal transition.



(a)



(b)

Figure 4.21: (a) Transmission versus photon energy for  $\text{LiAlH}_4$  at several pressures. Dotted lines indicate linear extrapolations to zero transmission; providing an estimate of the band gap. (b) Log of Transmission versus photon energy.

# Chapter 5

## Summary

- The d-electron metals Sc, Y, and Lu have been studied up to pressures of 74, 115, and 174 GPa, respectively. The  $T_c$  for Y reaches the exceptionally high value of 20 K (ac magnetic susceptibility onset) at 115 GPa. While the  $T_c$  of Y appears to saturate near 115 GPa, the  $T_c$  for Sc and Lu continues increase up to the highest pressure studied in this work. The superconductivity of all three of these metals is consistent with moderately strong-coupled, phonon-mediated superconductivity. For the non-magnetic, trivalent rare-earth series Sc, Y, La, and Lu there appears to be some correlation between  $T_c$  and  $R_{WS}/R_c$ , the ratio of the Wigner-Seitz radius to the ion core radius, which provides a measure of the d-electron occupation,  $N_d$ . A single experiment found some evidence for superconductivity in Eu metal near 4 K and 80 GPa; but this has yet to be verified.
- While one might expect that the  $T_c$  of Li would increase upon alloying divalent Mg into the monovalent Li, we find that, in an alloy  $\text{Li}_{0.90}\text{Mg}_{0.10}$ , the initial slope of  $T_c$  versus pressure is suppressed by a factor of 3 relative to that of pure Li. A detailed understanding of this behavior awaits further studies at increased Mg concentration and higher pressure. In the compound  $\text{CaLi}_2$  we find no evidence for superconductivity down to 1.1 K at ambient pressure. In high pressure resistivity measurements on  $\text{CaLi}_2$ , we observe a superconducting transition appearing at 2 K and 11 GPa, increasing to 13 K at 45 GPa and then

decreasing to 9 K at 81 GPa. Several ac magnetic susceptibility experiments on  $\text{CaLi}_2$  failed to detect any signature of superconductivity. Whether  $\text{CaLi}_2$  displays bulk superconductivity under pressure is still open to question.

- A search for a pressure-induced insulator to metal transition in a hydrogen rich, low-Z compound lead us to examine the two complex hydrides,  $\text{LiBH}_4$  and  $\text{LiAlH}_4$  to pressures of 52 and 75 GPa respectively. In  $\text{LiBH}_4$  we find no evidence of band gap closure. However, in  $\text{LiAlH}_4$  we observe that the sample turns orange near 35 GPa suggesting a reduction in the band gap. Infrared absorption measurements on  $\text{LiAlH}_4$  at high pressure indicate a closure in the band gap from  $\sim 5.5$  eV at ambient pressure to  $\sim 1.1$  eV at 42 GPa. A study to higher pressure indicates no further color change up to 75 GPa, suggesting a sudden change in band gap near 35 GPa, perhaps related to a structural phase transition.
- The sensitivity of our ruby fluorescence manometer has been significantly enhanced and the diamond vibron manometer has been demonstrated at pressures as high as 174 GPa. These improvements make it possible to routinely perform accurate measurements at pressures in excess of 1 Mbar.

# Appendix A

## R/V for Selected Compounds

The list below calculated R/V values for several compounds. Polarizability and molar volume values have been taken mainly from Reference [66]. The compounds are listed in order of decreasing R/V ratio.

R/V	Formula	Name
0.699	CH <sub>2</sub> Br <sub>2</sub>	dibromomethane
0.645	BeH <sub>2</sub>	beryllium hydride
0.571	C <sub>10</sub> H <sub>9</sub> N	beta-naphthylamine
0.538	C <sub>14</sub> H <sub>10</sub>	Phenanthrene
0.520	C <sub>15</sub> H <sub>21</sub> CrO <sub>6</sub>	chromium acetylacetonate
0.489	C <sub>24</sub> H <sub>12</sub>	coronene
0.485	C <sub>10</sub> H <sub>14</sub> BeO <sub>4</sub>	beryllium acetylacetonate
0.465	C <sub>18</sub> H <sub>12</sub>	chrysene
0.462	CHI <sub>3</sub>	iodoform
0.461	C <sub>14</sub> H <sub>10</sub>	Anthracene
0.449	C <sub>6</sub> H <sub>4</sub> N <sub>2</sub> O <sub>4</sub>	p-dinitrobenzene
0.447	C <sub>16</sub> H <sub>10</sub>	pyrene
0.446	C <sub>6</sub> H <sub>4</sub> O <sub>2</sub>	p-benzoquinone
0.426	C <sub>14</sub> H <sub>8</sub> O <sub>2</sub>	anthraquinone
0.425	C <sub>8</sub> H <sub>4</sub> N <sub>2</sub>	p-dicyanobenzene
0.403	CH <sub>2</sub> I <sub>2</sub>	diiodomethane
0.369	C <sub>2</sub> N <sub>2</sub>	cyanogen
0.367	C <sub>11</sub> H <sub>8</sub> O	1-naphthaldehyde
0.363	C <sub>6</sub> H <sub>5</sub> NO <sub>2</sub>	nitrobenzene
0.361	CH <sub>2</sub> Cl	chloromethane
0.355	C <sub>7</sub> H <sub>7</sub> NO <sub>3</sub>	nitroanisole
0.351	C <sub>10</sub> H <sub>9</sub> N	alpha-naphthylamine
0.351	C <sub>6</sub> H <sub>5</sub> I	iodobenzene
0.350	C <sub>9</sub> H <sub>7</sub> N	isoquinoline
0.349	C <sub>11</sub> H <sub>8</sub> O	2-naphthaldehyde
0.348	C <sub>10</sub> H <sub>9</sub> N	2-methylquinoline
0.347	C <sub>10</sub> H <sub>9</sub> N	1-methylisoquinoline
0.346	CH <sub>3</sub> NO <sub>2</sub>	nitromethane
0.345	C <sub>4</sub> H <sub>11</sub> N	butylamine
0.340	C <sub>6</sub> H <sub>12</sub> O <sub>3</sub>	paraldehyde
0.339	CHBr <sub>3</sub>	bromoform
0.338	C <sub>2</sub> H <sub>5</sub> NO <sub>2</sub>	nitroethane
0.337	C <sub>9</sub> H <sub>7</sub> N	quinoline
0.335	C <sub>6</sub> H <sub>7</sub> N	aniline
0.333	C <sub>10</sub> H <sub>8</sub>	Napthalene2
0.332	C <sub>8</sub> H <sub>6</sub> N <sub>2</sub>	quinoxaline
0.331	C <sub>6</sub> H <sub>8</sub> N <sub>2</sub>	phenylhydrazine
0.329	C <sub>8</sub> H <sub>8</sub>	Styrene
0.325	C <sub>6</sub> H <sub>8</sub> N <sub>2</sub>	phenylenediamine
0.324	C <sub>8</sub> H <sub>8</sub> O	acetophenone
0.323	CH <sub>3</sub> I	iodomethane
0.322	CN <sub>4</sub> O <sub>8</sub>	tetranitromethane

0.320	C <sub>8</sub> H <sub>11</sub> N	N-dimethylaniline	0.272	C <sub>2</sub> H <sub>5</sub> Br	bromoethane
0.320	C <sub>14</sub> H <sub>22</sub>	p-di-tert-butylbenzene	0.271	C <sub>2</sub> H <sub>8</sub> N <sub>2</sub>	ethylene diamine
0.318	C <sub>7</sub> H <sub>10</sub> N <sub>2</sub>	1,1-methylphenylhydrazine	0.270	C <sub>7</sub> H <sub>15</sub> Br	1-bromoheptane
0.318	C <sub>7</sub> H <sub>9</sub> NO	o-anisidine	0.269	C <sub>2</sub> H <sub>7</sub> N	ethyl amine
0.314	C <sub>6</sub> H <sub>6</sub> O	phenol	0.268	CH <sub>3</sub> Br	bromomethane
0.313	C <sub>10</sub> H <sub>8</sub>	Napthalene1	0.268	C <sub>18</sub> H <sub>37</sub> Br	bromooctadecane
0.312	C <sub>8</sub> H <sub>10</sub>	o-xylene	0.267	C <sub>2</sub> H <sub>3</sub> Br	bromoethene
0.312	C <sub>2</sub> H <sub>4</sub> Br <sub>2</sub>	1,2-dibromoethane	0.267	C <sub>16</sub> H <sub>33</sub> Br	bromohexadecane
0.310	C <sub>2</sub> H <sub>3</sub> I	iodoethylene	0.267	CH <sub>3</sub> NO	formamide
0.309	C <sub>4</sub> H <sub>4</sub> S	thiophene	0.266	C <sub>6</sub> H <sub>10</sub>	Cyclohexene
0.309	C <sub>7</sub> H <sub>5</sub> N	benzotrile	0.265	C <sub>4</sub> H <sub>8</sub> O <sub>2</sub>	2-methyl-1,3-dioxolane
0.306	C <sub>3</sub> H <sub>3</sub> N	acrylonitrile	0.264	C <sub>5</sub> H <sub>6</sub>	1,3-cyclopentadiene
0.306	C <sub>8</sub> H <sub>10</sub>	m-xylene1	0.263	C <sub>3</sub> H <sub>2</sub> N <sub>2</sub>	malononitrile
0.304	C <sub>7</sub> H <sub>8</sub> O	anisole	0.262	C <sub>6</sub> H <sub>10</sub>	2,3-dimethyl-1,3-butadiene
0.297	C <sub>5</sub> H <sub>5</sub> N	pyridine	0.262	C <sub>9</sub> H <sub>19</sub> Br	bromononane
0.297	C <sub>8</sub> H <sub>10</sub> O	phenetole	0.261	C <sub>4</sub> H <sub>4</sub> O <sub>2</sub>	diketene
0.296	C <sub>4</sub> H <sub>8</sub> O <sub>2</sub>	1,4-dioxane	0.261	C <sub>4</sub> H <sub>6</sub> O	crotonaldehyde
0.296	C <sub>9</sub> H <sub>10</sub> O <sub>2</sub>	ethyl benzoate	0.259	C <sub>6</sub> H <sub>10</sub> O <sub>3</sub>	ethyl acetoacetate
0.294	C <sub>6</sub> H <sub>12</sub> N <sub>2</sub>	dimethylketazine	0.259	C <sub>6</sub> H <sub>13</sub> Br	bromohexane
0.294	C <sub>8</sub> H <sub>12</sub> O <sub>2</sub>	ethyl sorbate	0.259	C <sub>7</sub> H <sub>14</sub>	Methylcyclohexane
0.293	C <sub>4</sub> H <sub>6</sub> S	divinyl sulfide	0.257	C <sub>5</sub> H <sub>8</sub> O <sub>2</sub>	acetyl acetone
0.293	C <sub>8</sub> H <sub>10</sub>	Ethylbenzene	0.257	C <sub>6</sub> H <sub>12</sub>	Cyclohexane1
0.292	C <sub>6</sub> H <sub>6</sub>	Benzene	0.256	C <sub>8</sub> H <sub>18</sub> O	butyl ether
0.292	C <sub>7</sub> H <sub>8</sub>	Toluene1	0.255	C <sub>2</sub> H <sub>5</sub> NO	N-methyl formamide
0.292	C <sub>8</sub> H <sub>10</sub>	m-xylene2	0.255	C <sub>3</sub> H <sub>7</sub> NO	N,N-dimethyl formamide
0.291	C <sub>8</sub> H <sub>10</sub>	m-xylene3	0.255	C <sub>2</sub> H <sub>2</sub> Cl <sub>4</sub>	1,1,2,2-tetrachloroethane
0.291	C <sub>7</sub> H <sub>8</sub>	Toluene2	0.254	C <sub>6</sub> H <sub>12</sub>	Cyclohexane2
0.291	C <sub>2</sub> H <sub>4</sub> BrCl	1-bromo-2-chloroethane	0.253	C <sub>8</sub> H <sub>14</sub> O <sub>4</sub>	diethyl succinate
0.290	C <sub>10</sub> H <sub>14</sub>	t-butylbenzene	0.253	C <sub>3</sub> H <sub>7</sub> NO	N-methyl acetamide
0.289	C <sub>9</sub> H <sub>12</sub>	Isopropylbenzene	0.253	C <sub>7</sub> H <sub>14</sub> O <sub>2</sub>	pentyl acetate
0.289	C <sub>10</sub> H <sub>20</sub>	t-butylcyclohexane	0.253	C <sub>5</sub> H <sub>9</sub> N	valeronitrile
0.288	C <sub>8</sub> H <sub>10</sub>	p-xylene	0.253	C <sub>4</sub> H <sub>10</sub> S	ethyl sulfide
0.284	C <sub>3</sub> H <sub>6</sub> O	allyl alcohol	0.252	C <sub>5</sub> H <sub>8</sub>	isoprene
0.282	C <sub>4</sub> H <sub>6</sub> N <sub>2</sub>	N-methylpyrazole	0.252	C <sub>4</sub> H <sub>4</sub> N <sub>2</sub>	succinonitrile
0.282	C <sub>8</sub> H <sub>16</sub>	Ethylcyclohexane	0.251	C <sub>3</sub> H <sub>6</sub> O <sub>2</sub>	ethyl formate
0.282	C <sub>3</sub> H <sub>9</sub> N	propylamine	0.251	C <sub>9</sub> H <sub>21</sub> N	tripropylamine
0.280	C <sub>6</sub> H <sub>12</sub> O	cyclohexanol	0.250	CH <sub>5</sub> N	methyl amine
0.276	C <sub>9</sub> H <sub>18</sub>	Isopropylcyclo-hexane	0.250	C <sub>5</sub> H <sub>8</sub>	trans-1,3-pentadiene
0.275	C <sub>3</sub> H <sub>4</sub>	Propyne	0.250	C <sub>4</sub> H <sub>6</sub>	1,3-butadiene
0.273	C <sub>6</sub> H <sub>12</sub> O <sub>2</sub>	amyl formate			

0.250	C <sub>2</sub> H <sub>6</sub> S	ethanethiol	0.232	C <sub>3</sub> H <sub>6</sub> O <sub>2</sub>	propionic acid
0.250	C <sub>4</sub> H <sub>8</sub> O <sub>2</sub>	ethyl acetate	0.231	C <sub>5</sub> H <sub>10</sub> O <sub>2</sub>	methyl butanoate
0.249	C <sub>3</sub> H <sub>8</sub> O	2-propanol	0.230	C <sub>6</sub> H <sub>14</sub>	n-hexane
0.248	C <sub>4</sub> H <sub>11</sub> N	diethylamine	0.230	C <sub>4</sub> H <sub>8</sub> O	butanal
0.248	C <sub>4</sub> H <sub>10</sub> O	ethyl ether	0.229	C <sub>2</sub> H <sub>6</sub> O <sub>2</sub> S	dimethyl sulfone
0.247	C <sub>4</sub> H <sub>9</sub> NO <sub>2</sub>	1-nitrobutane	0.228	C <sub>3</sub> H <sub>9</sub> N	isopropylamine
0.247	C <sub>8</sub> H <sub>18</sub>	n-octane	0.228	C <sub>6</sub> H <sub>13</sub> F	fluorohexane
0.246	C <sub>5</sub> H <sub>12</sub> O <sub>4</sub>	tetramethyl orthocarbonate	0.228	C <sub>4</sub> H <sub>8</sub>	1-butene2
0.246	C <sub>7</sub> H <sub>12</sub>	1-heptyne	0.228	C <sub>4</sub> H <sub>8</sub> O	methyl ethyl ketone
0.245	C <sub>5</sub> H <sub>10</sub>	Cyclopentane	0.227	C <sub>5</sub> H <sub>10</sub> O <sub>2</sub>	ethyl propionate
0.245	C <sub>4</sub> H <sub>10</sub> O	1-butanol	0.227	CH <sub>2</sub> O <sub>2</sub>	formic acid
0.244	C <sub>3</sub> H <sub>6</sub> O	propionaldehyde	0.226	C <sub>4</sub> H <sub>7</sub> N	isobutyronitrile
0.244	C <sub>3</sub> H <sub>6</sub>	Cyclopropane	0.226	C <sub>3</sub> H <sub>8</sub> O	1-propanol
0.243	C <sub>4</sub> H <sub>10</sub> O	2-methylpropanol	0.226	C <sub>5</sub> H <sub>12</sub> O	ethyl propyl ether
0.243	C <sub>4</sub> H <sub>7</sub> N	butyronitrile	0.224	C <sub>2</sub> H <sub>4</sub> O	ethylene oxide
0.243	C <sub>2</sub> H <sub>2</sub> ClN	chloroacetonitrile	0.222	C <sub>4</sub> H <sub>10</sub> O	methyl propyl ether
0.243	C <sub>6</sub> H <sub>15</sub> N	triethylamine	0.221	C <sub>3</sub> H <sub>6</sub> O <sub>2</sub>	methyl acetate
0.242	C <sub>2</sub> H <sub>7</sub> N	dimethyl amine	0.221	C <sub>5</sub> H <sub>9</sub> N	22-DMPN
0.242	C <sub>7</sub> H <sub>14</sub> O	2,4-dimethyl-3-pentanone	0.219	C <sub>3</sub> H <sub>8</sub> O <sub>2</sub>	dimethoxymethane
0.242	C <sub>2</sub> H <sub>5</sub> NO	acetamide	0.219	C <sub>5</sub> H <sub>12</sub>	Neopentane
0.241	C <sub>3</sub> H <sub>8</sub> O	ethyl methyl ether	0.219	C <sub>5</sub> H <sub>12</sub>	Pentane
0.240	C <sub>3</sub> H <sub>5</sub> N	propionitrile	0.218	C <sub>3</sub> H <sub>9</sub> N	trimethylamine
0.240	C <sub>3</sub> H <sub>7</sub> NO <sub>2</sub>	nitropropane	0.218	C <sub>3</sub> H <sub>6</sub> O	acetone
0.239	C <sub>6</sub> H <sub>10</sub>	1-hexyne	0.216	C <sub>2</sub> H <sub>3</sub> N	acetonitrile
0.238	C <sub>4</sub> H <sub>6</sub> O <sub>3</sub>	acetic anhydride	0.214	C <sub>4</sub> H <sub>10</sub>	Butane1
0.238	C <sub>3</sub> H <sub>8</sub> O <sub>2</sub>	eth.-glyc.-monomethylether	0.214	C <sub>2</sub> H <sub>6</sub>	Ethane
0.236	C <sub>2</sub> H <sub>2</sub>	Acetylene2	0.213	C <sub>3</sub> H <sub>8</sub>	Propane2
0.236	C <sub>6</sub> H <sub>14</sub> O	propyl ether	0.213	C <sub>4</sub> H <sub>8</sub>	1-butene1
0.236	C <sub>7</sub> H <sub>16</sub>	n-heptane	0.211	C <sub>2</sub> H <sub>5</sub> NO <sub>2</sub>	ethyl nitrate
0.236	C <sub>2</sub> H <sub>3</sub> Cl	chloroethylene	0.211	C <sub>3</sub> H <sub>8</sub>	Propane1
0.236	C <sub>5</sub> H <sub>10</sub> O	diethyl ketone	0.207	CH <sub>4</sub> O	methanol
0.235	C <sub>6</sub> H <sub>15</sub> N	dipropylamine	0.206	C <sub>2</sub> H <sub>4</sub> O	acetaldehyde
0.235	C <sub>5</sub> H <sub>10</sub> O	methyl propyl ketone	0.206	C <sub>4</sub> H <sub>10</sub>	Butane1
0.235	C <sub>4</sub> H <sub>8</sub> O <sub>2</sub>	methyl propionate	0.201	C <sub>6</sub> H <sub>14</sub> O <sub>2</sub>	1,2-diethoxyethane
0.234	C <sub>4</sub> H <sub>6</sub>	1-butyne	0.200	C <sub>2</sub> H <sub>2</sub>	Acetylene1
0.234	C <sub>4</sub> H <sub>8</sub> O <sub>2</sub>	butyric acid	0.195	C <sub>3</sub> H <sub>6</sub>	Propene
0.234	C <sub>5</sub> H <sub>10</sub> O <sub>3</sub>	diethyl carbonate	0.192	CH <sub>2</sub> O	formaldehyde
0.234	C <sub>2</sub> H <sub>6</sub> O	ethanol	0.147	CH <sub>4</sub>	methane
0.233	C <sub>5</sub> H <sub>8</sub>	1-pentyne	0.123	CH <sub>3</sub> F	fluoromethane
0.233	C <sub>6</sub> H <sub>14</sub> O <sub>2</sub>	1,1-diethoxyethane			

## Appendix B

# Overview of the Optical System

Figure B.1 shows an overview of the optical system used for the majority of the experiments reported in this dissertation. Table B.1 gives details on the various optical components shown in Figure B.1. The system is currently capable of fluorescence and visible wavelength optical transmission measurements. Raman spectroscopy is also possible provided that improvements are made in order to achieve the necessary sensitivity. The three basic functions of the system are: (1) view the sample, (2) bring the laser beam to sample and focus it to as small a spot as possible, and (3) capture light from the sample and couple it into the spectrometer. Lenses L1, L2, O1, and E1 form a microscope used for viewing the sample; a method for accurately aligning this part of the system is described in Appendix D. The total magnification of this microscope is the product of the magnifications for each component:  $(f_{L1}/f_{L2}) \cdot M_{O1} \cdot M_{E1} = 200\times$ .

In Figure B.1 the light path of the laser beam is indicated by the solid blue line. An improvement made to the optical system during the course of my dissertation work was the addition of lenses L4 and L5. Prior to the addition of these lenses, the focusing of the laser onto the sample (DAC) was entirely dependent on the distance of L2 from the sample. But L2 is also used for viewing the sample; thus, there was no way to simultaneously focus the viewing optics and the laser onto the sample. Lenses L1 and L2 act as a laser collimator, they are placed a distance slightly more than  $f_{L4} + f_{L5}$  apart so that the slightly diverging laser beam is brought closer to parallelism. Adjustments on the position of lens L4 allow one to fine tune the focusing of the laser in order to achieve the smallest spot size ( $\sim 50 \mu\text{m}$ ) and greatest intensity

at the sample.

The solid red line indicates the path of fluorescence light. Mirror M3 is small enough that it cuts out only a small central portion of the light cone originating from the sample, leading to a  $\sim 15\%$  loss in total intensity. Mirrors M4 and M5 may be toggled into the vertical light path to direct illumination from the Ne calibration source into the spectrometer and to view the sample visually, respectively. Filter F1 blocks the laser's long-wavelength plasma lines from entering the spectrometer and interfering with the fluorescence measurements. Filter F2 blocks the strong scattered laser light from entering the spectrometer and overloading the detector. The detector may be either a Hamamatsu R928 photomultiplier tube (PMT) or CCD detector (Hamamatsu HC236-1007). For CCD operation, aperture A3 is removed. Smaller apertures, A2 and A3 offer increased resolution at the cost of lower sensitivity. Reference [171] describes the operation of diffraction grating spectrographs in detail. Using  $35\ \mu\text{m}$  slits, the bandpass<sup>1</sup> of the spectrometer is  $\sim 0.5\ \text{nm}$ .

A key factor limiting the sensitivity of the system are the various apertures which cut down the amount of light reaching the spectrometer. A simple way to characterize the amount of light captured is the semi-angle (half of the full-angle) of the collected light cone. Currently, the aperture of the mount for L2 limits the light collection to  $\sim 5.7^\circ$  semi-angle. The next limiting apertures are the 1 mm hole in the backing material which limits light collection to  $\sim 7.1^\circ$  and the mount for W2 which limits light collection to  $\sim 8.8^\circ$ . By drilling out the backing material and increasing the aperture of the L2 mount an increase in sensitivity of  $\sim [\sin(8.8^\circ)/\sin(5.7^\circ)]^2 \approx 2.4\times$  could be achieved. Greater efficiency in capturing light would require placing a lens inside of the cryostat [91]. Placing an achromatic lens inside of the cryostat configured for infinite conjugate has the advantage of eliminating the effect of optical aberrations introduced by the cryostat windows (see Appendix D). Using backing materials with a  $30^\circ$  semi-angle and placing a lens inside of the cryostat would lead to an increase in sensitivity of  $\sim 25\times$  over the present setup.

---

<sup>1</sup>Bandpass corresponds to the measured full-width-half-maximum of a spectral line with sub-resolution width.

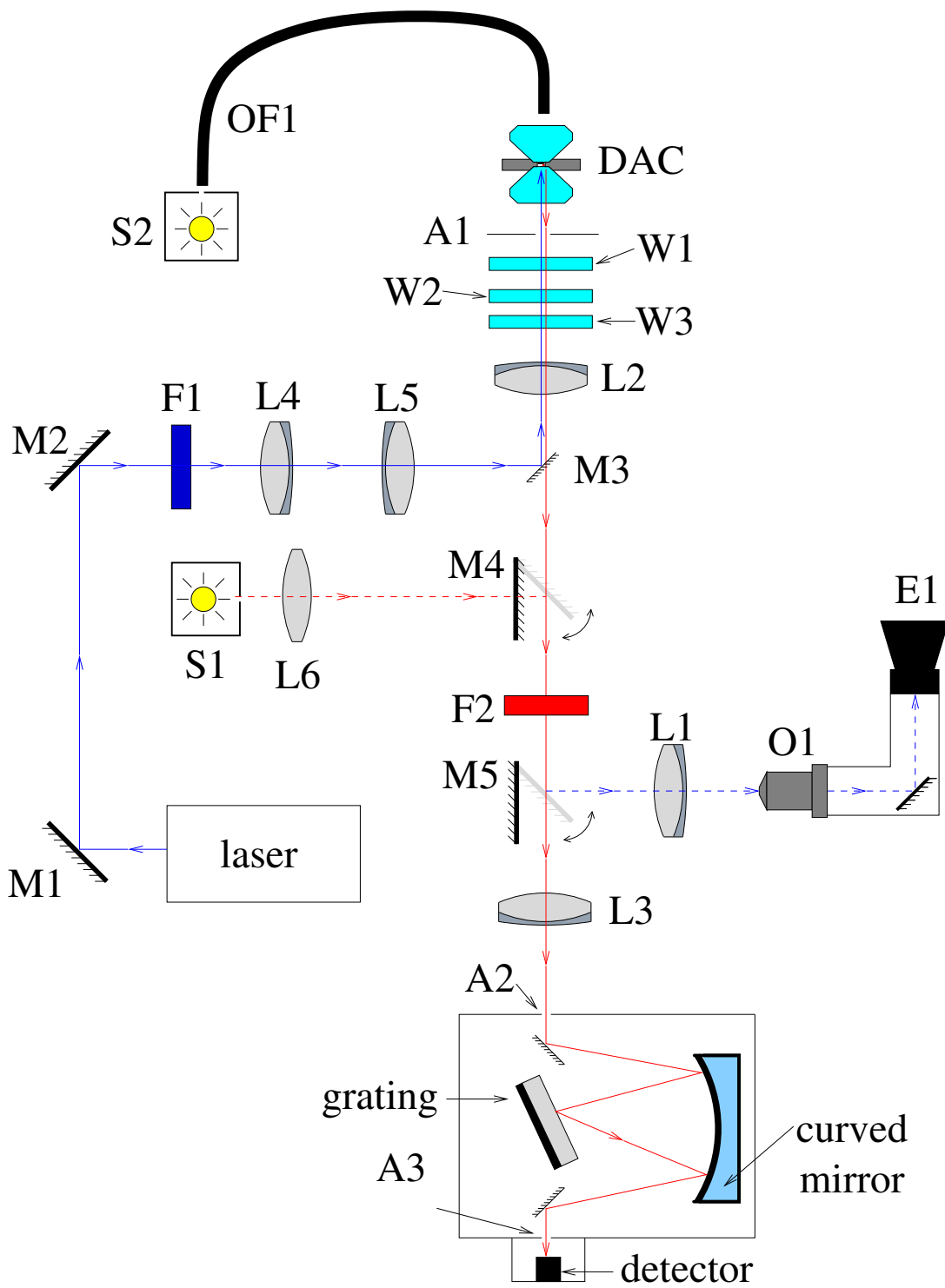


Figure B.1: Schematic of the optical system.

<b>Label</b>	<b>Type</b>	<b>Description</b>
L1	achromatic lens	$f_{L1} = 200$ mm
L2	achromatic lens	$f_{L2} = 80$ mm
L3	achromatic lens	$f_{L3} = 50$ mm
L4	achromatic lens	$f_{L4} = 50$ mm
L5	achromatic lens	$f_{L5} = 50$ mm
L6	singlet lens	$f_{L6} \sim 25$ mm
O1	objective	working distance: $\sim 4$ mm, $M_{O1} = 10$
E1	eyepiece	$M_{E1} = 8$
S1	light source	neon bulb
S2	light source	halogen bulb
F1	filter	short pass (blocks $\gtrsim 550$ nm)
F2	filter	long pass (blocks $\lesssim 600$ nm)
M1, M2	mirrors	beam steering mirrors
M3	mirror	6 mm diameter
M4, M5	mirrors	can be toggled out of light path
OF1	optical fiber	plastic
W1	cryostat window	sapphire (1.2 cm diameter aperture)
W2	cryostat window	quartz (1.5 cm diameter aperture)
W3	cryostat window	quartz (2.5 cm diameter aperture)
A1	aperture	hole in backing material
A2	slit aperture	35, 150, or 1000 $\mu\text{m}$ width
A3	slit aperture	35, 150, or 1000 $\mu\text{m}$ width

Table B.1: Components of the optical system.

## Appendix C

# Optical Measurement using the Nikon Optiphot Microscope

This section briefly describes techniques for measuring fluorescence, Raman scattering and visible absorption spectra in a DAC using the Nikon Optiphot microscope. The set-up for performing such measurements is shown in Figure C.1. For performing the gasket thickness measurements described in Section 3.5.4 an aperture  $\sim 1$  mm diameter must be placed between the DAC and objective to insure that only nearly parallel rays are sampled. Note that the eyepieces for visually inspecting the sample are not shown in this figure. Mirrors  $M1$  and  $M2$  steer the laser beam into the microscope. In order for the objective to focus the beam to the smallest possible point, the laser beam should be focused at the back focal plane of the objective and also should nearly fill the back aperture of the objective. Lens  $L1$  has focal length  $f \sim 5$  cm and is placed  $\sim 21$  cm from objective  $O1$ . Objective  $O1$  has a back focal length (“tube length”) of 16 cm. Thus, the laser is focused to a spot at the back focal plane of the objective and is expanded by a factor of  $\sim 16/5 = 3.2$ . When properly aligned this allows the beam to be focused to a spot  $\sim 10\mu\text{m}$  in diameter. The small diameter of the laser illumination makes it possible to measure pressure gradients within the cell by measuring different pieces of ruby throughout the cell. Mirror  $M3$  is a non-adjustable beam splitter that transmits  $\sim 90\%$  of incident light. Filter  $F1$  blocks scattered laser light from entering optical fiber  $OF2$ . For reflectivity/Raman/fluorescence measurements,  $OF1$  is coupled into the spectrometer. For

absorption measurements,  $OF1$  is coupled into the spectrometer and  $OF1$  is used to illuminate the sample with white light from a halogen light source (this also allows visual observation of the sample color). Coupling the fibers into the spectrometer is accomplished simply by placing the fiber against the spectrometer slit.

Fiber  $OF2$  should be placed at the conjugate focus of  $O1$ , 210 mm from  $O1$ . Optical fiber  $OF2$  collects light from a finite area near the focus of  $O1$ . The smaller the aperture of  $OF2$ , the smaller the sampled area. For a 1 mm diameter fiber and a  $40\times$  objective one can estimate the sampled area is roughly  $1\text{ mm}/40 = 25\ \mu\text{m}$  diameter. By placing an aperture at the conjugate focus of  $O1$  the sampled area can be further reduced. This is confocal microscopy.

Two simple improvements could greatly improve the utility of this system. First, mirrors  $M1$  and  $M2$  should be removed and the laser should be coupled into the microscope using an optical fiber. This would greatly improve the stability of the alignment as well as the ease of achieving alignment. Second, mirror  $M3$  should be replaced with an appropriate dichroic beam splitter. This would improve the sensitivity of the system since presently, we are losing  $\sim 90\%$  of the laser intensity at  $M3$ .

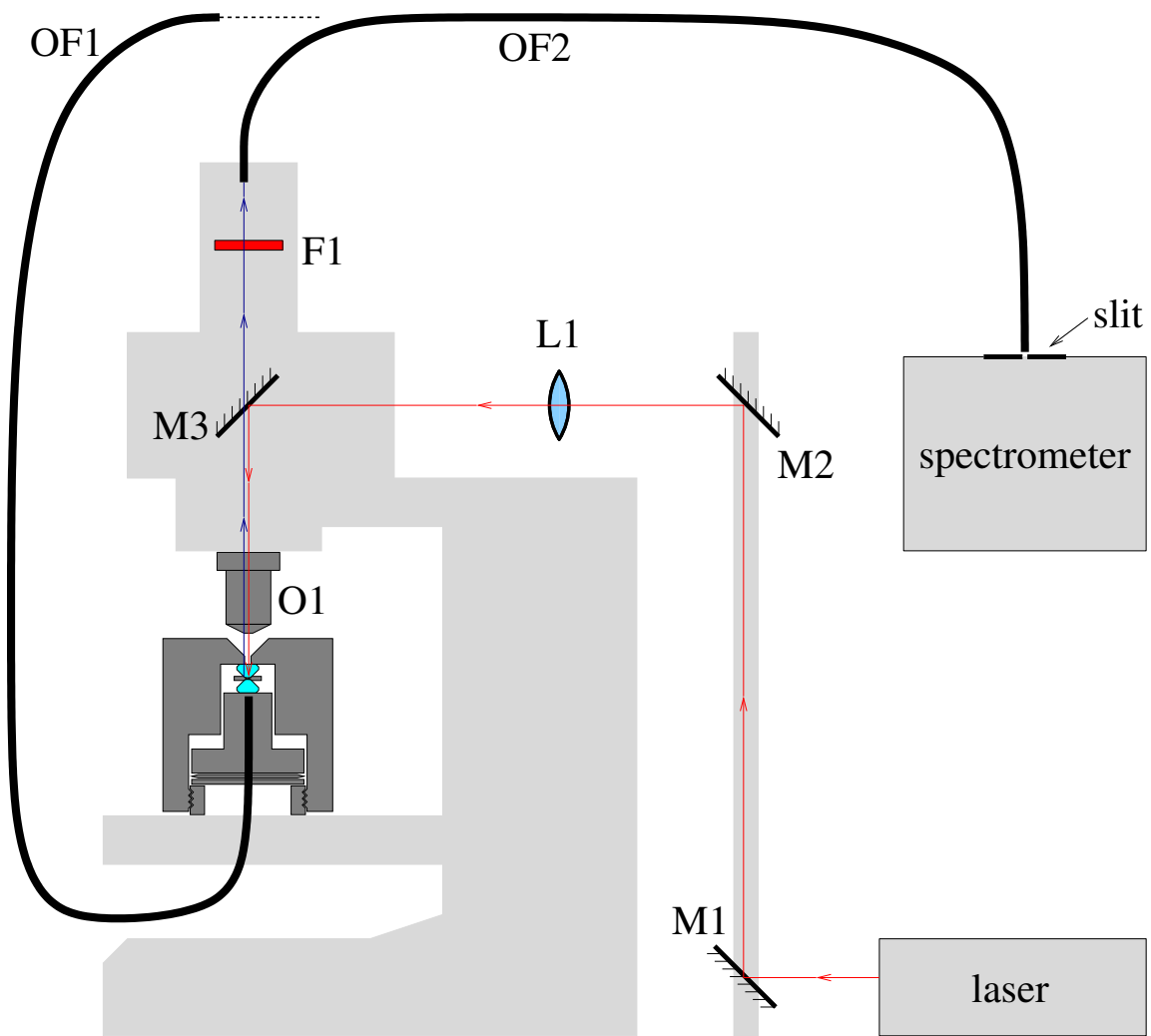


Figure C.1: Schematic of Nikon Optiphot microscope configured for optical measurements in a DAC.

## Appendix D

# A Precise Method for Aligning Optics at Infinite Conjugate

An achromat is a lens that is designed to minimize chromatic and spherical aberrations (for a discussion of aberrations in optical systems see Reference [172]). Most achromats are doublets, a compound lens formed by cementing two different types of glass together. In general the front and back focal lengths are somewhat different. Standard achromats are designed to be used in an infinite conjugate configuration, so that one of the image planes is at infinity. The side of the lens with greater curvature should face the infinite conjugate. Figure D.1 shows an achromat in the proper configuration. If the lens is used in any other configuration, aberrations will be greater. A parallel plate optical element (such as a filter) will aberrate any rays that pass through it, except for rays that pass through perpendicularly. Thus by using lenses in infinite conjugate configuration, it is possible to introduce parallel plate optical elements without introducing any additional aberrations. The following describes a highly precise method for locating the focal point of a lens and aligning lenses for infinite conjugate.

Suppose one wanted to determine very accurately  $f_1$  as shown in Figure D.1. One might want to do this in order to configure the optical system in Figure D.2 for infinite conjugates (so that the rays between the L1 and L2 are parallel). Note that this configuration appears several times throughout the optical system shown in Figure B.1. This basic system can be used as a microscope or for coupling light into

a monochromator.

The alignment described here is similar to what is frequently called the “no parallax” method for locating the focal point of the lens. An object is placed on one side of the lens and an mirror is placed on the other. There is one and only one position of the object where an image is formed at the same location as the object; that position is the focal point of the lens.

Figure D.3 shows the configuration for aligning this system for infinite conjugate. First, the microscope consisting of objective  $O1$  and eyepiece  $E1$  is focused on a crosshair made from 15 micron wire. Then, lens  $L1$  is moved back and forth until an image of the crosshair appears. This image only forms when the object (crosshair) is at the focal point of lens  $L1$ . Thus, when the crosshair and its image are both visible (see Figure D.4), we know that the crosshair is at the focal point of both  $L1$  and  $O1$ . Note that the crosshairs should be illuminated from both sides and that it may be necessary to adjust the angle of mirror  $M1$  so that the image of the crosshairs is visible. Once this alignment has been performed  $M1$  is removed and the distance between the object and  $L2$  is adjusted until the object becomes visible in the eyepiece. At this point, we know that the object is at the focal point of  $L2$ , so that  $L2$  is now also configured for infinite conjugate. Note that when the system is properly aligned for infinite conjugate the imaging properties are not effected by a change in the distance between  $L1$  and  $L2$ .

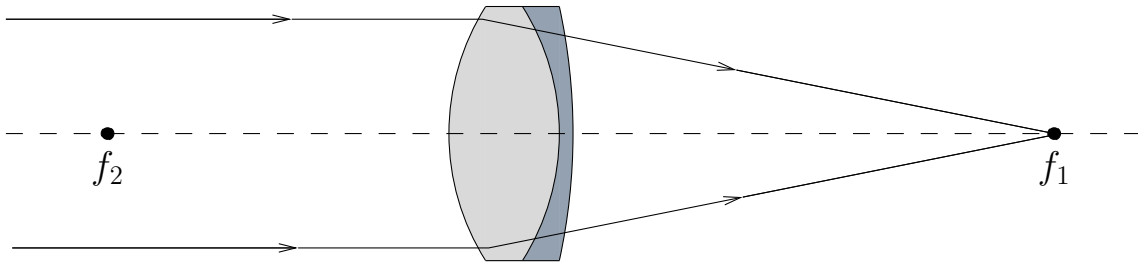


Figure D.1: Proper configuration for achromatic lenses. Achromatic lenses should be oriented so that the surface with greater curvature faces the infinite conjugate.

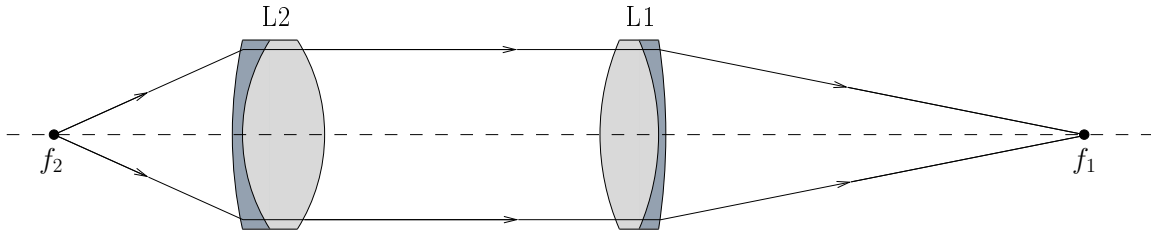


Figure D.2: A common optical system consisting of two achromatic lenses. The system is configured for infinite conjugate so that the rays between  $L1$  and  $L2$  are parallel. The magnification at  $f_1$  is  $M = f_1/f_2$ .

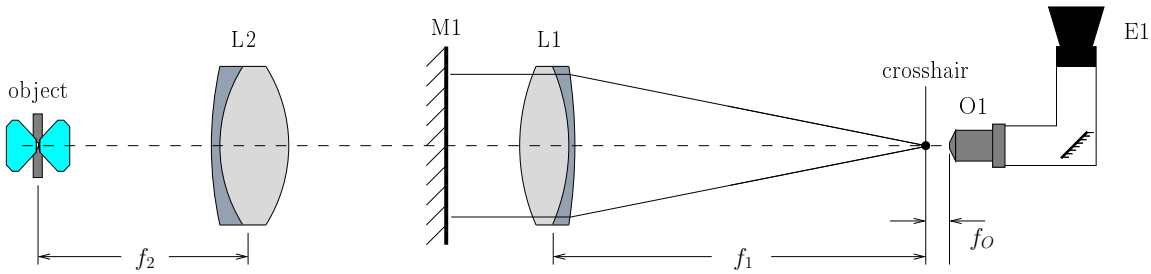


Figure D.3: Method for aligning lenses at infinite conjugate. The lengths  $f_2$ ,  $f_1$  and  $f_0$  are the focal length of  $L2$ ,  $L1$  and objective  $O1$  respectively. When the system is configured for infinite conjugate,  $f_1$  and  $f_0$  are coincident.

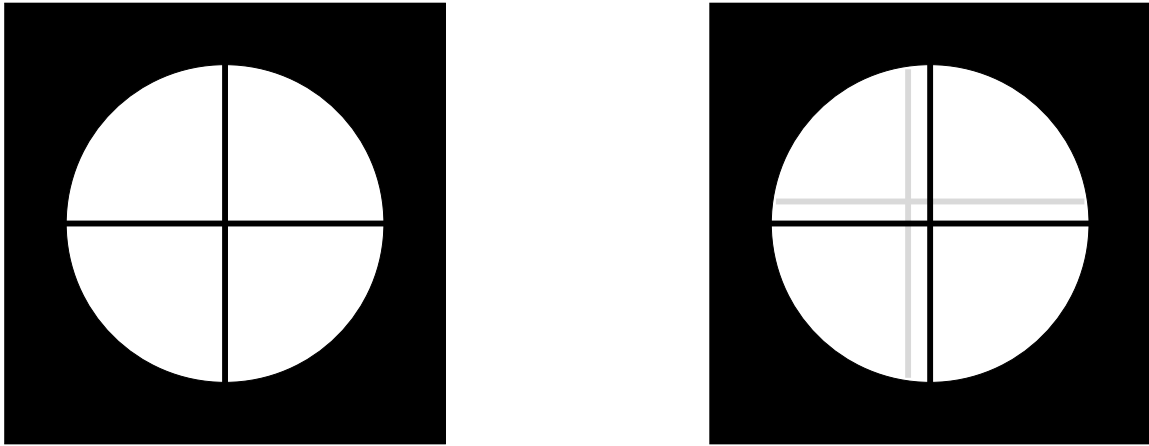


Figure D.4: Appearance of crosshair when system not aligned (left) and when system is aligned for infinite conjugate (right). The light circle on dark background indicates the field of view of the eyepiece. When  $f_1$  and  $f_0$  are coincident two images of the crosshair are visible as shown on the right of the figure. The black lines indicate the crosshair as directly imaged by the objective and the grey lines indicate the dimmer image of the crosshair as imaged by the objective after being reflected by  $M1$ . Adjusting the angle of  $M1$  moves the grey crosshair laterally.

# Bibliography

- [1] Onnes. Sur les résistances électriques. *Solvay*, pages 304–310, 1911.
- [2] Onnes. Further experiments with liquid helium. G. on the electrical resistance of pure metals, etc. VI. On the sudden change in the rate at which the resistance of mercury disappears. *RN*, 14:818–821, 1912.
- [3] J. Bardeen, L. N. Cooper, and J. R. Schrieffer. Theory of superconductivity. *Phys. Rev.*, 108:1175, 1957.
- [4] P. F. Dahl. *Superconductivity: Its Historical Roots and Development from Mercury to the Ceramic Oxides*. American Institute of Physics, New York, 1992.
- [5] T. Schachtman. *Absolute Zero and the Conquest of Cold*. Houghton Mifflin, Boston, 1999.
- [6] J. G. Bednorz and K. A. Müller. Possible high  $T_c$  superconductivity in the Ba-La-Cu-O system. *Z. Physik B*, 64:189–193, 1986.
- [7] C. W. Chu, P. H. Hor, R. L. Meng, L. Gao, Z. J. Huang, and Y. Q. Wang. Evidence for superconductivity above 40 K in the La-Ba-Cu-O compound system. *Phys. Rev. Lett.*, 58:405–410, 1987.
- [8] M. K. Wu, J. R. Ashburn, C. J. Torng, P. H. Hor, R. L. Meng, L. Gao, Z. J. Huang, Y. Q. Wang, and C. W. Chu. Superconductivity at 93 K in a new mixed-phase Yb-Ba-Cu-O compound system at ambient pressure. *Phys. Rev. Lett.*, 58(9):908–910, 1987.
- [9] L. Gao, Y. Y. Xue, F. Chen, Q. Xiong, R. L. Meng, D. Ramirez, C. W. Chu, J. H. Eggert, and H. K. Mao. Superconductivity up to 164 K in

- HgBa<sub>2</sub>Ca<sub>m-1</sub>Cu<sub>m</sub>O<sub>2m+2+δ</sub> (m=1, 2, and 3) under quasihydrostatic pressures. *Phys. Rev. B*, 50(6):4260–4263, 1994.
- [10] P. P. Edwards and C. N. R. Rao. A new era for chemical superconductors. *Chemistry in Britain*, 30(9):722–724, 1994.
- [11] V. Z. Kresin and S. A. Wolf. *Fundamentals of Superconductivity*. Plenum, New York, 1990.
- [12] T. Van Duzer and C. W. Turner. *Principles of Superconductive Devices and Circuits*. Elsevier North Holland, Inc., London, 1981.
- [13] D. R. Tilley and J. Tilley. *Superfluidity and Superconductivity*. Graduate Student Series in Physics. IOP Publishing Ltd, Bristol, England, 3 edition, 1990.
- [14] N. W. Ashcroft and N. D. Mermin. *Solid State Physics*. Brooks/Cole, Thompson Learning, United States, college edition edition, 1976.
- [15] J. File and R. G. Mills. Observation of persistent current in a superconducting solenoid. *Phys. Rev. Lett.*, 10(3):93–97, 1963.
- [16] W. Meissner and R. Ochsenfeld. Ein neuer effect bei eintritt der supraleitfähigkeit. *Die Naturewissenschaften*, 21:787–788, 1933.
- [17] F. London. On the Bose-Einstein condensation. *Phys. Rev.*, 54:947, 1938.
- [18] Jr. R. A. Ogg. Bose-Einstein condensation of trapped electron pairs. phase seperation and superconductivity of metal-ammonia solutions. *Phys. Rev.*, 69:243, 1946.
- [19] Jr. R. A. Ogg. Superconductivity in solid metal-ammonia solutions. *Phys. Rev.*, 70:90, 1946.
- [20] P. P. Edwards. Polarons, bipolarons, and possible high- $T_c$  superconductivity in metal-ammonia solutions. *Journal of Superconductivity: Incorporating Novel Magnetism*, 13(6):933, 2000.
- [21] C. A. Reynolds, B. Serin, W. H. Wright, and L. B. Nesbitt. Superconductivity of isotopes of mercury. *Phys. Rev.*, 78:487, 1950.

- [22] E. Maxwell. Isotope effect in the superconductivity of mercury. *Phys. Rev.*, 78:477, 1950.
- [23] J. Diederichs. *Magnetic and Superconducting Properties of Doped Fullerenes under Hydrostatic Pressure*. PhD thesis, Washington University, St. Louis, Missouri, 1996.
- [24] F. London and H. London. Supraleitung und diamagnetismus. *Physica*, 2:341, 1935.
- [25] C. P. Poole Jr., editor. *Handbook of Superconductivity*. Academic Press, London, 2000.
- [26] P. W. Bridgman. Theoretically interesting aspects of high pressure phenomena. *Rev. Mod. Phys.*, 7(1):1–33, 1935.
- [27] J. Canton. Experiments to prove that water is not incompressible. *Trans. Roy. Soc.*, pages 640–643, 1762.
- [28] P. W. Bridgman. *The Physics of High Pressure*. G. Bell and Sons, LTD, London, 2 edition, 1949.
- [29] C. E. Weir, E. R. Lippincott, A. Van Valkenburg, and E. N. Bunting. Infrared studies in the 1- to 15-micron region to 30,000 atmospheres. *J. Res. Natl. Bur. Stand.*, 63A:55–62, 1959.
- [30] R. A. Forman, G. J. Piermarini, J. D. Barnett, and S. Block. Pressure measurement made by the utilization of ruby sharp-line luminescence. *Science*, 176:284–285, 1972.
- [31] CAS databases, CAplus.
- [32] F. D. Murnaghan. The compressibility of media under extreme pressures. In *Proceedings of the National Academy of Sciences*, volume 30, pages 244–247, 1944.
- [33] F. Birch. Finite elastic strain of cubic crystals. *Phys. Rev.*, 71:809–824, 1947.

- [34] P. Vinet, J. H. Rose, J. Ferrante, and J. R. Smith. Universal features of the equation of state of solids. *J. Phys.: Condens. Matter*, 1:1941–1963, 1989.
- [35] F. Occelli, P. Loubeyre, and R. LeToullec. Properties of diamond under hydrostatic pressure up to 140 GPa. *Nature Materials*, 2:151–154, 2003.
- [36] A. Dewaele, P. Loubeyre, and M. Mezouar. Equations of state of six metals above 94 GPa. *Phys. Rev. B*, 70:094112, 2004.
- [37] M. Hanfland, I. Loa, K. Syassen, U. Schwarz, and K. Takemura. Equation of state of lithium to 21 GPa. *Solid State Commun.*, 112:123–127, 1999.
- [38] M. Hanfland, K. Syassen, N. E. Christensen, and D. L. Novikov. New high-pressure phases of lithium. *Nature*, 408:174, 2000.
- [39] M. Hanfland, I. Loa, and K. Syassen. Sodium under pressure: bcc to fcc structural transition and pressure-volume relation to 100 GPa. *Phys. Rev. B*, 65(18):184109, 2002.
- [40] M. Winzenick, V. Vijayakumar, and W. B. Holzapfel. High-pressure x-ray diffraction on potassium and rubidium up to 50 GPa. *Phys. Rev. B*, 50(17):12381, 1994.
- [41] K. Takemura, N. E. Christensen, D. L. Novikov, K. Syassen, U. Schwarz, and M. Hanfland. Phase stability of highly compressed cesium. *Phys. Rev. B*, 61(21):14399, 2000.
- [42] J. van Straaten, R. J. Wijngaarden, and I. F. Silvera. Low-temperature equation of state of molecular hydrogen and deuterium to 0.37 Mbar: implications for metallic hydrogen. *Phys. Rev. Lett.*, 48(2):97–100, 1982.
- [43] P. Loubeyre, R. LeToullec, D. Hausermann, M. Hanfland, R. J. Hemley, H. K. Mao, and L. W. Finger. X-ray diffraction and equation of state of hydrogen at megabar pressures. *Nature*, 383:702–704, 1996.
- [44] H. Cynn, J. E. Klepeis, C.-S. Yoo, and D. A. Young. Osmium has the lowest experimentally determined compressibility. *Phys. Rev. Lett.*, 88(13):135701, 2002.

- [45] H. G. Drickamer. Optical studies at high pressure. In F. P. Bundy, W. R. Hibbard Jr., and H. M. Strong, editors, *Progress in Very High Pressure Research*, New York, 1960. John Wiley & Sons, Inc.
- [46] W. L. McMillan. Transition temperature of strong-coupled superconductors. *Phys. Rev.*, 167(2):331–344, 1968.
- [47] J. J. Hopfield. Systematics of high  $T_c$  in transition metal materials. *Physica*, 55:41–49, 1971.
- [48] J. S. Schilling. *Handbook of High Temperature Superconductivity: Theory and Experiment*, chapter 11. Springer, Hamburg, 2007.
- [49] J. J. Hamlin, V. G. Tissen, and J. S. Schilling. Superconductivity at 20 K in yttrium metal at pressures exceeding 1 Mbar. *Physica C*, 451:82, 2007.
- [50] T. Yabuuchi, T. Matsuoka, Y. Nakamoto, and K. Shimizu. Superconductivity of Ca exceeding 25 K at megabar pressures. *J. Phys. Soc. Japan*, 75(8):083703, 2006.
- [51] C. Buzea and K. Robbie. Assembling the puzzle of superconducting elements: a review. *Supercond. Sci. Technol.*, 18:R1–R8, 2005.
- [52] V. L. Ginzburg and D. A. Kirzhnits. *High-Temperature Superconductivity*. Consultants Bureau, New York, 1982.
- [53] Z. P. Yin, S. Y. Savrasov, and W. E. Pickett. Linear response study of strong electron-phonon coupling in yttrium under pressure. *Phys. Rev. B*, 74:094519, 2006.
- [54] E. Wigner and H. B. Huntington. On the possibility of a metallic modification of hydrogen. *J. Chem. Phys.*, 3(12):764–770, 1935.
- [55] N. W. Ashcroft. Metallic hydrogen: A high-temperature superconductor? *Phys. Rev. Lett.*, 21(26):1748–1749, 1968.
- [56] W. A. Harrison. *Elementary Electronic Structure*. World Scientific, New Jersey, 1999.

- [57] J. T. Waber and D. T. Cromer. Orbital radii of atoms and ions. *J. Chem. Phys.*, 42:4116–4123, 1965.
- [58] E. Clementi and C. Roetti. Roothaan-Hartree-Fock atomic wavefunctions basis functions and their coefficients for ground and certain excited states of neutral and ionized atoms,  $Z \leq 54$ . *Atomic data and Nuclear data Tables*, 14:177–478, 1974.
- [59] N. W. Ashcroft. Bridgman’s high pressure atomic destructibility and it’s growing legacy of disordered states. *J. Phys.: Condens. Matter*, 16:S945–S952, 2004.
- [60] J. S. Schilling. Magnetism at high pressure. *Mat. Res. Soc. Symp. Proc.*, 22:79–88, 1984.
- [61] K. Shimizu, T. Kimura, S. Furomoto, K. Takeda, K. Kontani, Y. Onuki, and K. Amaya. Superconductivity in the non-magnetic state of iron under pressure. *Nature*, 412:316–318, 2001.
- [62] P. P. Edwards, R. L. Johnston, C. N. R. Rao, D. P. Tunstall, and F. Hensel. The metal-insulator transition: a perspective. *Phil. Trans. R. Soc. Lond. A*, 356:5–22, 1998.
- [63] D. A. Goldhammer. *Dispersion und Absorption des Lichtes*. Tubner-Verlag, Leipzig, 1911.
- [64] K. F. Herzfeld. On atomic properties which make an alement a metal. *Phys. Rev.*, 29:701–705, 1927.
- [65] L. Pauling. *General Chemistry*. W. H. Freeman, San Fransisco, 3 edition, 1970.
- [66] D. R. Lide, editor. *Handbook of Chemistry and Physics*. CRC Press, New York, 85 edition, 2004.
- [67] J. P. Van Dyke and G. A. Samara. Thallous halides: Pressure dependence of the energy-band structure and the insulator-metal transition. *Phys. Rev. B*, 11(12):4935–4944, 1975.

- [68] P. P. Edwards and M. J. Sienko. The transition to the metallic state. *Acc. Chem. Res.*, 15:87–93, 1982.
- [69] A. P. Jephcoat, H. K. Mao, L. W. Finger, D. E. Cox, R. J. Hemley, and C. S. Zha. Pressure-induced structural phase transitions in solid xenon. *Phys. Rev. Lett.*, 59(23):2670–2673, 1987.
- [70] J. H. Eggert, K. A. Goettel, and I. F. Silvera. Ruby at high pressure. II. fluorescence lifetime of the R line to 130 GPa. *Phys. Rev. B*, 40(8):5733–5738, 1989.
- [71] R. Reichlin, K. E. Brister, A. K. McMahan, M. Ross, S. Martin, Y. K. Vohra, and A. L. Ruoff. Evidence for the insulator-metal transition in xenon from optical, x-ray, and band-structure studies to 170 GPa. *Phys. Rev. Lett.*, 62(6):669–672, 1989.
- [72] M. I. Eremets, E. A. Gregoryanz, V. V. Struzhkin, H. K. Mao, R. J. Hemley, N. Mulders, and Neil M. Zimmerman. Electrical conductivity of xenon at megabar pressures. *Phys. Rev. Lett.*, 85(13):2797–2800, 2000.
- [73] M. Ross. On the Herzfeld theory of metallization. application to rare gases, alkali halides, and diatomic molecules. *J. Chem. Phys.*, 56(9):4651–4653, 1972.
- [74] H. L. Skriver. Crystal structure from one-electron theory. *Phys. Rev. B*, 31(4):1909–1923, 1985.
- [75] G. J. Piermarini and C. E. Weir. Allotropy in some rare-earth metals at high pressures. *Science*, 144:69–72, 1965.
- [76] A. Rosengren and B. Johansson. Alloy theory of the intermediate valence state: Application to europium metal. *Phys. Rev. B*, 13(4):1468–1472, 1976.
- [77] K. Takemura and K. Syassen. Pressure-volume relations and polymorphism of europium and ytterbium to 30 GPa. *J. Phys. F: Met. Phys.*, 15:543–559, 1985.
- [78] G. N. Chesnut and Y. K. Vohra. Structural and electronic transitions in ytterbium metal to 202 GPa. *Phys. Rev. Lett.*, 82(8):1712–1715, 1999.

- [79] Y. K. Vohra, S. L. Beaver, J. Akella, C. A. Ruddle, and S. T. Weir. Ultrapressure equation of state of cerium metal to 208 GPa. *J. Appl. Phys.*, 85(4):2451–2153, 1999.
- [80] W. Martienssen, editor. *Springer Handbook of Condensed Matter and Materials Data*. Springer Verlag, Berlin, 2005.
- [81] B. Johansson and A. Rosengren. Generalized phase diagram for the rare-earth elements: Calculations and correlations of bulk properties. *Phys. Rev. B*, 11(8):2836–2857, 1975.
- [82] T. Krüger, B. Merkau, W. A. Grosshans, and W. B. Holzapfel. Kinetics and systematics of structural phase transitions in the regular lanthanide metals under pressure. *High Pres. Res.*, 2:193–236, 1990.
- [83] J. C. Duthie and D. G. Pettifor. Correlation between d-band occupancy and crystal structure in the rare earths. *Phys. Rev. Lett.*, 38(10):564–567, 1977.
- [84] W. B. Daniels and M. G. Ryschkewitsch. Simple double diaphragm press for diamond anvil cells at low temperatures. *Rev. Sci. Instrum.*, 54(1):115–116, Jan. 1983.
- [85] J. S. Dugdale. *Physics of High Pressures and the Condensed Phase*, chapter 9, page 386. North-Holland, Amsterdam, 1965.
- [86] D. M. Adams, A. G. Christy, and A. J. Norman. Optimization of diamond anvil cell performance by finite element analysis. *Meas. Sci. Technol.*, 4:422–430, 1993.
- [87] T. Matsuoka. private communication, 2007.
- [88] V. G. Tissen. private communication, 2006.
- [89] M. Eremets. *High Pressure Experimental Methods*. Oxford University Press, New York, 1996.
- [90] M. Baucchio, editor. *ASM metals reference book*. ASM International, Ohio, 3 edition, 1993.

- [91] J. H. Eggert, F. Moshary, W. J. Evans, K. A. Goettel, and I. F. Silvera. Ruby at high pressure. III. a pumping scheme for the R lines up to 230 GPa. *Phys. Rev. B*, 44(14):7202–7208, October 1991.
- [92] S. Buchsbaum, R. L. Mills, and D. Schiferl. Phase diagram of N<sub>2</sub> determined by raman spectroscopy from 15 to 300 K at pressures to 52 GPa. *J. Phys. Chem.*, 88:2522–2525, 1984.
- [93] D. M. Adams, R. Appleby, and S. K. Sharma. Spectroscopy at very high pressures: Part X. use of the ruby R-lines in the estimation of pressure at ambient and low temperatures. *J. Phys. E: Sci. Instr.*, 9:1140–1144, 1976.
- [94] J. Yen and M. Nicol. Temperature dependence of the ruby luminescence method for measuring high pressures. *J. Appl. Phys.*, 72(12):5535–5538, 1992.
- [95] G. J. Piermarini, S. Block, J. D. Barnett, and R. A. Forman. Calibration of the pressure dependence of the R<sub>1</sub> ruby fluorescence line to 195 kbar. *J. Appl. Phys.*, 46(6):2774–2780, 1975.
- [96] H. K. Mao, P. M. Bell, J. W. Shaner, and D. J. Steinberg. Specific volume measurements of Cu, Mo, Pd, and Ag and calibration of the ruby R<sub>1</sub> fluorescence pressure gauge from 0.06 to 1 Mbar. *J. Appl. Phys.*, 49(6):3276–3283, 1978.
- [97] H. K. Mao, J. Xu, and P. M. Bell. Calibration of the ruby pressure gauge to 800 kbar under quasi-hydrostatic conditions. *J. Geophys. Res.*, 91(B5):4673–4676, 1986.
- [98] R. J. Hemley, C. S. Zha, A. P. Jephcoat, H. K. Mao, L. W. Finger, and D. E. Cox. X-ray diffraction and equation of state of solid neon to 110 GPa. *Phys. Rev. B*, 39(16):11820–11827, 1989.
- [99] W. B. Holzapfel. Progress in the realization of a practical pressure scale for the range 1-300 GPa. *High Pres. Res.*, 25(2):87–96, 2005.
- [100] A. D. Chijioke, W. J. Nellis, A. Soldatov, and I. F. Silvera. The ruby pressure standard to 150 GPa. *J. Appl. Phys.*, 98(11):114905–1, 2005.

- [101] I. F. Silvera, A. D. Chijioke, W. J. Nellis, A. Soldatov, and J. Tempere. Calibration of the ruby pressure scale to 150 GPa. *Phys. Stat. Sol. (b)*, 244(1):460–467, 2007.
- [102] K. Asaumi and A. L. Ruoff. Nature of the state of stress produced by xenon and some alkali iodides when used as pressure media. *Phys. Rev. B*, 33(8):5633–5636, 1986.
- [103] M. Chai and J. M. Brown. Effects of static non-hydrostatic stress on the R lines of ruby single crystals. *Geophys. Res. Lett.*, 23(24):3539–3542, 1996.
- [104] J. H. Eggert, K. A. Goettel, and I. F. Silvera. Elimination of pressure-induced fluorescence in diamond anvils. *Appl. Phys. Lett.*, 53(25):2489–2491, 1988.
- [105] A. L. Ruoff. *Recent Trends in High Pressure Research*. IBH, Oxford, New Delhi, 1992.
- [106] N. H. Chen and I. F. Silvera. Excitation of ruby fluorescence at multimegabar pressures. *Rev. Sci. Instrum.*, 67(12):4275–4278, 1996.
- [107] D. Krishnamurti. The Raman spectrum of diamond. *Proc. Indian Acad. Sci. Sect. A*, 40:211, 1954.
- [108] S. A. Solin and A. K. Ramdas. Raman spectrum of diamond. *Phys. Rev. B*, 1(4):1687–1698, 1970.
- [109] H. Boppart, J. van Straaten, and I. F. Silvera. Raman spectra of diamond at high pressures. *Phys. Rev. B*, 32(2):1423–1425, 1985.
- [110] M. Hanfland and K. Syassen. A Raman study of diamond anvils under stress. *J. Appl. Phys.*, 57(8):2752–2756, 1985.
- [111] Y. Akahama and H. Kawamura. Pressure calibration of diamond anvil raman gauge to 310 GPa. *J. Appl. Phys.*, 100:043516, 2006.
- [112] B. C. Smith. *Fundamentals of Fourier transform infrared spectroscopy*. CRC Press, Boca Raton, 1996.

- [113] A. Dewaele, J. H. Eggert, P. Loubeyre, and R. Le Toullec. Measurement of refractive index and equation of state in dense He, H<sub>2</sub>, H<sub>2</sub>, and Ne under high pressure in a diamond anvil cell. *Phys. Rev. B*, 67:094112, 2003.
- [114] D. D. Jackson, C. Aracne-Ruddle, V. Malba, S. T. Weir, S. A. Catledge, and Y. K. Vohra. Magnetic susceptibility measurements at high pressure using designer diamond anvils. *Rev. Sci. Instrum.*, 74(4):2467–2471, 2003.
- [115] R. I. Joseph. Ballistic demagnetizing factor in uniformly magnetized cylinders. *J. Appl. Phys.*, 37(13):4639–4643, 1966.
- [116] A. Aharoni. Demagnetizing factors for rectangular ferromagnetic prisms. *J. Appl. Phys.*, 83(6):3432–3434, 1998.
- [117] J. Wittig. Pressure-induced superconductivity in cesium and yttrium. *Phys. Rev. Lett.*, 24(15):812–815, 1970.
- [118] J. Wittig, C. Probst, F. A. Schmidt, and Jr. K. A. Gschneidner. Superconductivity in a new high-pressure phase of scandium. *Phys. Rev. Lett.*, 42(7):469–472, 1979.
- [119] J. Wittig. Superconductivity in elements and binary systems at high pressure. *Mat. Res. Soc. Symp. Proc.*, 22:17, 1984.
- [120] R. N. Shelton and A. R. Moodenbaugh. Search for superconductivity at high pressures in Eu, EuMo<sub>6</sub>S<sub>8</sub> and EuMo<sub>6</sub>Se<sub>8</sub>. *Phys. Rev. B*, 24(5):2863–2866, 1981.
- [121] F. P. Bundy and K. J. Dunn. Electrical behavior of Eu at very high pressure and low temperatures. *Phys. Rev. B*, 24(8):4136–4141, 1981.
- [122] K. Shimizu, H. Ishikawa, D. Takao, T. Yagi, and K. Amaya. Superconductivity in compressed lithium at 20 K. *Nature*, 419:597–600, 2002.
- [123] J.J. Hamlin, V.G. Tissen, and J.S. Schilling. Superconductivity at 17 K in yttrium metal under nearly hydrostatic pressures up to 89 GPa. *Phys. Rev. B*, 73:094522, 2006.

- [124] W. A. Grosshans and W. B. Holzapfel. Atomic volumes of rare-earth metals under pressures to 40 GPa and above. *Phys. Rev. B*, 45:5171, 1992.
- [125] H. Fujihisa, Y. Akahama, H. Kawamura, Y. Gotoh, H. Yamawaki, M. Sakashita, S. Takeya, and K. Honda. Incommensurate composite crystal structure of scandium-II. *Phys. Rev. B*, 72:132103–132106, 2005.
- [126] G. N. Chesnut and Y. K. Vohra. Phase transformation in lutetium metal at 88 GPa. *Phys. Rev. B*, 57(17):10221–10223, 1998.
- [127] P. B. Allen and R. C. Dynes. Transition temperature of strong-coupled superconductors reanalyzed. *Phys. Rev. B*, 12(3):905–922, 1975.
- [128] T. Tomita, J. J. Hamlin, J. S. Schilling, D. G. Hinks, and J. D. Jorgensen. Dependence of  $T_c$  on hydrostatic pressure in superconducting  $\text{MgB}_2$ . *Phys. Rev. B*, 64:092505, 2001.
- [129] X. J. Chen, H. Zhang, and H. U. Habermeier. Effects of pressure on the superconducting properties of magnesium diboride. *Phys. Rev. B*, 65:144514, 2002.
- [130] Jr. K. A. Gschneidner. *Solid State Physics*, volume 16, page 275. Academic Press, New York, 1964.
- [131] W. H. Butler. Electron-phonon coupling in the transition metals: Electronic aspects. *Phys. Rev. B*, 15(11):5267–5282, 1977.
- [132] T. W. E. Tsang, Jr. K. A. Gschneidner, F. A. Schmidt, and D. K. Thome. Low-temperature heat capacity of electrotransport-purified scandium, yttrium, gadolinium and lutetium. *Phys. Rev. B*, 31(1):235–244, 1985.
- [133] G. S. Knapp, R. W. Jones, and B. A. Loomis. *Low Temperature Physics*, volume 3 of *LT-13*, page 611. Plenum, 1974.
- [134] H. B. Radousky, T. Jarlborg, G. S. Knapp, and A. J. Freeman. Assessment of theoretical determinations of the electron-phonon coupling parameter  $\lambda$  in metals and intermetallic compounds. *Phys. Rev. B*, 26:1208, 1982.

- [135] H. L. Skriver and I. Mertig. Electron-phonon coupling in the rare-earth metals. *Phys. Rev. B*, 41:6553, 1990.
- [136] M. M. Sigalas and D. A. Papaconstantopoulos. Calculation of total energy, electron-phonon interaction and Stoner parameter for metals. *Phys. Rev. B*, 50(11):7255–7261, 1994.
- [137] L. W. Nixon, D. A. Papaconstantopoulos, and M. J. Mehl. Calculations of the superconducting properties of scandium under high pressure. *Phys. Rev. B*, 76:134512, 2007.
- [138] C. Probst and J. Wittig. *Handbook on the Physics and Chemistry of Rare Earths*, page 749. North-Holland, Amsterdam, 1978.
- [139] S. Lei, D. A. Papaconstantopoulos, and M. J. Mehl. Calculations of superconducting properties in yttrium and calcium under high pressure. *Phys. Rev. B*, 75(2):024512, 2007.
- [140] V. G. Tissen, E. G. Ponyatovskii, M. V. Nefedova, F. Porsch, and W. B. Holzapfel. Effect of pressure on the superconducting  $T_c$  of lanthanum. *Phys. Rev. B*, 53(13):8238–8240, 1996.
- [141] D. G. Pettifor. Theory of energy bands and related properties of 4d transition metals: I. band parameters and their volume dependence. *J. Phys. F: Met. Phys.*, 7(4):613–633, 1977.
- [142] W. E. Pickett. private communication. private communication.
- [143] O. Degtyareva, M. I. McMahon, and R. J. Nelmes. High-pressure structural studies of group-15 elements. *High Pres. Res.*, 24(3):319–356, 2004.
- [144] J. Nagamatsu, N. Nakagawa, T. Muranaka, Y. Zenitani, and J. Akimitsu. Superconductivity at 39 K in magnesium diboride. *Nature*, 410:63–64, 2001.
- [145] K. Tanigaki, T. W. Ebbesen, S. Saito, J. Mizuki, J. S. Tsai, Y. Kubo, and S. Kuroshima. Superconductivity at 33 K in  $\text{Cs}_x\text{Rb}_y\text{C}_{60}$ . *Nature*, 352:222–223, 1991.

- [146] J. B. Neaton and N. W. Ashcroft. Pairing in dense lithium. *Nature*, 400:141–143, 1999.
- [147] T. H. Lin and K. J. Dunn. High-pressure and low-temperature study of electrical resistance of lithium. *Phys. Rev. B*, 33(2):807–811, 1986.
- [148] V. V. Struzhkin, M. I. Erements, W. Gan, H. K. Mao, and R. J. Hemley. Superconductivity in dense lithium. *Science*, 298:1213–1215.
- [149] S. Deemyad and J. S. Schilling. Superconducting phase diagram of Li metal in nearly hydrostatic pressures up to 67 GPa. *Phys. Rev. Lett.*, 91(16):167001, 2003.
- [150] G. Oomi and S. B. Woods. The electrical resistance of some lithium-magnesium alloys near the martensitic transformation. *Solid State Commun.*, 53:223–225, 1985.
- [151] K. Shimizu. private communication.
- [152] T. B. Massalski, editor. *Binary Alloy Phase Diagrams*, volume 2. William W. Scott. Jr., 1986.
- [153] V. F. Degtyareva. Brillouin zone concept and crystal structures of sp metals under high pressure. *High Pres. Res.*, 23(3):252–257, 2003.
- [154] V. F. Degtyareva. Simple metals at high pressures: the Fermi sphere - Brillouin zone interaction model. *Physics-USpekhi*, 49(4):369–388, 2006.
- [155] N. F. Mott and H. Jones. *The Theory of the Properties of Metals and Alloys*. Oxford University Press, London, 1936.
- [156] H. Jones. *The theory of Brillouin Zones and Electron States in Crystals*. North-Holland, Amsterdam, 1962.
- [157] J. Feng, N. W. Ashcroft, and R. Hoffmann. Theoretical indications of singular structural and electronic features of Laves-phase  $\text{CaLi}_2$  under pressure. *Phys. Rev. Lett.*, 98(24):247002, 2007.

- [158] D. Fischer and M. Jansen. A new modification of the Laves phase  $\text{CaLi}_2$ . *Z. Anorg. Allg. Chem.*, 629:1934, 2003.
- [159] T. Matsuoka, M. Debessai, J. J. Hamlin, A. K. Gangopadhyay, J. S. Schilling, and K. Shimizu. Search for superconductivity under pressure in  $\text{CaLi}_2$ , 2007.
- [160] C. Narayana, H. Luo, J. Orloff, and A. L. Ruoff. Solid hydrogen at 342 GPa: no evidence for an alkali metal. *Nature*, 393:46–49, 1998.
- [161] N. W. Ashcroft. Hydrogen dominant metallic alloys: High temperature superconductors. *Phys. Rev. Lett.*, 92(18):187002, 2004.
- [162] J. Feng, W. Grochala, T. Jaroń, R. Hoffmann, A. Bergara, and N. W. Ashcroft. Structures and potential superconductivity in  $\text{SiH}_4$  at high pressure: En route to “metallic hydrogen”. *Phys. Rev. Lett.*, 96:017006, 2006.
- [163] M. Martinez-Canales and A. Bergara. No evidence of metallic methane at high pressure. *High Pres. Res.*, 26(4):369–375, 2006.
- [164] J. P. Blackledge. *Metal Hydrides*, chapter 1. Academic Press, New York, 1968.
- [165] J-Ph. Soulié, G. Renaudin, R. Černý, and K. Yvon. Lithium boro-hydride  $\text{LiBH}_4$  I. crystal structure. *J. Alloys Compd.*, 346:200–205, 2002.
- [166] P. Vajeeston, P. Ravindran, R. Vidya, H. Fjellvåg, and A. Kjekshus. Huge-pressure-induced volume collapse in  $\text{LiAlH}_4$  and its implications to hydrogen storage. *Phys. Rev. B*, 68:212101, 2003.
- [167] M. J. van Setten, V. A. Popa, G. A. de Wijs, and G. Brocks. Electronic structure and optical properties of lightweight metal hydrides. *Phys. Rev. B*, 75:035204, 2007.
- [168] K. Nakamoto. *Infrared and Raman Spectra of Inorganic and Coordination Compounds Part A: Theory and Applications in Inorganic Chemistry*. John Wiley & Sons, Inc., New York, 5 edition, 1997.

- [169] S. J. Jeon, R. F. Porter, Y. K. Vohra, and A. L. Ruoff. High-pressure x-ray-diffraction and optical-absorption studies of  $\text{NH}_4\text{I}$  to 75 GPa. *Phys. Rev. B*, 35(10):4954, 1987.
- [170] J. C. Phillips. *Solid State Physics*, volume 18, chapter 2, page 55. Academic Press, New York, 1966.
- [171] S. P. Davis. *Diffraction Grating Spectrographs*. Holt, Rinehart and Winston, New York, 1970.
- [172] E. Hecht. *Optics*. Addison-Wesley, 3rd edition, 1998.